Chaotic Modeling and Simulation (CMSIM) 3: 451–459, 2012

Quantum-Classical Correspondence through Entanglement Dynamics

Lock Yue Chew[1] and Ning Ning Chung[2]

[1] Nanyang Technological University, 21 Nanyang Link, SPMS-PAP-04-04, Singapore 637371
(E-mail: lockyue@ntu.edu.sg)
[2] Temasek Laboratory, National University of Singapore, Singapore 117508
(E-mail: tslcnn@nus.edu.sg)

Abstract. In the study of quantum chaos relating to entanglement dynamics, it is found that local dynamical features in the classical phase space, such as the tori in regular island and the chaotic sea, can have subtle influence on the entanglement production rate, the maximum entanglement entropy etc. In this paper, we revisit the two-coupled quartic oscillator system, whose entanglement dynamics was shown by Chung and Chew (2009, *Phys. Rev. E*, **80** 016204) to be insensitive to these local dynamical features. By means of a comprehensive set of initial coherent states, and by considering both the quantum and semi-classical regime, we provide additional numerical evidence and physical insights that support the conclusion that the entanglement dynamics of this system is dependent on the global classical dynamical regime while insensitive to the local classical behavior.
Keywords: Quantum-classical correspondence, Entanglement dynamics, Quantum chaos, Classical chaos, Coupled quartic oscillators, Quantum information processing.

1 Introduction

The problem of quantum-classical correspondence is related to the subject of quantum chaos. The study of how a classically chaotic system has a mysterious influence on its quantized counterpart has made quantum chaos a fasinating subject. The influence of chaos, instead of leading to an exponential divergence of quantum wavefunctions through minute changes of initial conditions (which is not possible since Schrödinger equation is linear), left its imprint through quantum properties such as the energy level statistics, the localization, or the scarring of the wavefunction [1].

Recently, there is great interest in the study of the effect of classical chaos on the entanglement between composite quantum system [2–7]. This results from the fact that entanglement is an important resource for information processing in the quantum regime. In particular, its non-classical feature has enabled the creation of novel information processing paradigms. For example, entanglement has important application in superdense coding, quantum teleportation

Received: 25 July 2011 / Accepted: 31 March 2012

ISSN 2241-0503

and quantum cryptography [8]. The importance of entanglement for quantum information processing suggests the need to generate entangled quantum states. A particular approach to create entangled quantum states is by means of quantum harmonic and anharmonic oscillator systems. Experimentally, quantum harmonic oscillator system has been achieved in the form of a micromechanical resonators strongly coupled to an optical field [9]. An extension to this system has also been proposed with the resonator interact with a trapped atom through a quantized light field in a laser driven high-finesse cavity [10]. On the other hand, quantum anharmonic oscillator system can be implemented by optical fibre with Kerr nonlinearities. By injecting coherent states into such a fibre, two Schrödinger cat-like states can be generated [11].

The consideration of the effects of chaos on entanglement have led to the studies of many diverse systems beyond quantum anharmonic oscillator systems. These systems are coupled kicked tops [2,7], Rydberg molecules [5] and interacting spin systems [6]. Generically, it is found in these investigations that when the classical system is more chaotic, the corresponding quantized system has more entanglement and also a faster entanglement production rate, although there are some notable exceptions [12,13]. In addition, the frequency of oscillation of the entanglement dynamics increases as the classical system becomes more chaotic. An important observation made by many researchers [4,5,2] is that the magnitude and production rate of the entanglement is dependent on the local dynamical structure of the corresponding classical phase space. This places the existence of a universal quantum-classical correspondence in terms of dynamcial entanglement production in a doubtful position. However, we have shown in [3] that contrary to such a local phase space dependence, it is possible for the entanglement dynamics to depend solely on the global classical dynamical regime.

In this paper, we will present our investigation on the correspondence between classical system and its quantized version through the entanglement entropy. More precisely, for the classical systems, we shall study its dynamics in the classical phase space and then relate it to the corresponding entanglement dynamics in the quantized system. We shall study such quantum-classical correspondence in an anharmonic oscillator system that can exhibit regular, mixed and purely chaotic dynamics. By perfoming detailed numerical computations, we have strengthed our earlier conclusion in [3] that it is possible for the entanglement dynamics to depend on the global classical dynamical regime.

2 The Coupled Quartic Oscillator

To begin, let us introduce our coupled nonlinear oscillator system. It is the coupled quartic oscillator given by the following Hamiltonian [14]:

$$H = \frac{1}{2}\left(p_1^2 + p_2^2\right) + 3x_1^4 + x_2^4 - \lambda x_1^2 x_2^2\,, \tag{1}$$

where p_1 and p_2 are the momenta, x_1 and x_2 the positions of the oscillator, and λ is the coupling constant. Depending on the value of λ, the classical dynamics

of this coupled quartic oscillator can display three distinct features: (a) regular dynamics (see Fig. 1), (b) a mixture of regular and chaotic dynamics (see Fig. 2), and (c) purely chaotic dynamics (see Fig. 3). Note that Figs. 1 to 3 gives the Poincaré section of the dynamics in the x_2-p_2 plane with $x_1 = 0$ and $p_1 > 0$.

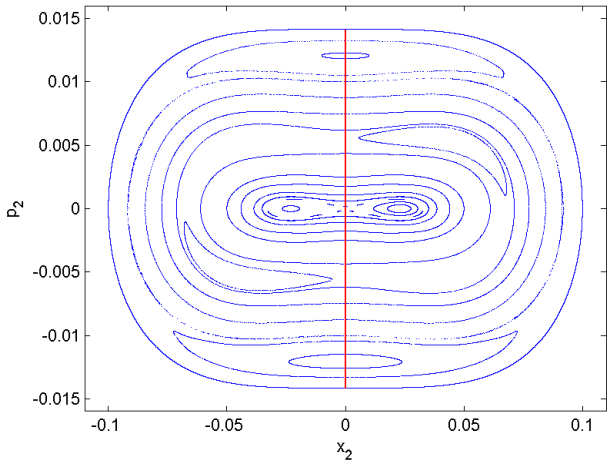

Fig. 1. Classical phase portrait for the coupled quartic oscillator system with coupling constant $\lambda = 0.4$. Note that twenty-nine equally spaced points are selected on the straight line with their corresponding coherent states serve as initial conditions for the entanglement dynamics evaluation.

Next, we proceed to quantize the coupled quartic oscillator system and investigate its quantum dynamics. This requires us to replace x_i and p_i with the corresponding operators $\hat{x}_i$ and $\hat{p}_i$. We select the product states $|n_1\rangle \otimes |n_2\rangle$ as our basis for the numerical computation. $|n_1\rangle$ and $|n_2\rangle$ are the eigenvectors of the harmonic oscillator. With this basis, we can express the Schrödinger equation in the following form:

$$i\hbar \frac{d}{dt}\langle m_1 m_2|\psi(t)\rangle = \sum_{n_1=0}^{M}\sum_{n_2=0}^{M}\langle m_1, m_2|\hat{H}|n_1, n_2\rangle\langle n_1, n_2|\psi(t)\rangle\,, \qquad (2)$$

where $\hat{H}$ is the quantized Hamiltonian and $|\psi(t)\rangle$ the quantum state at time t of the two-coupled quartic oscillator. For the sake of computation, we have truncated the size of the basis to M. Thus, $\langle m_1, m_2|\hat{H}|n_1, n_2\rangle$ is a four-dimensional matrix. The initial states $|\psi(0)\rangle$ are chosen to be the coherent states $|\alpha_1\rangle \otimes |\alpha_2\rangle$, which provides the connection between the classical and quantum domains. More specifically, the center of the coherent state corresponds precisely to the point (x_1, p_1, x_2, p_2) in the classical phase space, with $\alpha_l = (x_l + ip_l)/\sqrt{2}$. With the defined initial quantum state, we evolve the states of the bipartite quantum system numerically through Eq. (2). Note that more efficient com-

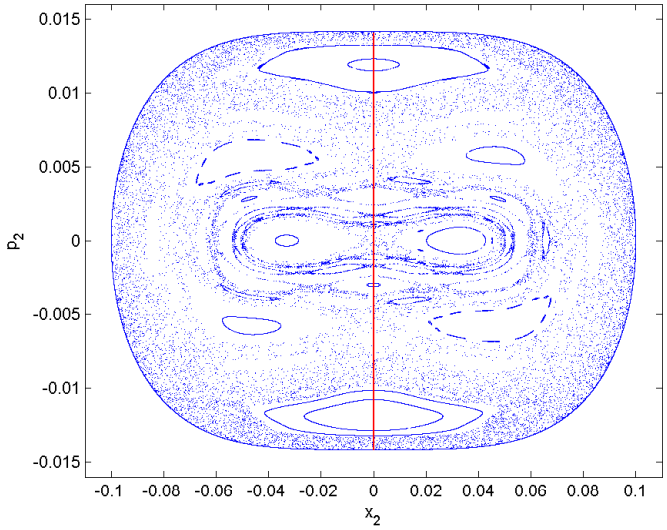

Fig. 2. Classical phase portrait for the coupled quartic oscillator system with coupling constant $\lambda = 0.8$. Note that twenty-nine equally spaced points are selected on the straight line with their corresponding coherent states serve as initial conditions for the entanglement dynamics evaluation.

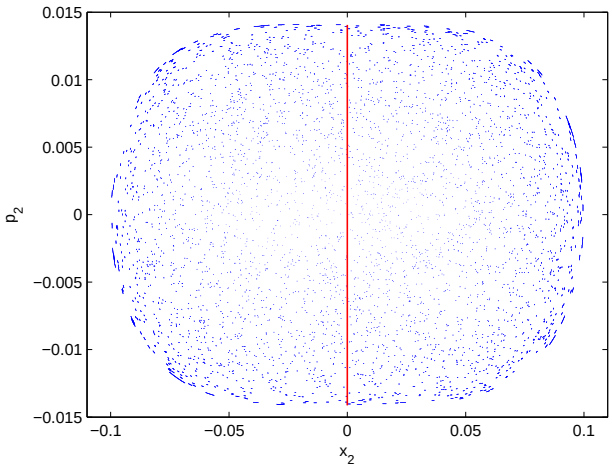

Fig. 3. Classical phase portrait for the coupled quartic oscillator system with coupling constant $\lambda = 2.7$. Note that twenty-nine equally spaced points are selected on the straight line with their corresponding coherent states serve as initial conditions for the entanglement dynamics evaluation.

putation can be achieved with the two-step approach [15–17] since it is suited for the evaluation of the time-evolved states of nonlinear quantum systems.

The entanglement dynamics is determined through the time variation of the von Neumann entropy, which is defined as follow:

$$S_{VN}(t) = -\mathrm{Tr}\left(\rho_1(t)\ln\rho_1(t)\right) , \tag{3}$$

where

$$\rho_1(t) = \mathrm{Tr}_2\left(\rho(t)\right) \tag{4}$$

is the reduced density matrix of oscillator 1. It is obtained by taking the partial trace over oscillator 2 on the density matrix $\rho(t)$ of the two-coupled quantum quartic oscillator, as shown in Eq. (4). Note that since

$$\rho(t) = |\psi(t)\rangle\langle\psi(t)|$$

is pure as our system is assumed to be protected from the decohering environment, the von Neumann entropy is an applicable measure of quantum entanglement. Furthermore, the replacement of $\rho_1(t)$ by the reduced density matrix of oscillator 2,

$$\rho_2(t) = \mathrm{Tr}_1\left(\rho(t)\right) ,$$

in Eq. (3) would not make any difference to the evaluation of the entanglement entropy.

In [3], we had computed the entanglement dynamics by picking coherent states which correspond to points in the classical phase space for each of the dynamical regimes, i.e., the regular, the mixed and the chaotic regimes (refer to Figs. 3 to 5 in [3]). For example, a selection of points in the mixed phase space with some in the regular islands and some in the chaotic sea had been picked (see Fig. 4 of [3]) with the corresponding coherent states serve as initial points for the entanglement dynamics calculation.

We had performed this computation in the quantum and semi-classical regimes. We had employed the parameter $R = \hbar/\Lambda$ to quantify the "quantumness" of the system. Note that $\Lambda = |\alpha_1|^2 + |\alpha_2|^2$ is the action of the system with α_1 and α_2 being the coordinates of the coherent state. When $R \gg 1$, the system is in the quantum regime. On the contrary, when $R \ll 1$, the system is in the semi-classical regime. The semi-classical regime can be approached in either of two ways: $\hbar \to 0$ or $\Lambda \to \infty$. The latter case in fact corresponds to the high-energy approximation in the semi-classical theory. The former case is the one adopted in this paper.

Our earlier results [3] show that the entanglement entropy is much larger in the semi-classical regime. We observe that for both the quantum and semi-classical regimes, the entanglement production is the highest in the pure chaos case, follow by the mixed case, and is lowest in the regular case. We also observe that when the classical system becomes more chaotic, the frequency of oscillation of the entanglement dynamics increases. These results correspond to those reported in the literature. However, for each of the regular, mixed and chaotic case, we observe that identical results are obtained when different initial conditions are employed. This is a surprising result that differs from others

in the literature. This result has led us to conclude in [3] that it is possible for the entanglement dynamics to depend entirely on the global dynamical regime while insensitive to the local classical behavior.

3 Results and Discussion

One may question the conclusion at the end of the last section as follow: is it possible that such global dependence arises from the choice of the initial coherent states? This query is especially relevant for the mixed case as the chosen initial coherent states may lie too close to the edge of the regular island, thus allowing it to sample the chaotic sea surrounding the island. This may have obscured the local dynamical structure and led to the identical results observed.

In this section, we present numerical results that will address these issues. To do this, we need to check the conclusion with a more extensive choice of initial conditions. In consequence, we select a set of initial conditions that lie along the straight lines as shown in Figs. 1, 2 and 3 for the regular, mixed and chaotic case respectively. By considering twenty-nine initial conditions that are equally and closely spaced on each of these straight lines, we can ascertain the validity of the conclusion since these initial conditions correspond to different local dynamical features of the classical phase space.

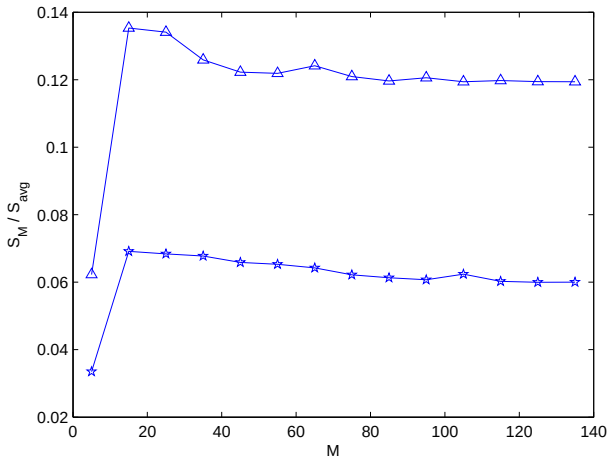

Fig. 4. The maximum and average entanglement entropy versus the basis size M. Note that the computation is based on $\lambda = 0.8$.

Due to the existence of scale invariance in the classical dynamics of Eq. (1) [14], we can select an energy $E = 0.0001$ that is small so that we do not need to use a large basis size for our numerical calculation of the entanglement dynamics. Our computations, as illustrated in Fig. 4, shows that a size of

$M = 135$ is sufficient to ensure convergence for our calculation. With this basis size, we determine the maximum entanglement entropy

$$S_M = \max_t S_{VN}(t)$$

and the mean entanglement entropy

$$S_{avg} = \frac{1}{T}\int_0^T S_{VN}(t)dt$$

of the entanglement dynamics, which are initiated by coherent states that correspond to the set of initial conditions discussed above. In our computation, we consider $\hbar = 1$ for the quantum regime and $\hbar = 0.00001$ for the semi-classical regime. This implies an uncertainty circle with size of order 0.7 for the quantum regime and 0.002 for the semi-classical regime.

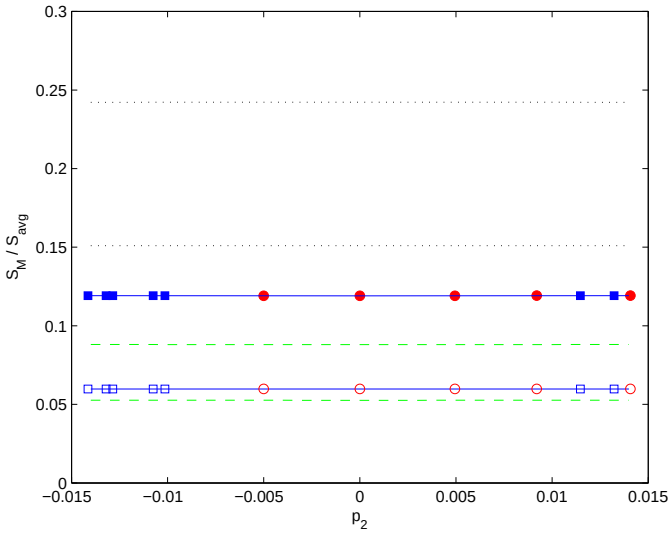

Fig. 5. The maximum and average entanglement entropy for initial coherent state in the quantum regime with $x_1 = x_2 = 0$ but different values of p_1 and p_2. From top to bottom, we have S_M and S_{avg} for $\lambda = 2.7$, S_M for $\lambda = 0.8$ and 0.4, S_{avg} for $\lambda = 0.8$ and 0.4. Note that the parameters used are $\hbar = 1$, $M = 135$ and $E = 0.0001$. Note that the circles and squares represent a sample of the chaotic and regular initial conditions respectively.

Our results for the regular case (dashed lines in Figs. 5 and 6) show a constant S_M and S_{avg} for all the initial coherent states in both the quantum and semi-classical regime. This is in marked contrast to [4] where initial coherent states that situate on the outer tori have a larger entanglement entropy than those that locate at the inner tori. Interestingly, the outcome here for a

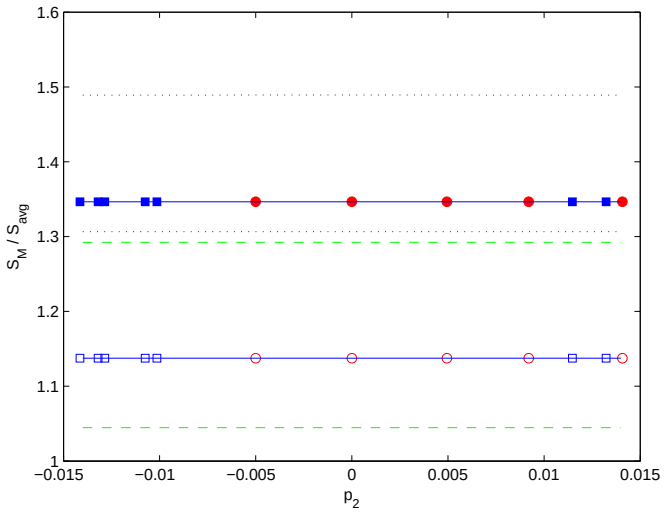

Fig. 6. The maximum and average entanglement entropy for initial coherent state in the semi-classical regime with $x_1 = x_2 = 0$ but different values of p_1 and p_2. From top to bottom, we have S_M for $\lambda = 2.7$ and 0.8, S_{avg} for $\lambda = 2.7$, S_M for $\lambda = 0.4$, S_{avg} for $\lambda = 0.8$ and 0.4. Note that the parameters used are $\hbar = 0.00001$, $M = 135$ and $E = 0.0001$. Note that the circles and squares represent a sample of the chaotic and regular initial conditions respectively.

nonlinear oscillator system is analogous to that of the linear systems discussed in [3].

In addition, Figs. 5 and 6 also show that S_M and S_{avg} attain a constant value for all the chosen initial coherent states in the mixed case (solid lines in the figures). This may be explained by the fact that the uncertainty circle of the initial coherent states in the quantum regime is large enough to sample a mixture of different local phase space structures, leading to the uniform results. However, with similar results obtained in the semi-classical regime, this explanation becomes untenable since the uncertainty circle of the initial coherent states is sufficiently small in this case for the differentiation of local phase space structure.

Finally, we observe a constant S_M and S_{avg} for the chaotic case as shown by the dotted lines in Figs. 5 and 6.

4 Conclusions

By means of a more comprehensive range of initial coherent states that correspond to diverse local dynamical structures in the classical phase space, we have shown that S_M and S_{avg} are insensitive to the choice of the initial coherent states. This is shown to be true for the regular, mixed and chaotic cases in both the quantum and semi-classical regimes for the coupled quartic oscillator

system. We have thus reaffirmed our earlier conclusion that it is possible for the entanglement dynamics to depend solely on the global classical dynamical regime while insensitive to the local classical behavior. An advantage of models that possess such global dependence is that they can serve to generate encoding subspaces that are stable against any errors in the preparation of the initial separable coherent states. We believe that these encoding subspaces will be significant in the design of robust quantum information processing protocol.

References

1.G. Casati and B. Chirikov. Quantum chaos: between order and disorder. Cambridge University Press, 1995.
2.M. Lombardi and A. Matzkin. Entanglement and chaos in the kicked top, Physical Review E, vol. 83, 016207, 2011.
3.N. N. Chung and L. Y. Chew. Dependence of entanglement dynamics on the global classical dynamical regime, Physical Review E, vol. 80, 016204, 2009.
4.S. Zhang and Q. Jie. Quantum-classical correspondence in entanglement production: entropy and classical tori, Physical Review A, vol. 77, 012312, 2008.
5.M. Lombardi and A. Matzkin. Scattering-induced dynamical entanglement and the quantum-classical correspondence, Europhysics Letters, vol. 74, 771-777, 2006.
6.M. Novaes. Entanglement dynamics for two interacting spins, Annals of Physics, vol. 318, 308-315, 2005.
7.P. A. Miller and S. Sarkar. Signatures of chaos in the entanglement of two coupled quantum kicked tops. Physical Review E, vol. 60, 1542-1550, 1999.
8.J. Audretsch, Entangled systems: new directions in quantum physics, Wiley-VCH, 2007.
9.S. Gröblacher, K. Hammerer, M. R. Vanner and M. Aspelmeyer. Observation of strong coupling between a micromechanical resonator and an optical cavity field, Nature, vol. 460, 724-727, 2009.
10.K. Hammerer, M. Wallquist, C. Genes, M. Ludwig, F. Marquardt, P. Treutlein, P. Zoller, J. Ye and H. J. Kimble. Strong coupling of a mechanical oscillator and a single atom, Physical Review Letters, vol. 103, 063005, 2009.
11.B. Yurke and D. Stoler. Generating quantum mechanical superpositions of macroscopically distinguishable states via amplitude dispersion, Physical Review Letters, vol. 57, 13-16, 1986.
12.H. Fujisaki, T. Miyadera and A. Tanaka. Dynamical aspects of quantum entanglement for weakly coupled kicked tops, Physical Review E, vol. 67, 066201, 2003.
13.M. Novaes and M. A. M. De Aguiar. Entanglement and chaos in a square billiard with a magnetic field, Physical Review E, vol. 70, 045201(R), 2004.
14.M. Tomiya, N. Yoshinaga, S. Sakamoto and A. Hirai. A large number of higher-energy eigenvalues of a huge dimensional matrix for a quantum chaotic study of a quartic potential, Computer Physics Communications, vol 169, 313-316, 2005.
15.N. N. Chung and L. Y. Chew. Two-step approach to the dynamics of coupled anharmonic oscillators, Physical Review A, vol. 80, 012103, 2009.
16.N. N. Chung and L. Y. Chew. Energy eigenvalues and squeezing properties of general systems of coupled quantum anharmonic oscillators, Physical Review A, vol. 76, 032113, 2007.
17.C. S. Hsue and J. L. Chern. Two-step approach to one-dimensional anharmonic oscillators, Physical Review D, vol. 29, 643-647, 1984.

Chaotic Modeling and Simulation (CMSIM) 3: 461-468, 2012

A general systems theory for atmospheric flows and atmospheric aerosol size distribution

A. M. Selvam[1]

[1] (Retired) Indian Institute of Tropical Meteorology, Pune 411008, India
(E-mail: amselvam@gmail.com)

Abstract: Atmospheric flows exhibit selfsimilar fractal spacetime fluctuations manifested as the fractal geometry to global cloud cover pattern and inverse power law form for power spectra of meteorological parameters such as windspeed, temperature, rainfall etc. Inverse power law form for power spectra indicate long-range spacetime correlations or non-local connections and is a signature of selforganised criticality generic to dynamical systems in nature such as river flows, population dynamics, heart beat patterns, etc. The physics of selforganised criticality is not yet identified. The author has developed a general systems theory which predicts the observed selforganised criticality as a signature of quantumlike chaos in dynamical systems. The model predictions are (i) The fractal fluctuations can be resolved into an overall logarithmic spiral trajectory with the quasiperiodic Penrose tiling pattern for the internal structure. (ii) The probability distribution represents the power (variance) spectrum for fractal fluctuations and follows universal inverse power law form incorporating the *golden mean*. Such a result that the additive amplitudes of eddies when squared represent probability distribution is observed in the subatomic dynamics of quantum systems such as the electron or photon. Therefore the irregular or unpredictable fractal fluctuations exhibit quantumlike chaos. (iii) Atmospheric aerosols are held in suspension by the vertical velocity distribution (spectrum). The atmospheric aerosol size spectrum is derived in terms of the universal inverse power law characterizing atmospheric eddy energy spectrum. Model predicted spectrum is in agreement with the following two experimentally determined atmospheric aerosol data sets, (i) SAFARI 2000 CV-580 Aerosol Data, Dry Season 2000 (CARG) (ii) World Data Centre Aerosols data sets for the three stations Ny Ålesund, Pallas and Hohenpeissenberg.
Keywords: Universal atmospheric aerosol size spectrum, SAFARI 2000 aerosol size spectra, World data center aerosol size spectra, Fractal fluctuations in atmospheric flows, Chaos and nonlinear dynamics..

1 Introduction

Information on the size distribution of atmospheric aerosols is important for the understanding of the physical processes relating to the studies in weather, climate, atmospheric electricity, air pollution and aerosol physics. Aerosols affect the radiative balance of the Earth/atmosphere system via the direct effect whereby they scatter and absorb solar and terrestrial radiation, and via the indirect effect whereby they modify the microphysical properties of clouds thereby affecting the radiative properties and lifetime of clouds [1]. At present

Received: 8 September 2011 / Accepted 30 March 2012

ISSN 2241-0503

empirical models for the size distribution of atmospheric suspended particulates is used for quantitative estimation of earth-atmosphere radiation budget related to climate warming/cooling trends. The empirical models for different locations at different atmospheric conditions, however, exhibit similarity in shape implying a common universal physical mechanism governing the organization of the shape of the size spectrum.

Atmospheric flows exhibit selfsimilar fractal fluctuations generic to dynamical systems in nature. Self-similarity implies long-range space-time correlations identified as self-organized criticality [2]. The physics of self-organized criticality ubiquitous to dynamical systems in nature and in finite precision computer realizations of non-linear numerical models of dynamical systems is not yet identified. During the past three decades, Lovejoy and his group [3] have done extensive observational and theoretical studies of fractal nature of atmospheric flows and emphasize the urgent need to formulate and incorporate quantitative theoretical concepts of fractals in mainstream classical meteorological theory. The empirical analyses summarized by Lovejoy and Schertzer [3] directly demonstrate the strong scale dependencies of many atmospheric fields, showing that they depend in a power law manner on the space–time scales over which they are measured. In spite of intense efforts over more than 50 years, analytic approaches have been surprisingly ineffective at deducing the statistical properties of turbulence. Conclusions about anthropogenic influences on the atmosphere can only be drawn with respect to the null hypothesis, i.e. one requires a theory of the natural variability, including knowledge of the probabilities of the extremes at various resolutions. At present, the null hypotheses are classical so that they assume there are no long-range statistical dependencies and that the probabilities are thin-tailed (i.e., exponential). However observations show that cascades involve long-range dependencies and (typically) have fat tailed (algebraic) distributions in which extreme events occur much more frequently and can persist for much longer than classical theory would allow [3].

A general systems theory for the observed fractal space-time fluctuations of dynamical systems [4-7] helps formulate a simple model to explain the observed vertical distribution of number concentration and size spectra of atmospheric aerosols. The atmospheric aerosol size spectrum is derived in terms of the universal inverse power law characterizing atmospheric eddy energy spectrum. A universal (scale independent) spectrum is derived for suspended atmospheric particulate size distribution expressed as a function of the golden mean τ ($\approx$ 1.618), the total number concentration and the mean volume radius (or diameter) of the particulate size spectrum. Knowledge of the mean volume radius and total number concentration is sufficient to compute the total particulate size spectrum at any location. The physical basis and the theory relating to the model are discussed in Sec. 2. The model predictions are (i) Fractal fluctuations can be resolved into an overall logarithmic spiral trajectory with the quasiperiodic Penrose tiling pattern for the internal structure. (ii) The probability distribution of fractal space-time fluctuations represents the power (variance) spectrum for fractal fluctuations and follows universal inverse power

law form incorporating the *golden mean*. Such a result that the additive amplitudes of eddies when squared represent probability distribution is observed in the subatomic dynamics of quantum systems such as the electron or photon. Therefore the irregular or unpredictable fractal fluctuations exhibit quantumlike chaos. (iii) Atmospheric aerosols are held in suspension by the vertical velocity distribution (spectrum). The normalised atmospheric aerosol size spectrum is derived in terms of the universal inverse power law characterizing atmospheric eddy energy spectrum. Model predicted spectrum is in agreement with the following two experimentally determined atmospheric aerosol data sets, (i) SAFARI 2000 CV-580 Aerosol Data, Dry Season 2000 (CARG) (ii) World Data Centre Aerosols data sets for the three stations Ny Ålesund, Pallas and Hohenpeissenberg.

2 General systems theory for atmospheric aerosol size spectrum

The atmospheric eddies hold in suspension the aerosols and thus the size spectrum of the atmospheric aerosols is dependent on the vertical velocity spectrum of the atmospheric eddies. Atmospheric air flow is turbulent, i.e., consists of irregular fluctuations of all space-time scales characterized by a broadband spectrum of eddies. The suspended aerosols will also exhibit a broadband size spectrum closely related to the atmospheric eddy energy spectrum.

A general systems theory for turbulent fluid flows predicts that the eddy energy spectrum, i.e., the variance (square of eddy amplitude) spectrum is the same as the probability distribution P of the eddy amplitudes, i.e. the vertical velocity W values. Such a result that the additive amplitudes of eddies, when squared, represent the probabilities is exhibited by the subatomic dynamics of quantum systems such as the electron or photon. Therefore the unpredictable or irregular fractal space-time fluctuations generic to dynamical systems in nature, such as atmospheric flows is a signature of quantum-like chaos. The general systems theory for turbulent fluid flows predicts [4-7] that the atmospheric eddy energy spectrum follows inverse power law form incorporating the *golden mean* τ [7] and the normalized deviation t for values of $t \geq 1$ and $t \leq -1$ given as $P = \tau^{-4t}$. Normalised deviation t ranging from -1 to +1 corresponds to the primary eddy growth region. In this region the probability density distribution P is shown to be equal to $P = \tau^{-4k}$ where k is the fractional volume dilution by eddy mixing equal to $k = \sqrt{\frac{\pi}{2z}}$ where z is the eddy length scale ratio ranging from 2 to 10 and the corresponding to t values are equal to 1.1-(z/10).

The normalised height is also represented by z. The model predicted probability density distribution P along with the corresponding statistical normal distribution with probability values plotted on linear and logarithmic scales respectively on the left and right hand sides are shown in Figure 1. The model predicted probability distribution P for fractal space-time fluctuations is very close to the statistical normal distribution for normalized deviation t values less

than 2 as seen on the left hand side of Figure 1. The model predicts progressively higher values of probability P for values of t greater than 2 as seen on a logarithmic plot on the right hand side of Figure 1 and may explain the reported *fat tail* for probability distributions of various physical parameters [8].

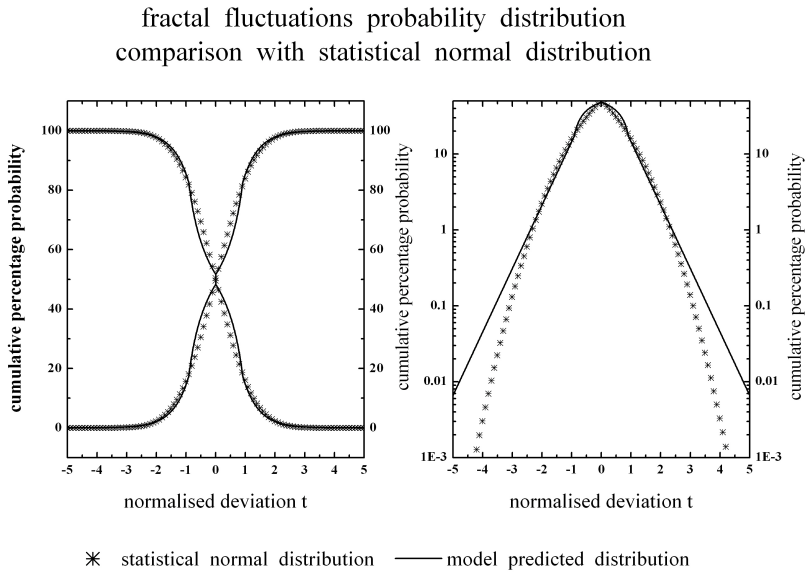

Figure 1. Probability distribution of fractal fluctuations. Comparison of theoretical with statistical normal distribution.

The atmospheric eddies hold in suspension the aerosols and thus the size spectrum of the atmospheric aerosols is dependent on the vertical velocity spectrum of the atmospheric eddies. Atmospheric air flow is turbulent, i.e., consists of irregular fluctuations of all space-time scales characterized by a broadband spectrum of eddies. The suspended aerosols will also exhibit a broadband size spectrum closely related to the atmospheric eddy energy spectrum.

The normalized aerosol size spectrum is obtained by plotting a graph of normalized aerosol concentration $\frac{1}{N}\frac{\mathrm{d}N}{\mathrm{d}(\ln r_{\mathrm{n}})} = \frac{3}{2}P\tau^{2t}$ versus the normalized aerosol radius $r_{\mathrm{n}} = r/r_a = \tau^{2t/3}$ where r_a is the mean volume radius, N the total number concentration and dN the number concentration in the size interval dr. The normalized aerosol size spectrum is derived directly from the universal probability density P distribution characteristics of fractal fluctuations and is independent of the normalised height z of measurement and is universal for aerosols in turbulent atmospheric flows. The aerosol size spectrum is computed

starting from the minimum size, the corresponding probability density P refers to the cumulative probability density starting from 1 and is computed as equal to $P = 1 - \tau^{-4t}$. The model predicted universal scale-free aerosol size spectrum is shown in Figure 2.

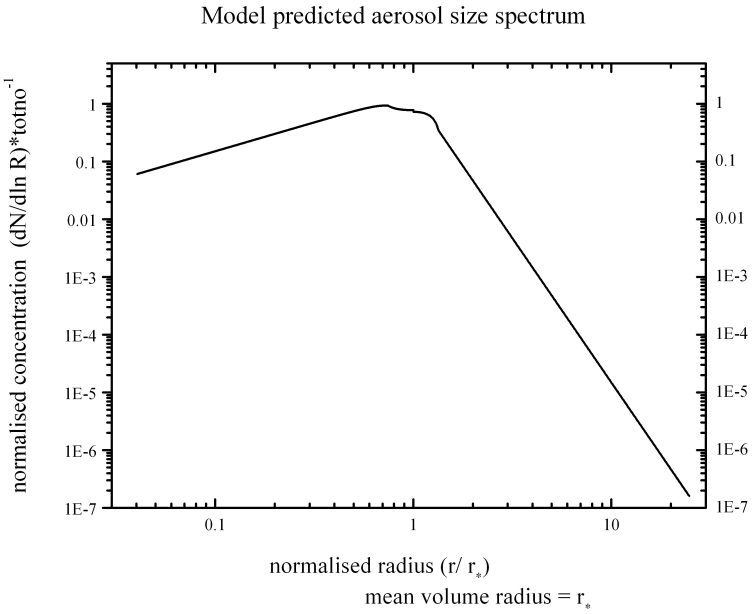

Figure 2. Model predicted aerosol size spectrum

3 Comparison of Observed and Model Predicted Aerosol Size Spectra

The following two data sets were used for comparison of observed with model predicted aerosol size spectrum:
(i) SAFARI 2000 CV-580 Aerosol Data, Dry Season 2000 (CARG). The Cloud and Aerosol Research Group (CARG) of the University of Washington participated in the SAFARI-2000 Dry Season Aircraft campaign with their Convair-580 research aircraft. This campaign covered five countries in southern Africa from August 10 through September 18, 2000. The UW Technical Report for the SAFARI 2000 Project (http://daac.ornl.gov/data/safari2k/atmospheric/CV-580/comp/SAFARI-MASTER.pdf) gives a complete detailed guide to the extensive measurements obtained aboard the UW Convair-580 aircraft in support of SAFARI 2000 [Hobbs PV. SAFARI 2000 CV-580 Aerosol and Cloud Data, Dry Season 2000 (CARG). Data set. Available on-line (http://www.daac.ornl.gov/) from Oak Ridge National Laboratory Distributed Active Archive Center, Oak Ridge, Tennessee, U.S.A. doi:10.3334/ORNLDAAC/710, 2004]. The mean and standard deviation of normalised aerosol size spectrum was computed for

245037 and 189761 individual spectra respectively for *pcasp* and *tsi3320* aerosol measurement instrument systems and shown in Figure 3 along with the model predicted universal normalized aerosol size spectrum.
(ii) Aerosol size distributions for three land stations (Ny Ålesund, Pallas and Hohenpeissenberg) were obtained from World Data Centre for Aerosols (http://wdca.jrc.it/data/parameters/data_size.html) at The Aerosol Size Distribution Data Archive. The annual means (2001 to 2004 for the first two and 2001 to 2005 for the third staion) normalized aerosol size spectra with associated standard deviations were computed for the three stations Ny Ålesund, Pallas and Hohenpeissenberg for each year and shown in Figure 4.

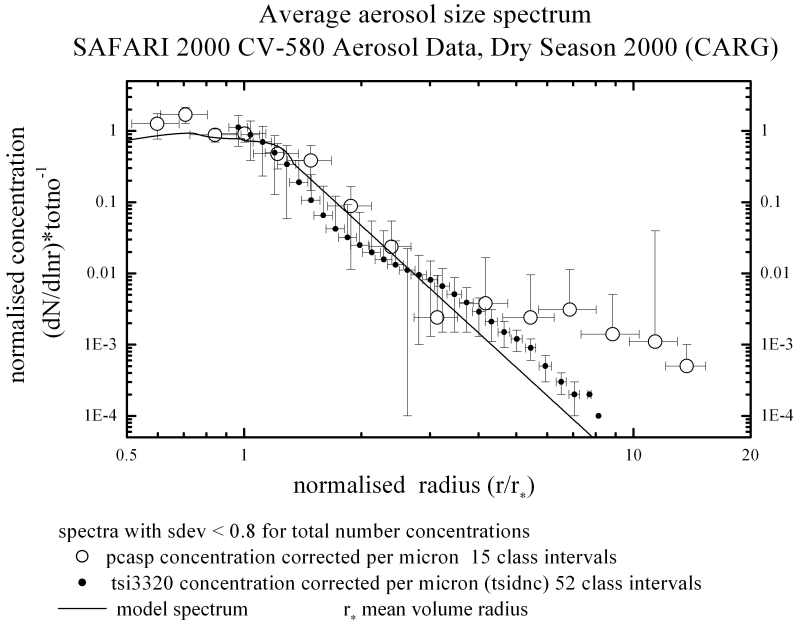

Figure3. Average aerosol size spectrum for SAFARI 2000 CV-580 aerosol size spectra and comparison with model prediction. Error bars indicate one standard deviation on either side of the mean

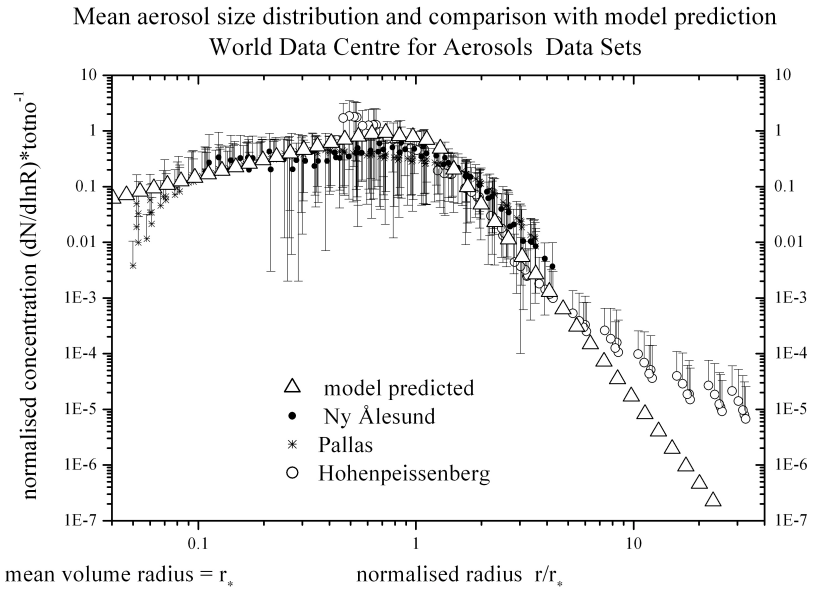

Figure 4. Mean aerosol size spectrum for World data center aerosols data sets and comparison with model prediction. Error bars indicate one standard deviation on either side of the mean

4 Conclusions

There is a close agreement between the model predicted and the observed aerosol size distributions for the two aerosol data sets (SAFARI 2000 and World Data Center) used in the study. SAFARI 2000 aerosol size distributions reported by Haywood *et al*. [1] also show similar shape for the distributions. The physical hypothesis relating to the dynamics of the atmospheric eddy systems proposed in the present paper can be extended to other planetary, solar and stellar atmospheres.

References

1. J. Haywood, P. Francis, O. Dubovik, M. Glew and B. Holben. Comparison of aerosol size distributions, radiative properties, and optical depths determined by aircraft observations. *Journal of Geophysical Research*, 108:NO. D13, 8471, pp. SAF 7 – 1 to 12, 2003. doi:10.1029/2002JD002250.

2. P .C. Bak, C. Tang and K. Wiesenfeld. Self-organized criticality. *Phys. Rev. A*., 38:364–374, 1988.

3. S. Lovejoy and D. Schertzer. Towards a new synthesis for atmospheric dynamics: space-time cascades. *Atmos. Res*., 96:1-52, 2010. doi:10.1016/j.atmosres.2010.01.004. http://physics.mcgill.ca/~gang/eprints/eprintLovejoy/neweprint/Atmos.Res.8.3.10.finalsdarticle.pdf.

4. A. M. Selvam. Deterministic chaos, fractals and quantumlike mechanics in atmospheric flows. *Can. J. Phys*., 68:831–841, 1990. http://xxx.lanl.gov/html/physics/0010046

5. A. M. Selvam. A general systems theory for chaos, quantum mechanics and gravity for dynamical systems of all space-time scales. *ELECTROMAGNETIC PHENOMENA*, 5 No.2 (15):160–176, 2005. http://arxiv.org/pdf/physics/0503028; http://www.emph.com.ua/15/selvam.htm.

6. .A. M. Selvam. *Chaotic Climate Dynamics*. Luniver Press, U.K., 2007.

7. A. M. Selvam. Fractal fluctuations and statistical normal distribution. *Fractals*, 17 (3):333-249, 2009.

8. M. Buchanan. Power laws and the new science of complexity management. *Strategy and Business Issue*, 34:70–79, 2004.

Chaotic Modeling and Simulation (CMSIM) 3: 469-476, 2012

Chaos and Complexity Models in Sustainable Building Simulation

Xiaoshu Lu[1,2], Charles Kibert[3], Martti Viljanen[1]

[1]Department of Civil and Structural Engineering, School of Engineering, Aalto University, PO Box 12100, FIN-02150, Espoo, Finland
E-mail: xiaoshu@cc.hut.fi
[2]Finnish Institute of Occupational Health, Finland
[3]Powell Center for Construction & Environment, University of Florida, PO Box 115703, Gainesville, Florida 32611-5703 USA

Abstract: This paper intends to provide suggestions of how sustainable building simulation might profit from mathematical models derived from chaos and complexity approaches. It notes that with the increasing complexity of building systems which are capable of intelligently adjusting buildings' performance from the environment and occupant behaviour and adapting to environmental extremes, building performance simulation is becoming more crucial and heading towards new challenges, dimensions, concepts, and theories beyond the traditional ones. The paper then goes on to describe how chaos and complexity theory has been applied in modelling building systems and behaviour, and to identify the scarcity of literature and the need for a suitable methodology of linking chaos and complexity approaches to mathematical models in building sustainable studies. Chaotic models are proposed thereafter for modelling energy consumption, nonlinear moisture diffusion, and building material properties in building simulation. This paper provides an update on the current simulation models for sustainable buildings.

Keywords: Chaos and complexity theory, Sustainable building simulation, Energy consumption, Moisture diffusion and Material properties.

1. Introduction

Buildings represent a large share of the world's end-use energy consumption. Due to rapid worldwide increases in energy consumption, climate change driven by global warming, and rising energy shortages, there is no doubt that renewable energy and sustainable buildings will play a major role in the future. Today, sustainable buildings are seen as a vital element of a much larger concept of sustainable development that aims to meet human needs while preserving the environment so that the needs can be met not only in the present, but in the indefinite future [1]. Moreover, the concept itself keeps on evolving

Received: 29 June 2011 / Accepted 30 March 2012

ISSN 2241-0503

and resulting in iterations of sustainability [2]. Technically, sustainable buildings require integration of a variety of computer-based complex systems which are capable of intelligently adjusting their performance based on the environment and occupant behaviour and intelligently adapting to environmental extremes [2].

With the increasing complexity of building systems, simulation based design and predictive control of building performances are becoming more and more important for a sustainable energy future. Consequently, this makes building performance models more complex and crucial and they are heading towards new challenges, dimensions, concepts, and theoretical framework beyond the traditional building simulation theories. It has been suggested that as a basis chaos and complexity theory is valid and can handle the increasing complexity of building systems that have dynamic interactions among the building systems on the one hand, and the environment and occupant behaviour on the other. In this paper we do not distinguish between chaos and complexity theories even though there has been a debate about their differences [3].

The chaos models have already been applied to some problems in building simulation applications. Chow et al. investigated chaos phenomena of the dynamic behaviour of mixed convection and air-conditioning systems for buildings with thermal control [4]. Weng et al. applied chaos theory to the study of backdraft phenomenon in room fires [5]. Morimoto et al. studied an intelligent control technique for keeping better quality of fruit during the storage process [6]. For humidity control purpose, the sampled relative humidity data in storage house were measured and analysed. Chaos phenomenon was identified in such measured relative humidity data during daytime hours.

In spite of the studies discussed above, the application of chaos theory to building performance simulation, especially to sustainable buildings, is still in its infancy. Building performance simulation models can be roughly classified into either the physical model or the black-box approach. Some may be difficult to categorise in this way. As far as the physical model is concerned, there is a voluminous literature on the models ranging from detailed to local thermal analysis of energy demand, passive design, environmental comfort and the response of control [7,8]. These physical models often require sufficient information on systems, control and environmental parameters for buildings. The output of the model is only as accurate as the input data.

Presently input data for buildings are often poorly defined, which creates ambiguity or uncertainty in interpreting the output. This is the general drawback of these models. Therefore, for many practical applications, a black-box approach, a model without internal mechanisms or physical structure, is often adopted. For example, neutral networks, fuzzy logic, and time series models [9,10] are generally better suited for prediction. However, these models have several limitations. Take neural networks as an example. Firstly, large

experimental input and output data are needed in order to build neural networks which can be difficult and expensive to obtain in practice. Secondly, they are susceptible to over-training. Above all, the models have been criticised as 'black box' models with no explanation of the underlying mechanisms that drive the study systems [11].

More specifically, as for sustainable buildings, the current models often lack the long-term economics factors, evolving factors, and flexibility necessary for dynamic predictions. These weaknesses and the current status of sustainable building simulation models have encouraged us to focus instead on a chaos-based model incorporating physical model to enhance our understanding and prediction of building physical behaviour. Chaos theory is characterised by the so-called 'butterfly effect' [12]. It is the propensity of a system to be sensitive to initial conditions so that the system becomes unpredictable over time. Yet, a chaotic process is not totally random and has broadened existing deterministic patterns with some kind of structure and order [12]. This paper extends the literature by proposing potential chaotic models in sustainable building simulation. Below we describe three such models. The first is a building energy consumption model. The second deals with a nonlinear moisture diffusion model. The third is related to building material properties.

2. Building Energy Consumption Model

Swan provided an up-to-date review of various simulation models used for modelling residential sector energy consumption and sustainability [13]. Most models rely on input data whose levels of details can vary dramatically. Li presented an overview of literature regarding long-term energy demand and CO_2 emission forecast scenarios [14]. These reviews reflect general modelling approaches currently in existence for sustainable buildings. Two approaches are generally adopted: top-down and bottom-up. The top-down approach utilises historic aggregate energy values and regresses the energy consumption of the housing stock as a function of top-level variables such as macroeconomic indicators. While the generally employed techniques account for future technology penetration based on historic rates of change, they lack of evolving factors. Hence an inherent drawback of the generally employed approaches is that there is no guarantee that values derived from the past will remain valid in the future, especially given the fact that the levels of details of input data vary significantly [13].

The bottom-up approach extrapolates the estimated energy consumption of a representative set of individual houses to regional and national levels, and consists of two distinct methodologies: the statistical method and the engineering method [13]. Methodologically, extrapolation has been questioned for many good reasons. It is therefore noted that the statistical technique is hampered by multicollinearity resulting in poor prediction of certain end-uses

while the engineering technique requires more inputs and has difficulty estimating the unspecified loads [13, 15].

The major disadvantage of these models is their lack of flexibility due to the fact that there is no deterministic structure provided to characterise the data. In this context, chaos theory offers a solid theoretical and methodological foundation for interpreting the fundamental deterministic structure of the data which present the increasingly complexity of building systems. Karatasou applied chaos theory in analysing time series data on building energy consumption [16]. The correlation dimension 3.47 and largest Lyapunov exponent 0.047 were estimated for the data, which indicates that chaotic characteristics exist in the energy consumption data. Therefore, chaos theory techniques can be used to model and predict buildings energy consumption.

3. Strong Nonlinear Moisture Diffusion Model

Building envelopes can be susceptible to moisture accumulation which may cause mould growth and the deterioration of both occupant health and building materials. A certain duration of exposure conditions, such as humidity, temperature, and exposure time, is required for the growth of organisms and the start of the deterioration process. Critical exposure duration depends on the particular exposure and material. Take a critical moisture level as an example. If the moisture content in the material exceeds the critical level, there is a risk of damage [17] and mould growth [18]. Trechsel summarised that the critical moisture level can be presented as critical factors such as 'the critical moisture content' and 'the critical accumulative exposure time' [19]. He emphasised that with qualitative criteria it is not possible to assess the risk. Qualitative criteria can be used only if performance limit states are known which need statistical data. Evidence has shown the existence of inherent randomness and nonlinearity in mould growth and the data [18]. Therefore, the moisture transfer process manifestly has chaos.

From a physical modelling point of view, heat and moisture transfer phenomena in a medium are governed by heat or diffusion equations which are partial differential equations. For a homogeneous and isotropic medium, the diffusivity coefficient is often assumed to be constant in the entire domain under study. In inhomogeneous media, it depends on the coordinates [20]. Until now, there is no model has considered time-dependent diffusivity. However, time-dependent diffusivity, which might be due to the time-dependent perturbation of environment such as sudden structural change, is an optional explanation for the critical moisture level.

Yao studied one-dimensional Kuramoto–Sivashinsky (KS) equation, a nonlinear partial differential equation, in the hope of clarify the role of the time-dependent governing parameter and the sensitivity of the long-time solution to initial conditions [21]:

$$u_t + 4u_{xxxx} + \lambda(u_{xx} + uu_x) = 0 \quad (1)$$

Nonlinear stability analysis was investigated with respect to time-dependent λ. After a certain time (t =4), chaotic behavior was observed.

It is not difficult to see that the KS equation and nonlinear moisture diffusion equations do not differ significantly. Thus the KS equation example is expected to more easily expose major points and hopefully identify open questions that are related to the critical moisture level or mould phenomena as related to chaos phenomena.

4. Material Properties Model

Porous media have played a major role in building engineering applications. They are important elements of heat and mass conservation for buildings and have been extensively studied [22]. A porous material has a unique structure of complex geometry which is characterised by the presence of a solid matrix and void phases with porosity. The heat and mass transport behaviour of porous media is largely governed by the interactions among coexisting components. These interactions occur through interfaces. Theoretically, transport processes in a porous medium domain may be described by a continuum at the microscopic level based on the Navier-Stokes equations for example, as taking into account the multi-phase nature of the domain. However, for most cases this is impractical because of the inability to both describe the complex geometry and trace a large number of interfacial boundaries for the porous domain. Therefore, the porous media models are often constructed through averaging the governing equations, for example Navier-Stokes equations, in continua at the microscopic level over a length scale such as representative elementary volume [23]. During the averaging process some integrals are performed, introducing a weighted average of the relevant variables, parameters and properties which can be determined by laboratory and field measurements.

However, both laboratory and field measurements are often tedious, time consuming and expensive. This has motivated researchers toward the development of mathematical modeling approaches based on routinely measured properties. In general, three types of mathematical models are used to model material transport properties: empirical, bundle of tubes, and network models [24]. The empirical models provide a set of analytical functions to fit the measurement data for material properties. The model has the advantage of simplicity but the disadvantage of limited flexibility and adjustability and hence low reliability.

Depending on how they represent the geometry of the material, both the bundle of tubes and the network models rely on the pore structure, such as pore distribution, connectivity and tortuosity, to derive the material's transport properties. These models are also called pore-distribution models and were

pioneered by Fatt [25-27]. The bundle of tubes model approximates the pore structure in a fairly simple way, for example, a set of parallel tubes [24]. Networks models approximate the pore structure by a lattice of tubes and throats of various geometrical shapes on the microscopic scale. Creating a network model is laborious and not straightforward especially for 3D models [28].

Most importantly, these models, or current state of material property modelling approaches, are case sensitive depending on the excited boundary or the environment. Therefore, variations of material properties under different conditions are large, which has been a challenge for modellers. On a longer time scale, **a** large quantity of data is often needed to build the model and this can be difficult and expensive to accomplish in practice. In addition, in a wide environment setting when different environmental phenomena overlap, material properties become complicated and difficult to predict [29]. This is due to the lack of a deterministic structure or a core mechanism which characterises the material transport properties. Chaos theory provides a tool to exploit the underlying structures that appear random or unpredictable under traditional analysis.

Stazi et al. applied chaos theory to investigate the hygrometric properties of building materials, such as adsorption and suction curves [29]. The constitute relationship of a material's water content and the environment humidity was modelled on the basis of fractal geometry using the material's pore radius as:

$$u = u(\phi, D) \tag{2}$$

where u is the hygroscopic content inside the material and ϕ the relative humidity of the material. Their relationship was determined through finding the material 's fractal dimension of water inside the pores, D, which was 2.5265 for mortar [29].

The novelty of the model lies in its ability to construct the relationship between the water content inside the material and the relative humidity of the environment based on the material's geometric property characterised by the fractal dimension. The knowledge of the fractal dimension of the pore spacing in a porous medium is enough to work out the suction and adsorption curves of the material. It is, therefore, natural for us to consider chaos theory as a source of inspiration to envisage the importance of the concerns raised in research in different fields of building material properties.

5. Conclusions

This paper suggests some new thinking about how to update the current status of simulation models for sustainable buildings. Three chaotic models are proposed. The first is the building energy consumption model because chaotic characteristics have been observed in the specific energy consumption data. The second deals with the investigation of nonlinearity of the moisture diffusion

model. The third model involves the investigation of material physical properties. The conclusion to be drawn is that chaos theory may reflect real situations, deepen our understanding, and make predictions more realistic in sustainable building simulation.

References

1. Wikipedia-The Free Encyclopedia, Sustainable Development. http://en.wikipedia.org/wiki/Sustainable_development, June, 2008.
2. C. Du Plessis. Thinking about the Day after Tomorrow. New Perspectives on Sustainable Building. *Rethinking Sustainable Construction 2006 Conference*, Sarasota, Florida, USA 2006.
3. R.C. Zahra. From Chaos to Cohesion—Complexity in Tourism Structures: An Analysis of New Zealand's Regional Tourism Organizations. *Tourism Management* 28: 854-862, 2007.
4. K. Chow, G. Xin, A. Liu. A Further Study on Multiple Attractors of Mixed Convection in Confined Spaces. *Building and Environment* 40: 1021-1031, 2005.
5. W.G. Weng, W.C. Fan. Nonlinear Analysis of the Backdraft Phenomenon in Room Fires. *Fire Safety Journal* 39: 474-464, 2004.
6. T. Morimoto, Y. Hashimoto. An Intelligent Control for Greenhouse Automation, Oriented by the Concepts of SPA and SFA- An Application to a Post-harvest Process. *Computers and Electronics in Agriculture* 29: 3-20, 2004.
7. X. Lu, D. Clements-Croome, M. Viljanen. Past, Present and Future Mathematical Models for Buildings: Focus on Intelligent Buildings (Part 1). *Intelligent Building International* 1:22-38, 2009.
8. X. Lu, D. Clements-Croome, M. Viljanen. Past, Present and Future Mathematical Models for Buildings: Focus on Intelligent Buildings (Part 2). *Intelligent Building International* 2:131-141, 2009.
9. A.I. Dounis, C. Cariscos. Advanced Control Systems Engineering for Energy and Comfort Management in a Building Environment : A Review. *Renewable and Sustainable Energy Reviews* 13: 1246-1261, 2009.
10. D. Popescu, F. Ungureanu, A. Henandez-Guerrero. Simulation Models for the Analysis of Space Heat Consumption of Buildings. *Energy* 34: 1447-1453, 2009.
11. M. Aydinalp, V.I. Ugursal, A. Fung. Modeling of the Appliance, Lighting, and Space-cooling Energy Consumptions in the Residential Sector Using Neural Networks. *Applied Energy* 72: 87–110, 2002.
12. E. Lorenz. Deterministic Nonperiodic Flow. *Journal of Atmospheric Science* 20: 130–141, 1963.
13. L.G. Swan, V.I. Ugursal. Modeling of End-use Energy Consumption in the Residential Sector: A Review of Modeling Techniques. *Renewable and Sustainable Energy Reviews* 13: 1819-1835, 2009.
14. J. Li. Towards a Low-carbon Future in China's Building Sector-A Review of Energy and Climate Models Forecast. *Energy Policy* 36: 1736-1747, 2008.
15. B.M. Larsen, R. Nesbakken. Household Electricity End-use Consumption: Results from Econometric and Engineering Models. *Energy Economics* 26: 179–200, 2004.
16. S. Karatasou, M. Santamouris. Detection of Low-dimensional Chaos in Buildings Energy Consumption Time Series. *Communications in Nonlinear Science and Numerical Simulation* 15: 1603-1612, 2010.

17. V. Leivo, J. Rantala. Moisture Behaviour of Slab-on-ground Structures in Operating Conditions: Steady-state Analysis. *Construction and Building Materials* 22: 526-531, 2008.
18. H.J. Moon, G.A. Augenbroe. A Mixed Simulation Approach to Analyse Mold Growth under Uncertainty. *Ninth International IBPSA Conference,* Montreal, Canada*,* August 15-18, 2005.
19. H.R. Trechsel. Moisture Analysis and Condensation Control in Building Envelopes. *ASTM Manual* 40, Philadelphia, USA, 2001.
20. R.C. Gaur, N.K. Bansal. Effect of Moisture Transfer across Building Components on Room Temperature. *Building and Environment* 37: 11-17, 2002.
21. L-S, Yao. Is a Direct Numerical Simulation of Chaos Possible? A Study of Model Nonlinearity. *International Journal of Heat and Mass Transfer* 20: 2200-2207, 2007.
22. X. Lu. Modeling Heat and Moisture Transfer in Buildings: (I) Model Program. *Energy and Buildings* 34: 1033-1043, 2002.
23. J. Bear. *Dynamics of Fluids in Porous Media,* Elsevier: New York, NY, USA, 1972.
24. F.A.L. Dullien. *Porous Media: Fluid Transport and Pore Structure*, Academic Press: New York, 1979.
25. I. Fatt. The Network Model of Porous Media I. Capillary Pressure Characteristics. *Trans. AIME*. 207: 144–159, 1956.
26. I. Fatt. The Network Model of Porous Media II. Dynamic Properties of a Single Size Tube Network. *Trans. AIME*. 207: 160-163, 1956.
27. I. Fatt. The Network Model of Porous Media III. Dynamic Properties of Networks with Tube Radius Distribution. *Trans. AIME*. 207: 164-181, 1956.
28. W.B. Lindquist. Network Flow Model Studies and 3D Pore Structure. *Contemporary Mathematics* 295: 355-366, 2002.
29. A. Stazi, M. D'Orazio, E. Quagliarini. In-life Prediction of Hygrometric Behaviour of Buildings Materials: An Application of Fractal Geometry to the Determination of Adsorption and Suction Properties. *Building and Environment* 37: 733–739, 2002.

Chaotic Modeling and Simulation (CMSIM) 3: 477–483, 2012

Search for Deterministic Nonlinearity in the Light Curves of the Black Hole System GRS 1915+105

K. P. Harikrishnan[1], R. Misra[2], and G. Ambika[3]

[1] Department of Physics, The Cochin College, Cochin - 682 002, India
(E-mail: *kp_hk2002@yahoo.co.in*)
[2] Inter University Centre for Astronomy and Astrophysics, Pune - 411 007
(E-mail: `rmisra@iucaa.ernet.in`)
[3] Indian Institute of Science Education and Research, Pune - 411 021, India
(E-mail: `g.ambika@iiserpune.ac.in`)

Abstract. GRS 1915+105 is prominent black hole system exhibiting variability over a wide range of time scales and the light curves from the source have been classified into 12 temporal states. Here we undertake an analysis of the light curves from all the states using three important quantifiers from nonlinear time series analysis, namely, the correlation dimension (D_2), the correlation entropy (K_2) and singular value decomposition (SVD). An important aspect of our analysis is that, for estimating these quantifiers, we use algorithmic schemes which we have proposed recently and tested successfully on synthetic as well as practical time series from various fields. We show that nearly half of the 12 temporal states exhibit deviation from randomness and their complex temporal behavior can be approximated by a few (3 or 4) coupled ordinary differential equations. Based on our results, the 12 states can be broadly classified into three from a dynamical perspective: purely stochastic with D2 tending to infinity, affected by colored noise and those which are potential candidates for deterministic non linearity with $D2 \leq 4$. Our results could be important for a better understanding of the processes that generate the light curves and hence for modeling the temporal behavior of such complex systems. A more detailed analysis and results are presented elsewhere [1].
Keywords: Time Series Analysis, Applied Chaos, Black Hole Binaries.

1 Introduction

Most of the systems in Nature are described by models which are inherently nonlinear. Since the discovery of *deterministic chaos* a few decades back and the development of various techniques in subsequent years, there remained the exciting prospect of a better understanding of the complex behavior shown by various natural systems in terms of simple nonlinear models. A large number of techniques from nonlinear dynamics are routinely being employed for this

Received: 29 June 2011 / Accepted: 30 March 2012

ISSN 2241-0503

purpose. For example, see Hilborn [2] and Lakshmanan & Rajasekhar [3] for details.

Astrophysical objects are among the most interesting real world syatems where methods from nonlinear dynamics have been attempted right from the development of chaos theory. Important examples include the analysis of variable stars [4] to understand the nature of variability, the study of the temporal variations in the sun spot activities [5] and to develop possible measures to differentiate between AGNs and black holes [6]. One major limitation regarding the analysis of astrophysical objects is that the only available information regarding the source is the light intensity variations emitted by it, called the *light curve*, over which one has no control. It is a single scalar variable recorded as a function of time, namely, a *time series*. Thus the main task in the analysis is to understand the nature of variability and to reconstruct the underlying model using the methods of time series analysis.

A number of computational schemes and measures are used for the nonlinear time series analysis as discussed by many authors [7,8]. The most important quantifiers among these are the correlation dimension (D_2) and the correlation entropy (K_2). We have recently proposed automated algorithmic schemes [9,10] for computation of D_2 and K_2 from time series based on the delay embedding technique and applied them successfully to various types of time series data. In this work, we apply these computational schemes to analyse the X-ray light curves from a very prominent black hole binary, GRS 1915+105.

2 Analysis of the Light Curves

Among the most important nonlinearity measures used for the analysis of time series data are D_2 and K_2. D_2 is often used as a discriminating measure for hypothesis testing to detect nontrivial structures in the time series. However, if the time series involves colored noise, a better discriminating measure is considered to be K_2 [11]. We employ surrogate analysis using both D_2 and K_2 as discriminating measures and to compute these measures, we make use of the automated algorithmic schemes proposed by us recently [9,10]. The scheme involves creation of an embedding space of dimension M with delay vectors x_j constructed from the time series. One then counts the relative number of data points in the embedded attractor within a distance R from a particular i^{th} data point

$$p_i(R) = \lim_{N_v \to \infty} \frac{1}{N_v} \sum_{j=1, j \neq i}^{N_v} H(R - |\boldsymbol{x_i} - \boldsymbol{x_j}|) \tag{1}$$

where N_v is the total number of reconstructed vectors and H is the Heaviside step function. Averaging this quantity over N_c number of randomly selected centres gives the correlation sum

$$C_M(R) = \frac{1}{N_c} \sum_{i}^{N_c} p_i(R) \tag{2}$$

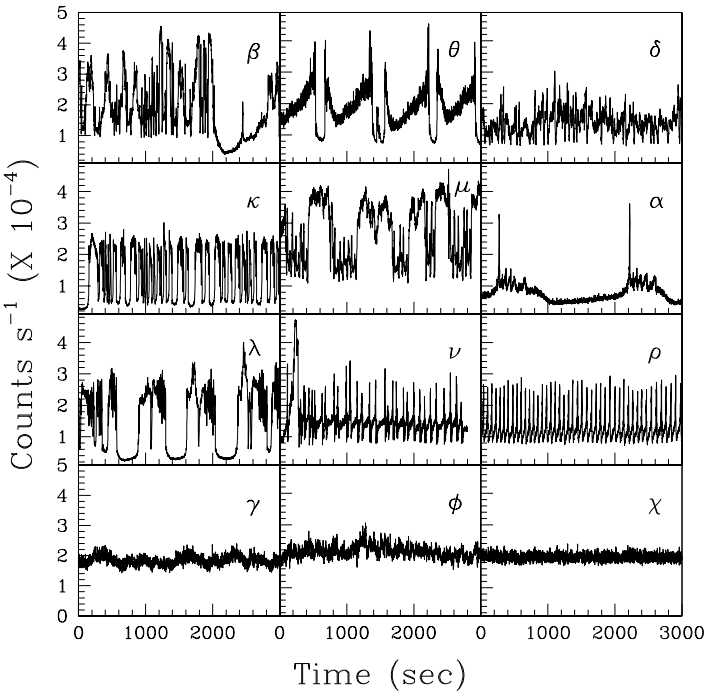

Fig. 1. Light curves from the 12 temporal states of the black hole system GRS 1915+105. Only a part of the generated light curve is shown for clarity.

The correlation dimension $D_2(M)$ is then defined to be,

$$D_2 \equiv \lim_{R\to 0} d(logC_M(R))/d(log(R)) \tag{3}$$

which is the scaling index of the variation of $C_M(R)$ with R as $R \to 0$. In our scheme, D_2 is computed by choosing a scaling region algorithmically.

To compute K_2, one measures the ratio at which the trajectory segments are increased as M increases, using the formal expression

$$K_2\Delta t \equiv \lim_{R\to 0} \lim_{M\to\infty} \lim_{N\to\infty} log(C_M(R)/C_{M+1}(R)) \tag{4}$$

To generate the surrogate data sets, we apply the IAAFT scheme [12,13] using the TISEAN package [8]. Finally, in order to visualise the qualitative features of the underlying attractor, we use the singular value decomposition (SVD) analysis (for details, see [10]). The SVD analysis computes the dominant eigen vectors whose projection, called the BK projection, shows the reconstructed attractors from the time series. Here we use the TISEAN package to generate the SVD plots.

The black hole source under investigation in this work, GRS 1915+105, is unique among all such sources in that it shows a wide range of variability in the light curves. Belloni et al. [14] have classified the light curves into

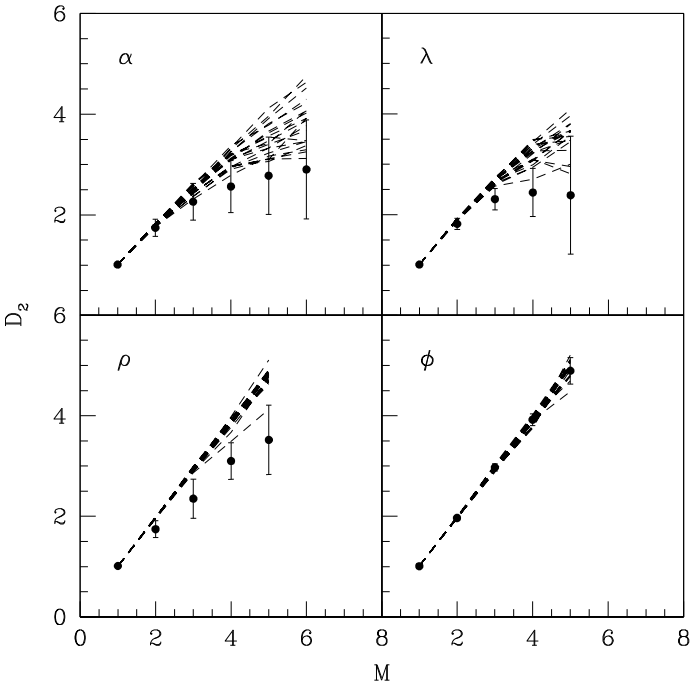

Fig. 2. Surrogate analysis with D_2 as a discriminating measure for the light curves from four states of GRS 1915+105. Surrogates are represented by dashed lines without error bar. Here we have done surrogate analysis with 10 surrogates. For more detailed surrogate analysis with 20 surrogates, see [1]. Note that the null hypothesis can be rejected in all cases except the ϕ state.

12 spectroscopic classes based on the RXTE observations. The nature of the light curves changes completely as the system flips from one temporal state to another. We have chosen a representative data set from each temporal class and extracted continuous data streams 3200 seconds long from it. The light curves were generated with a time resolution of 0.5 seconds resulting in approximately 7000 continuous data points for each class. More details regarding the data are given elsewhere [15].

Fig.1 shows all the 12 light curves used for the analysis, which are labelled by 12 different symbols representing the 12 temporal states of the black hole system. An earlier analysis of these light curves has shown that more than half of these 12 states deviated from a purely stochastic behavior [16]. Here we combine the results of D_2, K_2 and SVD analysis to get a better understanding regarding the nature of these light curves.

Fig.2 shows the results of surrogate analysis on four of the 12 states. It is clear that, of the states shown in the figure, only ϕ shows purely stochastic behavior. Of the remaining 8 states not shown, three more, namely γ, δ and χ, are found to belong to this category. Thus, only four out of the 12 states show behavior consistent with white noise in the D_2 analysis.

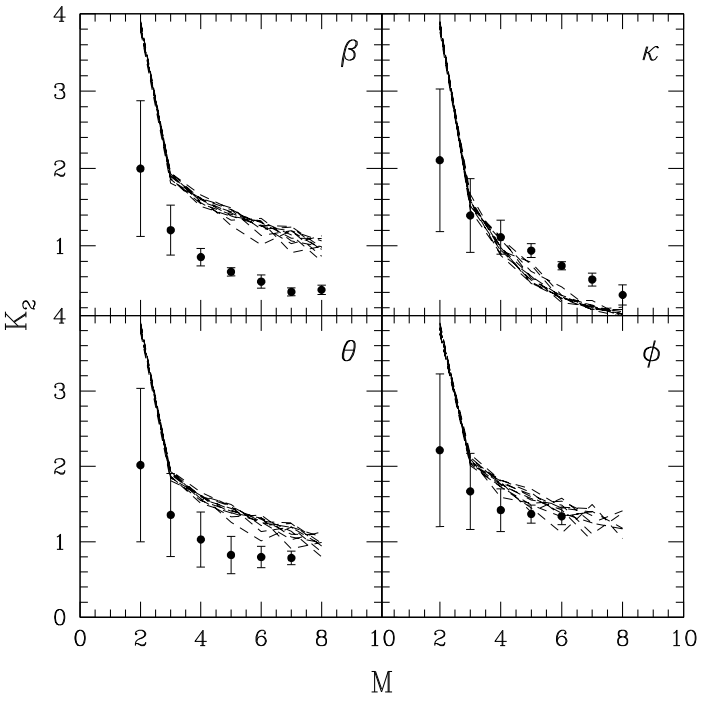

Fig. 3. Surrogate analysis of the light curves from four states with K_2 as the discriminating measure. While the data and the surrogates can be distinguished for β and θ, κ and ϕ behaves like colored noise and white noise respectively.

It is known that the X-ray emissions from the accretion discs may also involve colored noise. The colored noise gives a saturated value of D_2 and hence it is difficult to identify it in D_2 analysis. For this, we undertake surrogate analysis with K_2 as discriminating statistic. While data involving nontrivial structures give a saturated value of K_2, for pure colored noise, $K_2 \to 0$ as the embedding dimension M is increased. Results of K_2 analysis for four representative states are shown in Fig.3. While the behavior of β, θ and ϕ are consistent with earlier D_2 analysis, the bahavior of κ suggests that it is contaminated with colored noise. In fact 3 of the 8 states - κ, λ and μ - which showed deviation from stochastic behavior in the D_2 analysis are found to be contaminated with colored noise in the K_2 analysis. For more details regarding D_2 and K_2 analysis, see [1].

Finally, we perform a SVD analysis on all the states which clearly shows the qualitative nature of the underlying attractors. The plot of attractors for selected states is shown in Fig.4. The most interesting plot is for the ρ state which shows a typical limit cycle type attractor added with noise. Also, note that the SVD plot for the κ state has nontrivial appearance, eventhough the surrogate analysis suggested the presence of colored noise. This may be an indication that the state is not a pure colored noise. The same behavior is

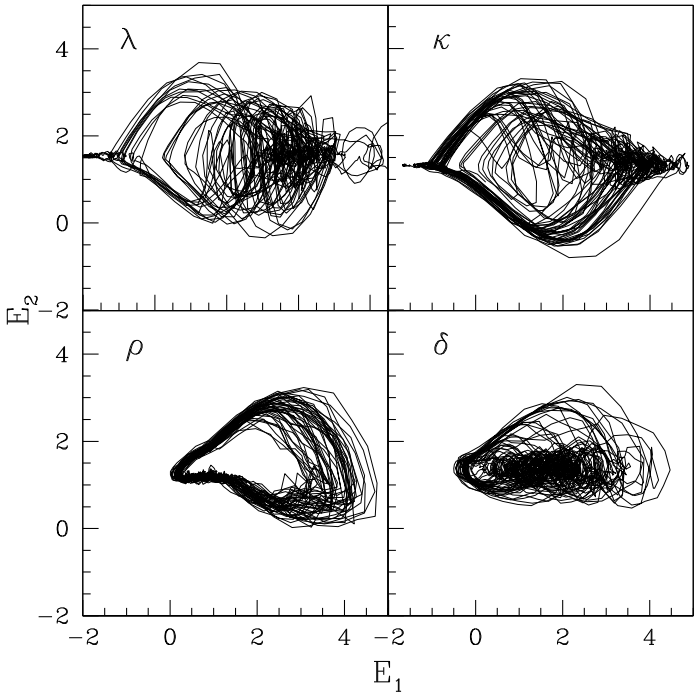

Fig. 4. The plot of attractors underlying four states of the black hole system reconstructed via SVD analysis. Except the ϕ state, which behaves as a white noise, all the others indicate the presence of underlying attractors, the most interesting being the ρ state.

found for two other states, λ and μ. Thus, these 3 states are likely to be a mixture of deterministic nonlinearity and colored noise.

Based on our results, the 12 states can thus be divided into 3 broader classes from the point of view of their temporal properties. It turns out that some of the states which are spectroscopically different, behave identically in their nonlinear dynamics characteristics. This may be an indication of of some common features in the mechanism of production of light curves from these states.

3 Conclusion

Identifying nontrivial structures in real world systems is considered to be a challenging task as it requires a succession of tests using various quantitative measures. Eventhough a large number of potential systems from various fields have been analysed so far, the results remain inconclusive in most cases. Here we present an interesting example of an astrophysical system, which we analyse using several important quantifiers of nonlinear dynamics. We find that out of the 12 spectroscopic states of the black hole system, only 4 are purely stochastic. The remaining states show signatures of deterministic nonlinearity, with 3

of them contaminated by colored noise. All these 8 states are found to have $D_2 < 4$ so that their complex temporal behavior can be approximated by 3 or 4 coupled ordinary differential equations. Based on our results, the 12 states can be broadly classified into 3 from a dynamical perspective: purely stochastic with $D_2 \to \infty$, affected by colored noise and those which show deterministic nonlinear behavior with $D_2 < 4$.

KPH and RM acknowledge the financial support from Department of Science and Technology, Govt. of India, through a research grant No. SR/SP/HEP-11/2008.

References

1.K. P. Harikrishnan, R. Misra and G. Ambika. Nonlinear Time Series Analysis of the Light Curves from the Black Hole System GRS 1915+105. *Research in Astron. & Astrophys.*, 11:71, 2011.
2.R. C. Hilborn. *Chaos and Nonlinear Dynamics*, New York, 1994, Oxford University Press.
3.M. Lakshmanan and S. Rajasekhar. *Nonlinear Dynamics*, New York, 2003, Springer.
4.J. R. Buchler and Z. Kollath. Strange Cepheids and RR Lyrae. *Astrophys. J.*, 555:961, 2001.
5.N. Jevtic, J. S. Schweitzer and C. J. Cellucci. Nonlinear time series analysis of northern southern hemisphere daily sunsspot numbers in search of short term chaotic behavior. *Astronomy and Astrophys.*, 379:611, 2001.
6.M. Gliozzi, C. Rath, I. E. Papadakis and P. Reig. Characterising black hole variability with nonlinear methods: the case of X-ray Nova 4U 1543-47. *Astronomy and Astrophys.*, 512:21, 2010.
7.H. Kantz and T. Screiber. *Nonlinear Time Series Analysis*, Cambridge, 1997, Cambridge University Press.
8.R. Hegger, H. Kantz and T. Schreiber. Practical implementation of nonlinear time series methods: The TISEAN package. *Chaos*, 9:413, 1999.
9.K. P. Harikrishnan, R. Misra, G. Ambika and A. K. Kembhavi. A non subjective approach to the GP algorithm for analysing noisy time series. *Physica D*, 215:137, 2006.
10.K. P. Harikrishnan, R. Misra and G. Ambika. Combined use of correlation dimension and entropy as discriminating measures for time series analysis. *Comm. Nonlinear Sci. Num. Simulations*, 14:3608, 2009.
11.M. B. Kennel and R. Isabelle. A method to distinguish possible chaos from colored noise and to determine embedding parameters. *Phys. Rev. A*, 46:3111, 1992.
12.T. Schreiber and A Schmitz. Improved surrogate data for nonlinearity tests. *Phys. Rev. Lett.*, 77:635, 1996.
13.T. Schreiber and A. Schmitz. Surrogate time series. *Physica D*, 142:346, 2000.
14.T. Belloni, M. Klein-Wolt, M. Mendez, M. van der Klis and van Paradjis. A model independent analysis of the variability of GRS 1915+105. *Astronomy and Astrophys.*, 355:271, 2000.
15.R. Misra, K. P. Harikrishnan, B. Mukhopadhyay, G. Ambika and A. K. Kembhavi. The chaotic behavior of the black hole system GRS 1915+105. *Astrophys. J*, 609:313, 2004.
16.R. Misra, K. P. Harikrishnan, G. Ambika and A. K. Kembhavi. The nonlinear behavior of the black hole system GRS 1915+105. *Astrophys. J*, 643:1114, 2006.

Chaotic Modeling and Simulation (CMSIM) 3: 485-498, 2012

Single-partial Model of the Nonlinear Resonant Medium

Leonid A. Rassvetalov [1]

[1] Yaroslav the Wise Novgorod State University, Veliky Novgorod, Russia
(E-mail: leonid.rassvetalov@novsu.ru)

Abstract: Responses of the nonlinear resonant medium represented by set oscillators with various types of nonlinearity are investigated. Solutions of the nonlinear equations of oscillator in the form of final Volterra series in the time and frequency domains, corresponding to anharmonicity are received. Integral transformation of input signals responses' character is displayed. Both the duality of mediums under consideration as well as classical nonlinear circuits and the opportunity of realization of signals real time processing in those mediums attention is paid to.

Keyword: oscillator, resonance medium, Volterra series, nonlinearity, dualism, signal processing.

1 Introduction

Due to the time-frequency dualism nonlinear resonant (NRM) medium makes possible to calculate integral transformations of the convolution type in frequency space with the same connectivity as multiplication in time space.
In this case nonlinear effects will lead not to frequency mixing resulting in generation of oscillations with combinational frequencies, but to time mixing, i.e. to generation of signals (pulses) at combinational instants of time [1, 3]. This time-frequency dualism phenomenon is illustrated by fig. 1.

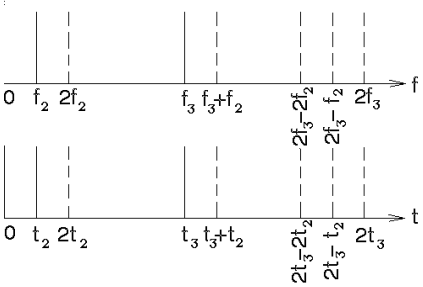

Fig. 1. Responses of nonlinear systems to multisignal excitation: above – responses of the nonlinear circuit to a series of harmonic excitations, below – responses of the nonlinear resonant medium to the excitation in the form of delta functions.

The time positions of responses are as rigidly connected to the time position of excitation pulses in nonlinear frequency space as combinational frequencies arising in a nonlinear circuit are connected to the excitation frequencies.

Received: 18 July 2011 / Accepted 30 March 2012

ISSN 2241-0503

Let us define the resonant medium as a set of high-Q oscillators, resonating in a frequency band. Such representation depicts the medium's local heterogeneity. The term "oscillator" here covers such concepts as separate micro particles or medium collective excitations – quasi-particles – under quantum-mechanical consideration, and as molecules or even the macroscopical particles carrying all properties of the substance - at the classical approach. In such a model the nonlinear properties of the medium can be provided both by the interaction of external excitation with a separate oscillator, and by the interaction between separate excited oscillators and thus reduced to the following types

- Anharmonicity;
- Nonlinear excitation;
- Nonlinear attenuation;
- Nonlinear interaction between oscillators.

In the latter case it is required to resolve a problem of many particles for the description of the model while solving one-partial problem is sufficient for the first three kinds of nonlinearity. The medium's response to the external excitation will be calculated by summing the responses of separate oscillators regarding with respect to their frequency distribution density $g(\omega)$. It is appropriate to mention here that the resonant medium represented by a set of oscillators is a real frequency space and it is convenient to describe it in terms of frequency representation.

The response of such nonlinear resonant medium - echo - signal – is a result of in-phase summation of oscillations of the excited oscillators, therefore the term «phased echo» is frequently used for this signal definition.

Specific physical and mathematical models distinguished by both the wide variety, and significant complexity are used in various type echo researches. In the applied perspective the theory of a spin echo [2] is most elaborated, still in this field the analysis is limited to small-signal approximation. The statistical analysis of the known physical and mathematical models of echo phenomenon in various media, not limited by the small-signal approximation framework, represents significant mathematical difficulties. The volume of such calculations even more increases due to the wide variety of specific physical mechanisms of echo – signals formation.

The purpose of the given article is to elaborate a unified description of the echo phenomenon regardless of the specific physical mechanism of its formation, suitable for the analysis of EP operation constituting a part of various radio engineering systems affected by signals and interference of any intensity. The mechanisms of nonlinearity mentioned above have the peculiarities related to responses' amplitude behavior and responses' phase - exciting pulses' phase dependence. The dependence of responses' shape on the shape of excitation pulses is the same for all types of nonlinearity. Therefore one kind of nonlinearity, that is anharmonicity, is considered in the given article.

2 NRM model with anharmonic oscillators.

Let us present the equation of the i-th anharmonic oscillator as follows

$$D_i y_i(t) + F_i[y_i(t)] = x(t), \quad (1)$$

where $x(t)$ - external excitation, $D_i = \frac{d^2}{dt^2} + 2\sigma_i \frac{d}{dt} + \omega_{0i}^2$ - linear operator, σ_i and ω_{0i} - loss characteristic and resonant frequency of linear approximation, correspondingly, $y_i(t)$ – response of the i-th oscillator, $F\left[y(t)\right] = \sum_{k=2}^{p} a_k y^k(t)$ is a polynomial of the p-th degree, a_k - the constants including power constants and geometrical values. Later, due to the equity of all oscillators the index i will be omitted. To solve (1) let us pass to the integral relation (2)

$$y(t) = \int_{t_0}^{T} h(\tau) x(t-\tau) d\tau - \int_{t_0}^{T} h(\tau) F\left[y(t-\tau)\right] d\tau \quad (2)$$

where $h(\tau) = \int_0^{\infty} \left[F\{y\}\right]^{-1} e^{j\omega t} \frac{d\omega}{2\pi}$ - (3)

pulse function of the linear part of (1), $[F\ \{\cdot\}]^{-1}$ – inverse Fourier transform. Substituting specific operator D in (3) we will have

$$h(\tau) = \begin{cases} \frac{1}{\omega_0} e^{-\sigma\tau} \sin \omega_e \tau, & \tau > 0, \\ 0, & \tau \le 0, \end{cases} \quad (4)$$

where $\omega_e = \sqrt{\omega_0^2 - \sigma^2} \approx \omega_0$.

The solution of (2) will be found by the iterative method that results in the representation of $y(t)$ in the form of Volterra finite series in case of weak nonlinearity ($a_k << 1$, $k = 2, 3, \ldots, p$):

$$y(t) = h_p + \sum_{p=1}^{n} \int_{E^p} h_p(\tau_1, \ldots, \tau_p) \prod_{i=1}^{p} x(t-\tau_i) d\tau_i, \quad (5)$$

where E^p - *p-dimensional* Euclidean space, in which Volterra kernels h_p (τ_1, τ_2, …, τ_p), representing pulse functions of nonlinear transformation of the p-th order are determined. So, for example,

$$h_2(\tau_1, \tau_2) = \begin{cases} \int_{-\infty}^{\infty} h(\tau) h(\tau_1 - \tau) h(\tau_2 - \tau) d\tau, & \tau_1,\ \tau_2 \ge 0, \\ 0 \quad \text{for all other values } \tau. \end{cases}$$

Outside the framework of the simple model of the isotropic medium without space nonlocal coupling considered above, $y(t)$ and $x(t-t_i)$ in (4)

should be vectors, and $h_p(\tau_1,\ldots,\tau_p)$ – tensor of the p + 1-th rank, having such values as charges, masses, geometrical and power constants, as well as values characterizing dissipation of energy as constants. This more general case which doesn't lead to any change of the final conclusions is not considered here. However, transition to this case is quite obvious.

Find the explicit form of the third order Volterra kernel

$$h_3(\tau_1,\tau_2,\tau_3)=\int_{E^1} h(\tau)h(\tau_1-\tau)h(\tau_2-\tau)h(\tau_3-\tau)d\tau$$

The area of integration corresponding to a causal kernel, is shown as shaded in fig. 2, according to which

$$h_3(\tau_1,\tau_2,\tau_3)=\int_0^{\min\{\tau_1,\tau_2,\tau_3\}} h(\tau)h(\tau_1-\tau)h(\tau_2-\tau)h(\tau_3-\tau)d\tau$$

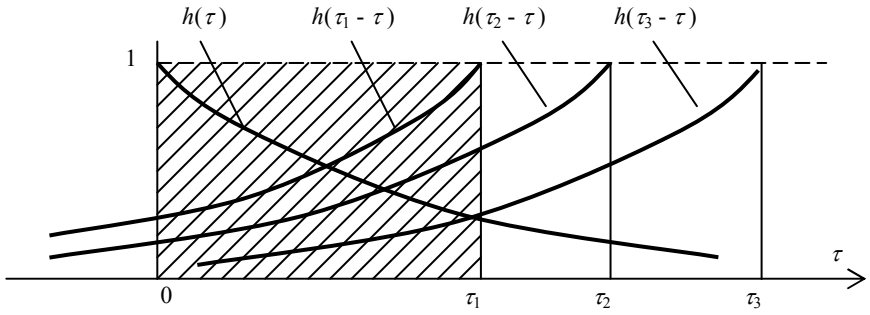

Fig. 2. The area of integration corresponding to a causal kernel.

Let $a = min\ \{\tau_1,\tau_2,\tau_3\}$. Taking (1.2.4) into account we have

$$h_3(\tau_1,\tau_2,\tau_3)=-\frac{1}{16\sigma\omega_e^4}e^{-\sigma(\tau_1+\tau_2+\tau_3)}\left(e^{2\sigma a}-1\right)\times$$

$$\left[\cos\omega_e(\tau_1-\tau_2-\tau_3)+\cos\omega_e(\tau_1+\tau_2-\tau_3)+\cos\omega_e(\tau_1-\tau_2+\tau_3)\right];$$

Under condition of $\omega_e >> \sigma$ the terms having the factor $1/16\omega_e^5$ are rejected here.

Thus:

if $\min\{\tau1,\tau2,\tau3\} = \tau1$ then

$$h_3(\tau_1,\tau_2,\tau_3)=\frac{1}{16\sigma\omega_e^4}\left[e^{-\sigma(\tau_1+\tau_2+\tau_3)}-e^{-\sigma(-\tau_1+\tau_2+\tau_3)}\right]\times \tag{6}$$

$$\left[\cos\omega_e(\tau_1-\tau_2-\tau_3)+\cos\omega_e(\tau_1+\tau_2-\tau_3)+\cos\omega_e(\tau_1-\tau_2+\tau_3)\right];$$

2) if $min\{\tau_1, \tau_2, \tau_3\} = \tau_3$ then

$$h_3(\tau_1,\tau_2,\tau_3) = \frac{1}{16\sigma\omega_e^4}\left[e^{-\sigma(\tau_1+\tau_2+\tau_3)} - e^{-\sigma(\tau_1+\tau_2-\tau_3)}\right]\times$$

$$\left[\cos\omega_e(\tau_1-\tau_2-\tau_3)+\cos\omega_e(\tau_1+\tau_2-\tau_3)+\cos\omega_e(\tau_1-\tau_2+\tau_3)\right];$$

3) if $min\{\tau_1, \tau_2, \tau_3\} = \tau_2$ then

$$h_3(\tau_1,\tau_2,\tau_3) = \frac{1}{16\sigma\omega_e^4}\left[e^{-\sigma(\tau_1+\tau_2+\tau_3)} - e^{-\sigma(\tau_1-\tau_2+\tau_3)}\right]\times$$

$$\left[\cos\omega_e(\tau_1-\tau_2-\tau_3)+\cos\omega_e(\tau_1+\tau_2-\tau_3)+\cos\omega_e(\tau_1-\tau_2+\tau_3)\right];$$

Another way to write the third order kernel is following below:

$$h_3(t,\tau_1,\tau_2,\tau_3) = \int_{\max\{\tau_1,\tau_2,\tau_3\}}^{t} h(t-\tau)h(t-\tau_1)h(t-\tau_2)h(t-\tau_3)d\tau =$$

$$\frac{1}{16\sigma\omega_e^4}\left[e^{-\sigma(3t-\tau_1-\tau_2-\tau_3)} - e^{-\sigma(t+\tau_1-\tau_2-\tau_3)}\right]\theta,$$

if $\tau_1 = \max\{\tau_1, \tau_2, \tau_3\}$;

$$h_3(t,\tau_1,\tau_2,\tau_3) = \frac{1}{16\sigma\omega_e^4}\left[e^{-\sigma(3t-\tau_1-\tau_2-\tau_3)} - e^{-\sigma(t-\tau_1+\tau_2-\tau_3)}\right]\theta,$$

if $\tau_2 = \max\{\tau_1, \tau_2, \tau_3\}$;

$$h_3(t,\tau_1,\tau_2,\tau_3) = \frac{1}{16\sigma\omega_e^4}\left[e^{-\sigma(3t-\tau_1-\tau_2-\tau_3)} - e^{-\sigma(t-\tau_1-\tau_2+\tau_3)}\right]\theta, \quad (7)$$

if $\tau_3 = \max\{\tau_1, \tau_2, \tau_3\}$;

Here $\theta = \cos\omega_e(t+\tau_1-\tau_2-\tau_3)+\cos\omega_e(t-\tau_1+\tau_2-\tau_3)+\cos\omega_e(t-\tau_1-\tau_2+\tau_3)$,

Find the oscillator respond to an excitation in the form of three δ-functions (fig. 3, at $t_1 = 0$):

$$x(t) = c_1\delta(t) + c_2\delta(t-t_2) + c_3\delta(t-t_3)$$

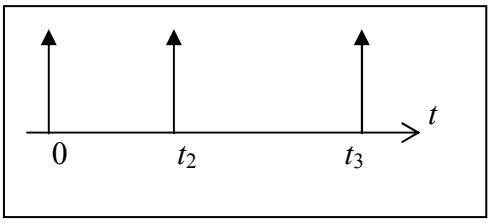

Fig. 3. Three-pulse excitation.

In the third approximation of the solution we have:

$$y_3(t) = \int_{E^1} h(t,\tau)x(\tau)d\tau - a_3\int_{E^3} h_3(t,\tau_1,\tau_2,\tau_3)\prod_{r=1}^{3} x(\tau_r)d\tau_r =$$

$$c_1h(t) + c_2h(t-t_2) + c_3h(t-t_3) -$$

$$c_1c_2c_3\{a_3\left[h_3(t,t_3,0,t_2) + h_3(t,t_3,t_2,0)\right]_{\tau_1=\max\{\tau_1,\tau_2,\tau_3\}} +$$

$$a_3\left[h_3(t,0,t_3,t_2) + h_3(t,t_3,t_2,0)\right]_{\tau_2=\max\{\tau_1,\tau_2,\tau_3\}} +$$

$$a_3\left[h_3(t,0,t_2,t_3) + h_3(t,t_2,0,t_3)\right]_{\tau_3=\max\{\tau_1,\tau_2,\tau_3\}}\} -$$

$$a_3c_1c_2^2[h_3(t,0,t_2,t_2)_{\tau_2,\tau_3=\max\{\tau_1,\tau_2,\tau_3\}} + h_3(t,t_2,0,t_2)_{\tau_1,\tau_3=\max\{\tau_1,\tau_2,\tau_3\}} +$$

$$h_3(t,t_2,t_2,0)_{\tau_1,\tau_2=\max\{\tau_1,\tau_2,\tau_3\}}] + \ldots$$

Here the first three terms correspond to the response of a linear circuit with the pulse characteristic *h (t)* and are not of interest from the echo – phenomena point of view. The expression in the first curly brackets defines the three-pulse response $y_3^{(123)}$, arising at the instant of time $t = t_2 + t_3$ (the top index corresponds to the numbers of stimulating pulses):

$$y_3^{(123)} = \frac{6a_3c_1c_2c_3}{16\sigma\omega_e^4}\left[e^{-\sigma(3t-t_2-t_3)} - e^{-\sigma(t-t_2+t_3)}\right]\cos\omega_e(t-t_2-t_3)$$

At the instant of time $t = t_2 + t_3$ all oscillators oscillate in the same phase and produce the pulse with the amplitude

$$y_3^{(123)}(t_2+t_3) = \frac{3}{8}a_3c_1c_2c_3e^{-2\sigma(t_3-t_2)}e^{-2\sigma t_2}\left(1-e^{-2\sigma t_2}\right)$$

The last terms in square brackets describe a two-pulse echo $y_3^{(12)}$ from the first two pulses:

$$y_3^{(12)}(t) = \frac{3a_3c_1c_2^2}{8\sigma\omega_e^4}\left[e^{-\sigma t} - e^{-\sigma(3t-2t_2)}\right]\cos\omega_e(t-2t_2)$$

There are two more echoes of two-pulse type from the second and third pulses $y_3^{(23)}(t)$ and from the first and third pulses $y_3^{(13)}(t)$

A distinctive feature of the echo - signals provided by anharmonicity is growth of the echo amplitude as the delay t_{12} between the first and the second pulses of excitation first rises up to maximum and then almost exponentially recesses [4], fig. 4.

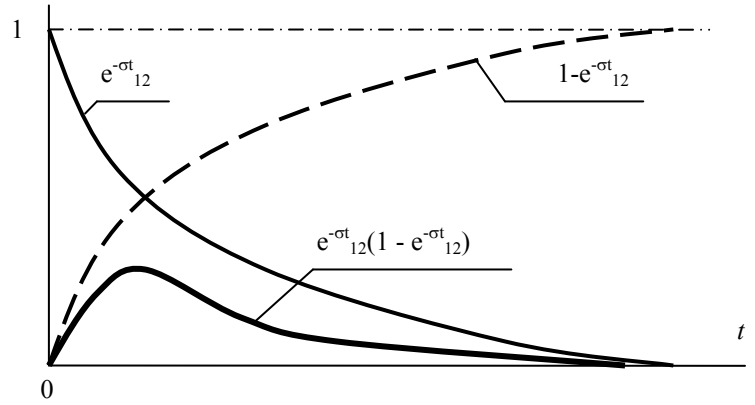

Fig. 4. Amplitude dependences of responses

Research the response of the anharmonic oscillator system to the excitation of three finite signals of the optional form within the framework of the third approximation.

The distinctive features associated with the record of the transformation kernel for various combinations of min $\{\tau_1,\tau_2,\tau_3\}$ and max $\{\tau_1,\tau_2,\tau_3\}$ will be shown in this calculation , as well as rules of calculating Volterra functionals stated.
The solution of the basic equation to a third approximation contains the first and third order functionals:

$$y_3(t) = \int_{E^1} h(t,\tau)x(\tau)d\tau - a_3 \int_{E^3} h_3(t,\tau_1,\tau_2,\tau_3)\prod_{r=1}^{3} x(\tau_r)d\tau_r \ , \quad (8)$$

among which only last one contains echo – responses .

As the all oscillators system response is of interest it should be specified that the solution (8) corresponds to the oscillator with the resonant frequency ω_e. Omitting a linear functional, we have:

$$y_3(t,\omega_e) = -a_3 \int_{E} h_3(t,\tau_1,\tau_2,\tau_3)\prod_{r=1}^{3} x(\tau_r)\,d\tau_r \ , \qquad (9)$$

The total system response in view of a frequency distribution density is as follows : $y_3(t) = \int_{-\infty}^{\infty} g(\omega)\, y_3(t,\omega_e)\, d\omega_e$

First find the three-pulse echo expression provided by the product of all three input pulses in (9). For this purpose we write of all terms resulting from the opening the brackets in the product

$$\prod_{r=1}^{3} x(\tau_r) = [x_1(\tau_1) + x_2(\tau_1 - \tau) + x_3(\tau_1 - T)][x_1(\tau_2) + x_2(\tau_2 - \tau) + x_3(\tau_2 - T)] \times$$
$$[x_1(\tau_3) + x_2(\tau_3 - \tau) + x_3(\tau_3 - T)],$$

those which are of interest for us

$$\prod_{r=1}^{3} x(\tau_r) = \ldots + x_1(\tau_1)x_2(\tau_1 - \tau)x_3(\tau_1 - T) + x_1(\tau_1)x_2(\tau_3 - \tau)x_3(\tau_2 - T) +$$
$$x_1(\tau_2)x_2(\tau_1 - \tau) + x_3(\tau_3 - T) + x_1(\tau_2)x_2(\tau_3 - \tau)x_3(\tau_1 - T) + \qquad (10)$$
$$x_1(\tau_3)x_2(\tau_1 - \tau)x_3(\tau_2 - T) + x_1(\tau_3)x_2(\tau_2 - \tau)x_3(\tau_1 - T) + \ldots$$

We notice that for the first term in (10) $\tau_3 = \max\{\tau_1,\tau_2,\tau_3\}$, and $\tau_1 = \min\{\tau_1,\tau_2,\tau_3\}$. Consequently, the kernel (7) should be used with the first term. In this kernel we should take that one of the three cosines in whose argument $\min\{\tau_1,\tau_2,\tau_3\}$ has a sign "plus", i.e. $\cos\omega(t+\tau_1-\tau_2-\tau_3)$. Thus, the transformation kernel for the first term (10) $x_1(\tau_1)x_2(\tau_2-\tau)x_3(\tau_3-\tau)$ is

$$h_3(t,\tau_1,\tau_2,\tau_3)\Big|_{\substack{\tau_3=\max(\tau_1,\tau_2,\tau_3)\\ \tau_1=\min(\tau_1,\tau_2,\tau_3)}} = \frac{1}{16\sigma\omega_e^4} \times \qquad (11)$$
$$\left[e^{-\sigma(3t-\tau_1-\tau_2-\tau_3)} - e^{-\sigma(t-\tau_1-\tau_2+\tau_3)}\right]\cos(t+\tau_1-\tau_2-\tau_3)$$

The other terms' kernels should be found in the same way. For example, in the fourth term $\tau_1 = \max\{\tau_1,\tau_2,\tau_3\}$, and $\tau_2 = \min\{\tau_1,\tau_2,\tau_3\}$. This term's kernel is

$$h_3(t,\tau_1,\tau_2,\tau_3)\Big|_{\substack{\tau_1=\max(\tau_1,\tau_2,\tau_3)\\ \tau_2=\min(\tau_1,\tau_2,\tau_3)}} = \frac{1}{16\sigma\omega_e^4} \times \qquad (12)$$
$$\left[e^{-\sigma(3t-\tau_1-\tau_2-\tau_3)} - e^{-\sigma(t+\tau_1-\tau_2-\tau_3)}\right]\cos(t-\tau_1+\tau_2-\tau_3)$$

As for the physical model under consideration Volterra kernels are symmetric the appropriate replacement of arguments in the terms (10) and in the corresponding kernels will reduce both all the terms and kernels to one. Indeed, the consequent change $\tau_1 \leftrightarrow \tau_3$, $\tau_2 \leftrightarrow \tau_1$ reduces the kernel (12) to the kernel (10). Such arguments replacement simultaneously reduces the fourth term to the first one.

Thus, the property of kernels symmetry appears to be rather useful and should be applied when possible in order to minimize rather bulky calculations of Volterra functionals.

All the terms in expression (10) are reduced to the same type, therefore (9) transforms in:

$$y_3(t,\omega) = -6a_3 \int_{E^3} h_3(t,\tau_1,\tau_2,\tau_3)\Big|_{\substack{\tau_3=\max(\tau_1,\tau_2,\tau_3)\\ \tau_1=\min(\tau_1,\tau_2,\tau_3)}} \times$$
$$x_1(\tau_1)x_2(\tau_2-\tau)x_3(\tau_3-T)d\tau_1 d\tau_2 d\tau_3$$

In this case it appears simpler to calculate all oscillators system response than that of one oscillator due to possibility of using spectral densities of the input signals:

$$y_3(t) = \mathrm{Re}\left\{ \begin{array}{l} -e^{-\sigma t}\int_{-\infty}^{\infty} cg(\omega_{\dot{y}})e^{j\omega t}\int_0^{t_1} e^{(\sigma+j\omega)\tau_1}x_1(\tau_1)d\tau_1 \times \\ \int_{\tau}^{\tau'} e^{(\sigma-j\omega)\tau_2}x_2(\tau_2)d\tau_2 e^{-2\sigma\text{å}} \times \\ \left[\int_T^{T'} e^{(\sigma-j\omega)\tau_3}x_3(\tau_3)d\tau_3 - \int_T^{T'} e^{(\sigma+j\omega)\tau_3}x_3(\tau_3)d\tau_3\right]d\omega_e \end{array} \right\}, \quad (13)$$

$$c = 6a_3 / 16\sigma\omega_e^4.$$

Internal integrals (13) represent spectral density of the input signals multiplied by the exponents exp ($\pm\sigma\tau_i$). Introducing definitions

$$S_{\pm\sigma i}(\omega_e) = \int_z^{z'} x_i(t)e^{\pm\sigma t}e^{-j\omega_e t}dt = \tilde{S}_{\pm\sigma i}(\omega_e)e^{\pm\sigma z}e^{-j\omega t},$$
$$,$$
$$S_{\pm\sigma i}(\omega_e) = \int_z^{z'} x_i(t)e^{\pm\sigma t}e^{j\omega_e t}dt = \tilde{S}^*_{\pm\sigma i}(\omega_e)e^{\pm\sigma z}e^{j\omega t}$$

where $\tilde{S}_{\pm\sigma i}(\omega_e)$ - spectral density of the signal $x_i(t)e^{\pm\sigma t}$ whose rise-up portion coincides with the time zero, we can write (13) as follows

$$y_3(t) = \mathrm{Re}\left\{\frac{3}{8}\frac{a_3}{\sigma}\int_{-\infty}^{\infty} g_1(\omega)\tilde{S}^*_{\sigma 1}(\omega)\tilde{S}_{\sigma 2}(\omega)\times\right.$$
$$\left.\left[\tilde{S}_{-\sigma 3}(\omega)e^{-\sigma T} - \tilde{S}_{\sigma 3}(\omega)e^{-\sigma(2t-T)}\right]e^{-\sigma(t-\tau)}e^{j\omega(t-T-\tau)}d\omega\right\},$$

where $g_1(\omega) = g(\omega)/\omega^4$.

As entrance signals duration is supposed to be negligible with reference to the decay time constant of the oscillators ($ti << 1/s$, $i = 1, 2, 3$), one can consider the approximate equality $\tilde{S}_{\sigma i} \approx \tilde{S}_{-\sigma i}$ valid. Then

$$y_3(t) = \mathrm{Re}\left\{\frac{3}{8}\frac{a_3}{\sigma} e^{-\sigma(t-\tau+\mathrm{T})}\left[1 - e^{-2\sigma(t-T)}\right]\times \right.$$
$$\left. \int_{-\infty}^{\infty} g_1(\omega)\widetilde{S}^*_{\sigma 1}(\omega)\widetilde{S}_{\sigma 2}(\omega)\widetilde{S}_{\sigma 3}(\omega) e^{j\omega(t-T-\tau)} d\omega \right\}. \qquad (14)$$

It follows from the last expression that the three-pulse echo signal form is defined by the product of spectral densities of the entrance signals, the spectrum of the first signal should be taken in a complex conjugated form. Composed of exponents factor at the integral sign determines the dependence of the three-pulse echo- signal amplitude on the entrance signals time positions. The echo - signal clusters about the moment of time $t = T + \tau$.

(14) can be written in the other form

$$y_3(t) = \frac{3}{8}\frac{a_3}{\sigma} e^{-\sigma(t-\tau+T)}\left[1 - e^{-2\sigma(t-T)}\right] g_1(t) * x_{\sigma 1}(t) \otimes x_{\sigma 2}(t-\tau) * x_{\sigma 3}(t-T),$$

where symbol * means convolution, and ⊗ - correlation.

Introducing multidimensional Fourier transforms of Volterra kernels instead of Volterra kernels themselves we can pass to the frequency representation for y(t)

$$K_n(\omega_1,...,\omega_n) = \int_0^{\infty}...\int_0^{\infty} h_n(\tau_1,...,\tau_n) e^{-j(\omega_1\tau_1+...+\omega_n\tau_n)} d\tau_1,...d\tau_n,, \qquad (15)$$

$$y(t) = \sum_{p=1}^{n} \frac{1}{2^p} \int_0^{\infty}...\int_0^{\infty} K_p(\omega_1,...,\omega_p) \prod_{k=1}^{p} S(\omega_k) e^{j\omega_0 t} d\omega_k, \qquad (16)$$

where $S(\omega)$ - spectral density of excitation $x(t)$ which use is determined by the assumed pulse character of $x(t)$. The reduced form of the record used in [5] is done in (16). In this record the total number of terms in the subintegral expression is equal to $(C_p^0 + C_p^1 + ... + C_p^p) = 2^p$, where C_p^k - number of combinations of p elements over k, containing k "minus" signs in the arguments of a gain. The first term in (16) describes signal $x(t)$ transmission through the linear quadripole with the gain $K_1(\omega)$, the others depict nonlinear signal transformation. The gain characteristics (16) are presented in [5].

If the frequencies in the gain arguments are not equal, i.e. $\omega_1 \neq \omega_2 \neq ... \neq \omega_p$, the ratio (16) describes occurrence of the new spectral components with frequencies $\pm\omega_1 \pm ... \pm \omega_k \pm ... \pm \omega_p$, passing through filters with the gain $K_p(\omega_1,..., \omega_k,..., \omega_p)$. Assuming the Q-quality of oscillators to be high it is possible to consider $K_p(\omega_1,..., \omega_k,..., \omega_p) = 0$ at $\omega_1 \neq ... \neq \omega_k \neq ... \neq \omega_p$. To exclude the highest harmonics of the signal the number of "plus" and "minus" signs in argument K_p should differ by unit. Such integrated transformation kernel in (16) is called a kernel with sum - differential argument in [5]. In this case

$$y(t) = \sum_{p=1}^{n} \frac{C_{2p-1}^{p-1}}{2^{2p-1}} \int_{-\infty}^{\infty} K_{2p-1}(\omega) S(\omega) \left|S(\omega)\right|^{2p-2} e^{j\omega t} d\omega + c.\tilde{n}., \qquad (17)$$

where *c.c.* - is a complex conjugate part of the expression presented above. The reduced form of the record is also applied here. Thus, for example, total description (17) of the second term of the series looks like this:

$$\frac{1}{2^3}\{\int_{-\infty}^{\infty} K_3(\omega,\omega,-\omega)S(\omega)S(\omega)S^*(\omega)d\omega +$$

$$\int_{-\infty}^{\infty} K_3(\omega,-\omega,\omega)S(\omega)S^*(\omega)S(\omega)d\omega +$$

$$\int_{-\infty}^{\infty} K_3(-\omega,\omega,\omega)S^*(\omega)S(\omega)S(\omega)d\omega + \text{ c.c.}\}$$

The block diagram of the device providing transformation (17) with all oscillators taken into account is shown in fig. 5. Filters $\Phi_i(\omega)$, i = 1, 2, …, m, m=N, select spectral bands of a signal with a bandwidth $\Delta\omega_i$; output oscillations of these filters are subject to instantaneous nonlinear transformation in nonlinear blocks with instantaneous characteristics $a_{2k-1}\xi^{2k-1}$, $k=1,2,...,n$, linear filters $K_{2k-1}^{(i)}(\omega)$ select the first spectral bands of the transformed oscillations, adders make linear summation of all output oscillations.

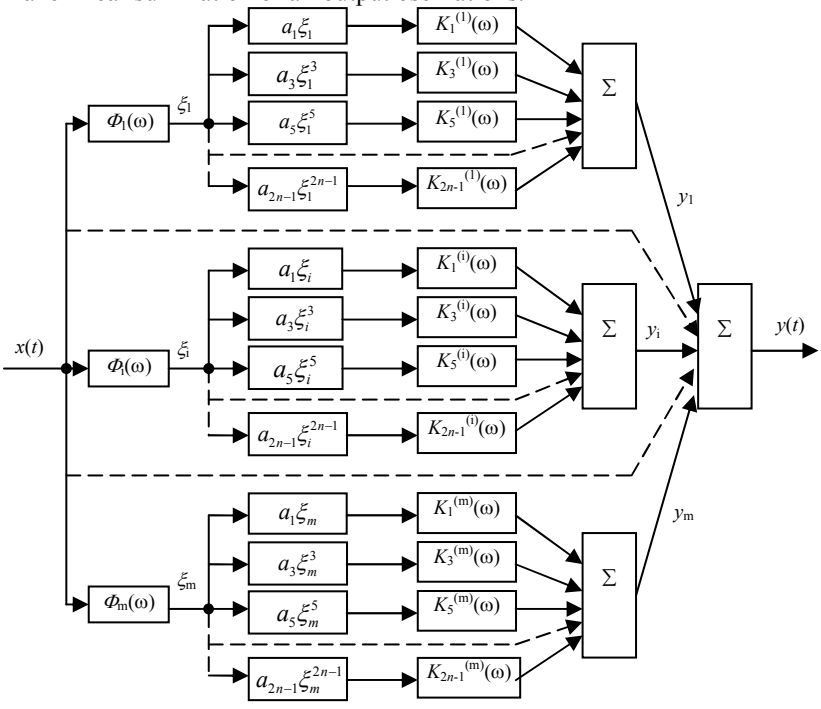

Fig. 5. The block diagram of the device making transformation (17).

The minimal order of nonlinearity in the equation (1) providing echo phenomena equals to three. This is the cubic medium and it can be represented by the radio engineering equivalent shown in Fig. 6. Putting aside thin distinctions of higher order echo time relations we can substantially simplify the block diagram transforming it as shown in Fig. 7.

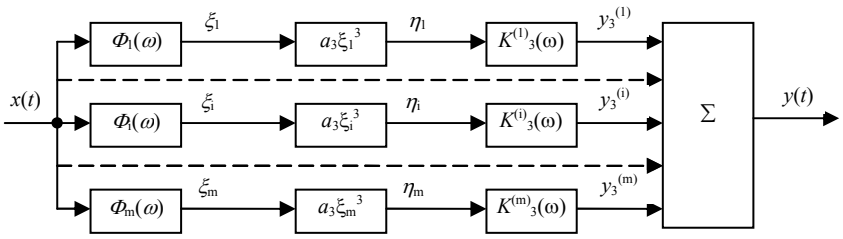

Fig. 6

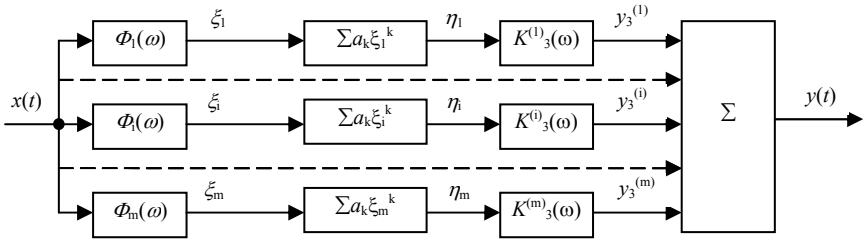

Fig. 7

We find the explicit form of the third order gain $K_3(-\omega,\omega,\omega)$ using the appropriate Volterra functional kernel (6):

$$h_3(t,\tau_1,\tau_2,\tau_3) = c\left[e^{-\sigma(\tau_1+\tau_2+\tau_3)} - e^{-\sigma(-\tau_1+\tau_2+\tau_3)}\right]\cos(\tau_1-\tau_2-\tau_3),$$

$$\tau_1 = \min\{\tau_1,\tau_2,\tau_3\}, \tau_2 = \max\{\tau_1,\tau_2,\tau_3\}$$

Then, letting $\omega_0 = \omega_e$,

$$\dot{K}_3(-\omega,\omega,\omega) = \int_0^{\infty} d\tau_3 \int_0^{\tau_3} d\tau_2 \int_0^{\tau_2} d\tau_1 h_3(\tau_1,\tau_2,\tau_3) e^{-j\omega(-\tau_1+\tau_2+\tau_3)} =$$

$$= \dot{F}(\omega-\omega_0) + \dot{F}(\omega+\omega_0) =$$

$$= \frac{1}{\left[\sigma+j(\omega-\omega_0)\right]^2}\left\{1+\frac{1}{2}\left[\frac{1}{\sigma-j(\omega-\omega_0)}+\frac{1}{\sigma+j(\omega-\omega_0)}\right]\right\} + \dot{F}(\omega+\omega_0).$$

Considering only positive frequencies domain and taking into account, that $\sigma >> 1$, we write $K_3(-\omega,\omega,\omega)$ in the following form

$$K_3(-\omega,\omega,\omega)\approx\frac{1}{\left[\sigma+j(\omega-\omega_0)\right]^2}\left\{1+\frac{1}{2}\left[\frac{1}{\sigma+j(\omega-\omega_0)}+\frac{1}{\sigma-j(\omega-\omega_0)}\right]\right\}$$

Correction resulted from the summation of the conjugated factors in the square brackets, has the maximal value (1 + 1/s) at $\omega - \omega_0 = 0$ and, thus,

$$K_3(-\omega,\omega,\omega)\approx\frac{1}{\left[\sigma+j(\omega-\omega_0)\right]^2},$$

as shown in fig. 7.

Let us find the whole oscillator system response to the signal $x(t)$:

$$y(t)=\frac{1}{2\pi}\sum_{p=1}^{n}a_{2p-1}\frac{C_{2p-1}^{p-1}}{2^{2p-1}}\int_E g'(j\omega)S(j\omega)\left|S(j\omega)\right|^{2p-2}e^{j\omega}d\omega+\text{ c.c.}, \qquad (18)$$

where $g'(j\omega)=g(\omega)\sum_i K_{2p-2}^{(i)}(j\omega)$ -

the total resonant characteristic of the oscillator system, function g(ω) has the meaning of the oscillator frequency distribution density. The first term of expression (18) describes linear transmission of the signal $x(t)$ through the filter with the gain $g'(j\omega)$; the second one corresponds to the nonlinear transformation of the third order and rather adequately characterizes the processes occurring in the nonlinear resonant medium:

$$y(t\mid p=2)=2\frac{3}{8}\frac{a_3}{2\pi}\operatorname{Re}\left\{\int_{-\infty}^{\infty}g'(j\omega)S(j\omega)\left|S(j\omega)\right|^2e^{j\omega t}d\omega\right\} \qquad (19)$$

The spectral density of the output signal corresponding to this transformation defines possible responses of medium.

In time domain the medium response to the excitation x (t), determined by the second approximation of the basic medium equation solution, can be presented according to (20) in the form, where $g'(t)$ - the pulse characteristic of the system with the gain $g'(j\omega)$.

$$S_y(j\omega\mid p=2)=\frac{3a_3}{8}\left[S(j\omega)\left|S(j\omega)\right|^2\right]g'(j\omega), \qquad (20)$$

The last expression determines functional capabilities of the devices which can use NRM properties, i.e. producing convolution, signal correlation function and Fourier transforms in real time.

References

1. Korpel A., Chatterjee M. Nonlinear echoes, phase conjugation, time reversal, and electronic holography. Proceedings IEEE, vol. 69, pp 1539 – 1556, 1981.

2. Hahn E.L. Physical Revue, vol. 80. pp. 580 – 594. 1950.
3. Rassvetalov L. A. Radiotechnika i Electronika, vol. 31. № 1, pp 8 – 14, 1987.
4. Gould R.W. American Journal Physic, vol. 37, 6. pp. 595 – 597, 1969.
5. Kashkin V. B. Functional polynoms in problems of a statistical radio engineering. Novosibirsk, Nauka, 1981, P. 145.

Chaotic Modeling and Simulation (CMSIM) 3: 499-507, 2012

Simulation and Control of Highly Maneuverable Aircraft under Turbulent Atmosphere using Nonlinear Dynamics Inversion Technique

Sunil Sharma[1], A.K.Ghosh[1]
[1]Indian Institute of Technology Kanpur, Kanpur-208016, India
Email-ID : sunilsharmaiitk@gmail.com

Nomenclature

V	Net Velocity of flight in body frame
V_z	Component of net velocity along body Z axis
α	Angle of attack
β	Sideslip angle
μ	Velocity vector roll angle
γ	Flight path angle
φ,θ,Ψ	Body axis Roll,Pitch,Yaw angle respectively (Euler angles)
$\Omega=[p,q,r]$	Body axis Roll,Pitch,Yaw rate respectively (Angular velocities)
$\delta_a,\delta_e,\delta_r$	Aileron,Elevator,Rudder deflection respectively
T	Thrust command

Abstract : This paper presents a robust technique to design the flight controllers for the aircraft to fly under turbulent atmosphere as well as to perform maneuvers incorporating the whole highly nonlinear dynamics of the aircraft system. Aircrafts have 6 degrees of freedom (DOF) and so translational as well as rotational motion can be performed by the aircrafts in all those directions of freedom. Aircraft flight controller is required for the aircraft to undergo various flight conditions and to perform various types of maneuvers in a desired and controlled manner. In this study, completely nonlinear set of equations defining whole dynamics of the aircraft have been used for simulation and Nonlinear Dynamics Inversion (NDI) control technique has been used to design the controller of the flight vehicle. NDI control technique is a highly emerging time domain control methodology used to design the controllers for various types of highly nonlinear systems.

Keywords : Nonlinear dynamics inversion (NDI), Aircraft flight controller, Flight envelope.

1. Introduction

In the field of aerospace vehicles, flight vehicle control law design methods have gained a lot of attention due to advancements in the theoretical concepts as

Received: 21 July 2011 / Accepted 30 March 2012

ISSN 2241-0503

well as exponential improvements in the hardware technologies over past decades. Any sort of flight vehicle designed i.e aircraft, rocket, missile is required to perform its intended task and along with that, it is an essential requirement for the vehicle to perform the task in a well controlled and desired manner. To implement that, there is requirement of a controller which would ensure that the desired task is done in a controlled manner, even if there is sudden turbulence caused by wind gusts.

It is extremely important that these vehicles undergo any of the flight condition in a controlled manner to avoid failure of missions and lethal accidents. Several attempts have been made to design the controllers for all sort of flight vehicles. There are a number of control techniques to design controllers for nonlinear dynamics systems like aircrafts. In this study, NDI technique is discussed and implemented to design the controller of an aircraft.

The advantage of preferring NDI control technique over other linear control methods is that the linear control methods linearize the nonlinear system about the equilibrium points to approximate it into a linear system and then design a control law; In this manner the approximated linearized equations can predict the actual system performance only in a very small flight envelope i.e. in a small range of operations and if the system goes beyond that range then these equations do not simulate the actual behavior of the system and so the linear controllers stay no more effective; whereas the NDI control technique does not linearize the system about any equilibrium point, rather it incorporates all the system nonlinearities while developing the control law and so NDI controllers stay quite efficient over a wide flight envelope.Thus NDI is a very efficient control technique to design controllers for the nonlinear systems.

In the field of control of aerospace vehicles, NDI control technique has gained a lot of attention and it has been applied to many of aircraft applications, such as F-16[1], F-18 HARV [2], F-117 [3] for designing the controller.

2. The Aircraft Model

The modeled aircraft used in this study is McDonnell Douglas F-4 which is a highly maneuverable fighter aircraft. An attempt has been made to control the various flight conditions of the aircraft using NDI. The aircraft 6 DOF equations of motion are given by the following set of differential equations which explain the translational and rotational dynamics of the aircraft model [4,5].

$$\dot{V} = (f_x \cos\alpha \cos\beta + f_y \sin\beta + f_z \sin\alpha \cos\beta)/m$$

$$\dot{\alpha} = [(f_z \cos\alpha - f_x \sin\alpha)/(mV\cos\beta)] - p\cos\alpha \,\mathrm{Tan}\,\beta + q - r\sin\alpha \,\mathrm{Tan}\,\beta$$

$$\dot{\beta} = [(f_y \cos\beta - \sin\beta(f_x \cos\alpha + f_z \sin\alpha))/(mV)] + p\sin\alpha - r\cos\alpha$$

$$\dot{\Omega} = [I]^{-1}[M - \Omega * ([I]\Omega)]$$

$$\begin{bmatrix}\dot{\varphi}\\ \dot{\theta}\\ \dot{\psi}\end{bmatrix} = \begin{bmatrix}1 & Tan_\theta Sin_\varphi & Tan_\theta Cos_\varphi\\ 0 & Cos_\varphi & -Sin_\varphi\\ 0 & Sin_\varphi Sec_\theta & Cos_\varphi Sec_\theta\end{bmatrix}\begin{bmatrix}p\\ q\\ r\end{bmatrix}$$

$$\dot{\mu} = p_w + (q_w Sin\mu Tan\gamma) + (r_w Cos\mu Tan\gamma)$$

$$\dot{\gamma} = (q_w Cos\mu) - (r_w Sin\mu)$$

$$\begin{bmatrix}\dot{x}_e\\ \dot{y}_e\\ \dot{z}_e\end{bmatrix} = C_1(\varphi)C_2(\theta)C_3(\Psi)\begin{bmatrix}VCos_\alpha Cos_\beta\\ VSin_\beta\\ VSin_\alpha Cos_\beta\end{bmatrix}$$

$$p_w = (pCos\alpha + rSin\alpha)(Cos\beta + Tan\beta Sin\beta) + \left(\frac{f_x \sin\alpha - f_z \cos\alpha}{mV}\right)Tan\beta$$

$$Q_w = \left(\frac{f_x \sin\alpha - f_z \cos\alpha}{mV}\right)$$

$$r_w = [f_y \cos\beta - \sin\beta(f_x \cos\alpha + f_z \sin\alpha)]/(mV) \qquad \text{--Eq.Set (1)}$$

Here f_x, f_y, f_z represent the net forces along X,Y,Z axes of the aircraft. Matrix [I] represent the moment of inertia matrix and M consists of the rotational moments about X,Y,Z axes of the aircraft and x_e, y_e, z_e represent the spatial position of the aircraft with respect to the earth axis system. C_1, C_2, C_3 represent the transformation matrices about roll, pitch, yaw axis respectively.

3. NDI Control Law

In the implementation of NDI control law, the control commands are generated based upon the error signal generated from the desired state and current state values received from the sensors via feedback path. In the NDI technique, generally a robust 2-scale separation method is used which allows the order of the controller to be smaller [6,7]. The NDI law used in this study uses time scale separation between slow variables and fast variables and correspondingly generates the control commands. Any aircraft system can be represented by the following nonlinear vector form dynamics equation

$$\dot{x} = f(x) + g(x)u \qquad \text{--Eq.(2)}$$

x represents the vector representing state variables, $f(x)$ represent nonlinear state dynamic function and $g(x)$ represent the control distribution function. NDI

control law inverts the dynamics equation and then replaces the inherent rate of change of state variable by the desired rate of change of that variable to generate the required command which is fed to the system. Inverting eq. (2) we get

$$u = g(x)^{-1}[\dot{x} - f(x)] \quad \text{--Eq.(3)}$$

Applying NDI control logic, above equation is converted into a form as

$$u_d = g(x)^{-1}[\dot{x}_d - f(x)] \quad \text{--Eq.(4)}$$

where, $$\dot{x}_d = k(x_d - x) \quad \text{--Eq.(5)}$$

x_d in eq.(5) represents the vector consisting of the desired values of state variables and x represents the vector consisting of the measured values of corresponding state variables obtained via feedback path. k represents state gain matrix whose elements are the tuning parameters of the controller and u_d represents the vector consisting of the control commands generated i.e. elevator, aileron, rudder deflections and thrust command which are to be fed to the aircraft system as control input.

4. Applicaton of NDI under various flight conditions

The purpose of this study is to control the various parameters of the aircraft for different flight conditions like cruise flight, sideslip flight, cordinated turn, pull-up maneuver, velocity vector roll maneuver etc. Table 1 shows all the flight conditions studied in this paper and shows the corresponding variables to be controlled in each flight condition so that the flight vehicle performs in the desired manner. For each case, NDI control law is implemented on the concerned set of governing nonlinear equations of the aircraft system and control commands corresponding to the desired states are generated.

Table 1. Various flight conditions and corresponding control variables

Flight conditions	Control variables
Cruise flight	α,β,μ,γ
Steady sideslip flight	α,β,Ψ,γ
Coordinated turn	α,β,γ,$\dot{\Psi}$
Pull-up maneuver	p,q,r,V
Velocity vector roll maneuver	α,β,γ,$\dot{\mu}$

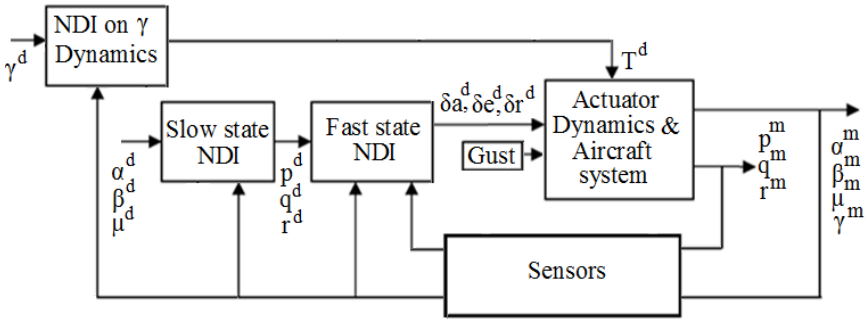

Figure 1. NDI control approach for control variables α,β,μ,γ

Figure 1 explains the implementation of NDI control law for the cases in which control variables are α,β,μ,γ.The desired states are represented by (α^d,β^d,μ^d, γ^d). Similarly other variables can be controlled in the similar fashion for other cases. In present case, (α,β,μ,γ) act as slow state variables whereas (p,q,r) act as fast state variables.NDI is applied on slow state variables as well as fast state variables as explained in equations (2)-(5) and control surfaces deflection commands (δ_a^d,δ_e^d,δ_r^d) are generated.

These command values are passed through the actuator dynamics system so as to ensure that the commands generated are well within the control surfaces deflection limits as well as within the maximum rate of deflection of control surfaces.Thrust command (T^d) is generated by applying NDI on γ dynamics equation in case of various flight conditions except pull-up and pull-down maneuvers as in these maneuvers, the thrust command is generated by applying NDI on dynamics equation of velocity.

5. Simulation, Control and Results

The 6 DOF equations of motion of the aircraft explain its translational and rotational dynamics.The equations were simulated using numerical method Runge-Kutta-4 (RK-4) algorithm. For simulation, completely nonlinear set of aerodynamic data of McDonnell Douglas F-4 aircraft has been used [8]. Results have been shown for different flight conditions.

Note : For all the following figures of results, the values of all the angles are in degree, distances are in meter, time is in second, angular velocities (p,q,r) are in radian/sec, velocities are in meter/sec and acceleration is in meter/sec^2.

Case 1. **Cruise flight control under effect of wind gusts:**

In this case, Cruise flight is controlled under turbulent atmosphere as sudden gust comes and aircraft trim condition is disturbed and the controller has to

control the aircraft and bring it back to the trim condition. As shown in figure 2, Aircraft is cruising at α= 4 deg and a sudden gust comes to disturb the trim condition of the aircraft and the controller acts to bring the aircraft back to the trim condition.

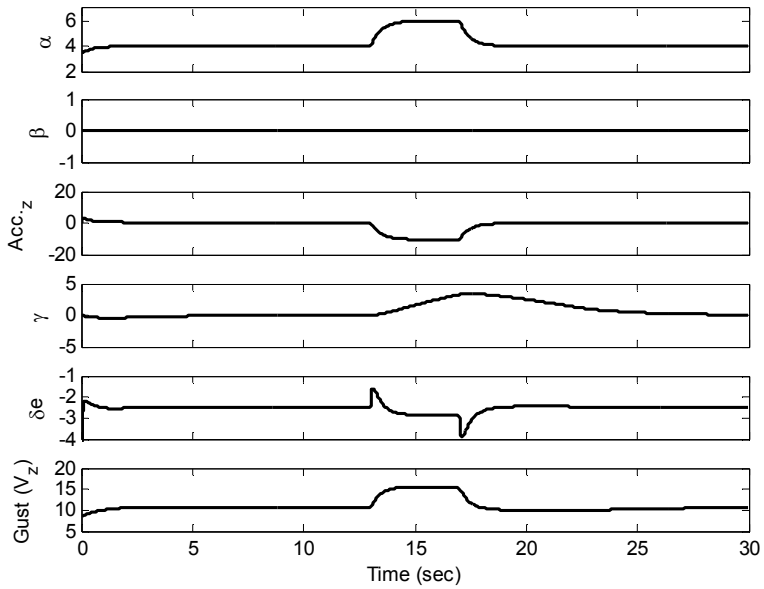

Figure 2. Cruise flight control under Turbulent Atmosphere

Case 2. **Steady sideslip flight under effect of wind gusts**

In this case, aircraft is undergoing steady sideslip flight and suddenly a vertical wind gust is introduced to disturb the aircraft states and the controller has to control and bring the aircraft states back to the desired values.

As shown in figure 3, aircraft is flying at α = 4 deg, β = 2 deg and the aircraft is holding Ψ= -2 deg for proper steady sideslip and then a sudden gust is introduced but the aircraft controller still performs in the desired manner.

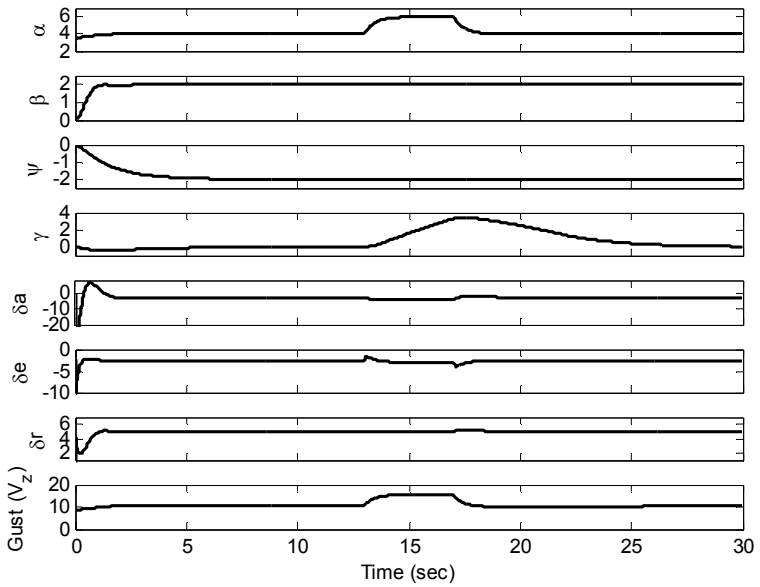

Figure 3. Steady sideslip flight control under Turbulent Atmosphere

Case 3. **Steady Coordinated turn**

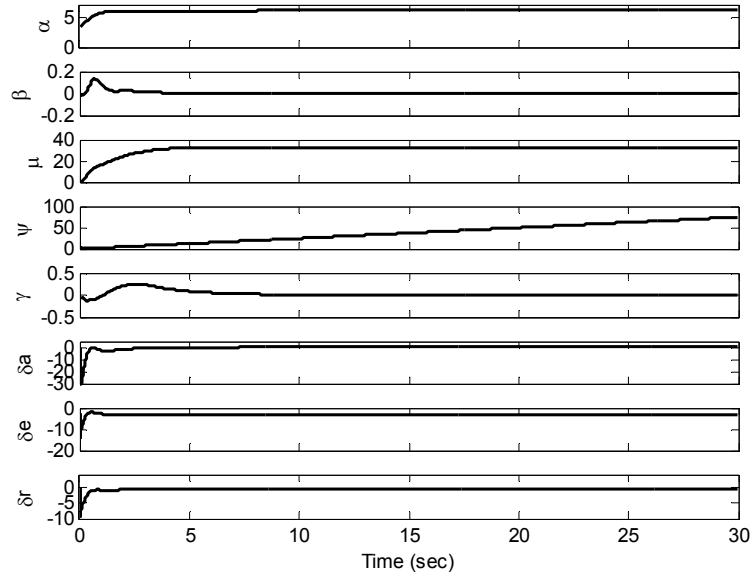

Figure 4. Aircraft states and control commands for Coordinated turn

In case 3, as explained by figure 4, the aircraft has to undergo steady coordinated turn i.e. the sideslip angle should be zero during the turn. In this case, aircraft is turning at the rate of change of Ψ as 2.5 deg/sec at α= 6 deg while maintaining sideslip to zero value.

Case 4. Pull-up Maneuver

In this case, aircraft performs a continuous pull-up maneuver in vertical XZ plane. In this case, maneuver is done at pitch rate of 0.1 rad/sec as shown by figure 5 which also shows that for vertical pull-up, the roll angle, roll rate, yaw rate should be zero.

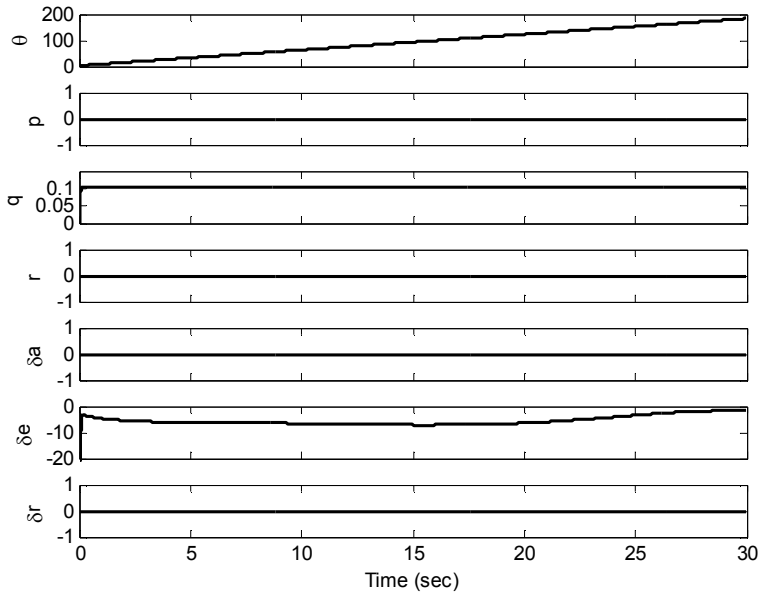

Figure 5. Aircraft states and control commands for Pull-up Maneuver

Figure 6 shows the aircraft trajectory in XZ plane during this flight condition.

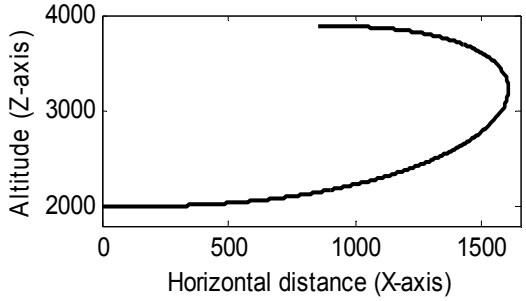

Figure 6. Aircraft trajectory in XZ plane during Pull-up Maneuver

Case 5. Velocity vector roll Maneuver

Aircraft performs a continuous roll maneuver about the velocity axis at high α. During this maneuver, aircraft should not lose altitude as well as should not go under sideslip motion. In this case, aircraft performs this maneuver at α=12 deg as shown in figure 7.

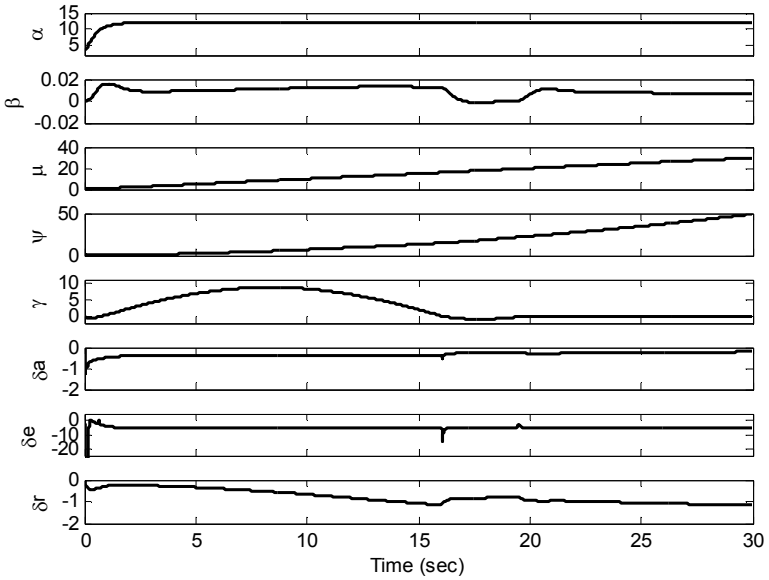

Figure 7. Velocity vector roll Maneuver at α =12 degree

References

1. Adams, R. J. ,Banda, S. S."Robust Flight Control Design Using Dynamic Inversion and Structured Singular Value Synthesis," IEEE Transactions on control systems technology,Vol.1,No. 2, NewYork,June 1993,pp 80-92.
2. Bugaski, D. J., Enns, D. F., and Elgersma, M. R., "A Dynamic Inversion Based Control with Application to the F-18 HARV," AIAA Paper 90-3407, Proceedings of the AIAA Guidance, Navigation, and Control Conference, Portland, OR, 1990, pp. 826-839.
3. Colgren, R., and Enns, D., "Dynamic Inversion Applied to the F-117A," AIAA Paper 97-3786, 1997.
4. Flight stability and automatic control,2nd edition,Robert C Nelson,Tata Mcgraw Hill.
5. Benjamin R. Carter, Time-optimization of high performance combat maneuvers-2005,Naval postgraduate school, Monterey,California.
6. S. A. Snell, D. F. Enns, and W. L. Garrard Jr., "Nonlinear Inversion Flight Control for a Supermaneuverable Aircraft," Journal of Guidance, Control, and Dynamics, Vol. 15, No. 4, AIAA, 1992, pp. 976-984.
7. J. Reiner, G.J. Balas, W.J. Garrard, Flight control design using robust dynamic inversion and time-scale separation, Automatica 32 (11) (1996)1493–1504.
8. A Collection of Nonlinear Aircraft Simulations in MATLAB, NASA/TM-2003-212145.

Chaotic Modeling and Simulation (CMSIM) 3: 509–517, 2012

The Chaotic Analysis of Financial Time Series: Classification of Foreign Exchange Rates Series via Their Exponential Divergence Curves

Pritha Das[1], Atin Das[2], and Gürsan Çoban[3]

[1] Bengal Engineering and Science University, Department of Mathematics,West Bengal, INDIA
(E-mail: pritha@math.becs.ac.in)
[2] NH School, Naktala, Calcutta, INDIA
(E-mail: dasatin@yahoo.co.in)
[3] Istanbul Technical University, Institute of Informatics, Division of Computational Science & Engineering, Istanbul, TURKEY
(E-mail: gursan.coban@be.itu.edu.tr)

Abstract. In this work we evaluate the notable results of four interrelated successive works ([2–5]) dealing with the classification properties and temporal evolution of foreign exchange rates series (ForEX). The main idea in these works can be conceptualized through the behavior of the exponential divergence curves of financial time series that make a clear distinction for both spatial (between countries) and temporal (between different time segments of ForEX series) patterns. Despite being a well known concept, the use of exponential divergence curves for the classification of ForEX series is a relatively new concept. The classification procedure discussed here is based on the surrogate testing procedure where the statistics gathered from the original system is compared to the ones that are gathered from a completely randomized system. Our new researches on the data during the period of present economic recession (January 2008-October 2009) by calculating the largest Lyapunov exponent (LLE) has shown that the earlier classification of countries based on LLE's holds true. By a similar approach, we have investigated the temporal evolution of the exponential divergence distance metrics where we have developed a computationally consistent procedure to obtain the metrics for various ForEX series. Finally we obtained strong indicators for the distinction of the temporal evolution of ForEX series for developed and developing countries. We discuss possible reasons for the existing separation of temporal structures.
Keywords: Lyapunov Exponents, surrogate test, randomness, fluctuation, nonlinear classification, foreign exchange rates.

1 Introduction

In 1966, Benoit Mandelbrot introduced the basic principle of a Martingale in finance theory as to describe the efficient market hypothesis (EMH). The idea

Received: 20 July 2011 / Accepted: 31 March 2012

ISSN 2241-0503

can be written as follows: the random process $z(t)$ is produced by a fair game if,

$$\langle z(t + \Delta t)\rangle_{\Phi} = z(t) \tag{1}$$

where the average is calculated via an information source Φ. Typically such an information may be evaluated through the historical observation of $z(t)$ as $\{z(t - \Delta t), z(t - 2\Delta t), \ldots\}$. If $z(t)$ is a martingale, then the historical observations are irrelevant in predicting the future prices, $\langle z(t + \Delta t)\rangle \approx z(t) + R$ for some return ratio R [1]. In this work, our approach towards financial series is different, such that historical observations of financial time series effects to the current conditions where nonlinear statistics obtained from the series follow distinguishably different patterns comparing to a random series. Assumptions of classical financial time series analysis about the source of local or global fluctuations strongly dissociate from the ones belonging to the nonlinear deterministic analysis. Hsieh [6] and Scheinkman [7] emphasize the two essential sources of the fluctuations that originate from the business cycles: (1) according to the Box-Jenkins formalism, the overall economy is stable however it is perturbed by permanent external shocks (such as whether, wars). In this case the fluctuating behavior of the system is a result of external effects. (2) In chaotic growth models, the system comes from a nonlinear dynamic one and has an intrinsic self-generating structure where the system is supposed to behave randomly. Although it is still possible to make short-term predictions, such effort is bounded by the information loss (kolmogorov entropy) due to the exponential divergence in phase space.

Few works investigate the similarity of nonlinear measures between original dynamics and surrogate data while measuring nonlinear similarity of time series. The independent works of Schreiber and Schmidtz [12] and Cellucci et al. [8] can be given as the two important contributions coming into prominence. The nonlinear similarity measures based on the exponential divergence of nearby trajectories was investigated by Cellucci et al. [8] where they have proposed an efficient procedure for estimating or to what extent a time series is noise corrupted. From their point of view the distance between exponential divergence curves ([13]) and the curves that were created from the phase-shuffled surrogates reduces while signal to noise ratio decreases. Originally they introduced the link between randomness and its effects on the statistics obtained from phase flow of the dynamics. If the the governing dynamics are known, then this effect may also be used to estimate the randomness of a time series [9]. One of the interpretation of this observation as verified by Schreiber and Schmidtz [12] is that the power of surrogate testing depends on the randomness level of the investigated time series. Thus, when the noise level of a time series is increased, then the nonlinear statistics gathered from the original series gets closer to the ones obtained from the surrogate ones.

Nonlinear phenomenon is widely discussed in financial studies due to its inevitable effects towards the evaluation of the nature of the considered system. When a system is governed by a deterministic law, the characteristics of the structure often show globally definable invariant measures such as fractal dimension and Lyapunov exponents as an extension of sensitive dependence to

initial conditions. In this work, we try to observe the behavior of separation between ForEX series depending on the Lyapunov exponents as the nonlinear statistics. The sections are arranged as follows: in Section 2 we give the brief results of the literature dealing with the existence of nonlinear dynamics in financial systems. In Section 3 we give the basic results of the nonlinear similarity tests including the crisis period. To analyze the temporal patterns, we also investigate the historical reactions of the ForEX system towards time depended random fluctuation under the assumption of a *stable nonlinear dynamic* structure. Our conclusions and future perspectives are given in Section 4.

2 Deterministic Flow of Exchange Rates

The first studies related to the determination of nonlinearity in financial time series approach the problem via statistical frameworks like BDS test for independence or bispectrum test for statistical nonlinearity. In spite of the difficulties in data quality concept, studies related to financial data have found evidence for nonlinear or chaotic relationships. Due to the importance of a key variable for macroeconomic policy, the exchange rates data have been researched widely in financial analysis. Through all these, results of the studies covering exchange rate dynamics are summarized by [10] as follows:

- The tests based on correlation dimension and some others confirmed nonlinear structure in exchage rates.
- Limited evidence for chaos.
- Residuals gathered from suitable statistical models (ARCH and GARCH) do not show nonlinear characteristics, so the mentioned models are adequate.

On the other hand studies that tries to quantify the geometrical peculiarities of phase flow assume a self-similar structure which is a result of sensitive dependence to initial conditions. For example Çoban and Büyüklü [3] analyzed the time series of New Turkish Lira with respect to US Dollars in between August 2001 and February 2007. The applied locally projective filtering methodology removed most of the noise contaminant which irregularly shadows the original phase flow (see Figure.(1)). The filtered series has a correlation dimension of $D_2 = 4.5$ and Lyapunov exponent of $\lambda = 0.05$. We state that, the phase flow properties of daily ForeX return series exhibit continuous flow characteristics rather than a discrete chaotic map or high dimensional random walk (Figure.(1)). Obviously, for such flow properties, the exponential divergence metrics has sense in terms of nonlinear dynamic analysis. Naturally, the surrogate testing procedure is able to show whether the nature of the governing dynamics of considered series has a significantly different behavior from a stochastic system.

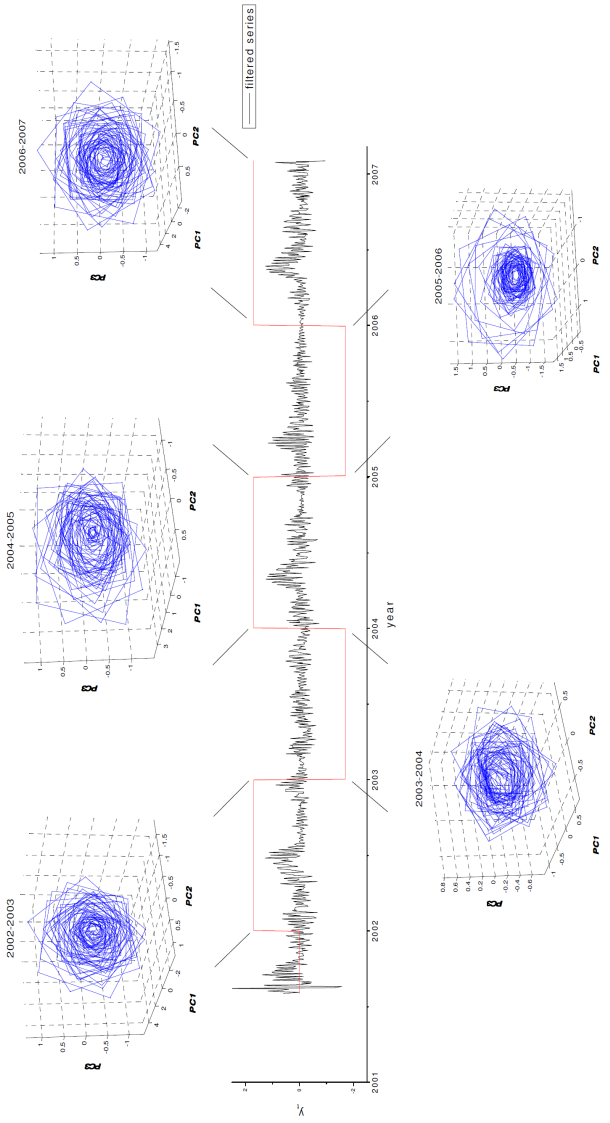

Fig. 1. The yearly phase flow representation of a highly noise reduced version of Turkish Lira-Dollar daily logarithmic return series in between 2001-2007. $PC_{1,2,3}$ stands for the first three principal directions used for projection.

3 Classification via Surrogate Testing

While working with real world observations generated by unknown dynamics some distributive properties should be acquired for the system to be analyzed. This may be realized by constructing random surrogate data sets that originate from the real observations. Surrogate data are designed to mimic constrained

properties of original data to allow a comparison between assumed dynamics and some other stochastic structure which have similar properties. The two basic versions for the surrogate data are produced via shuffling observations (Random Surrogate) in random order and randomization of complex phase parameter of 'Fast Fourier Transformed' series (FFT). Any random shuffle of the original data destructs all linear and nonlinear dependencies between the observations and preserves only the empirical distribution. Thus, the observations became completely independent by construction which could be evaluated as an extreme case among surrogate methods. In FFT procedure, all linear properties of original sequence remains constant since the power spectrum is preserved. Thus, comparing invariant properties are gathered from the original signal and FFT sequences by point of statistical assumptions under defined significance level yield an interpretation about nonlinearity ([14]).

What makes the exchange rate changes in the recession era much more complicated is the intervention from the respective governments during recession period, in addition to the news in fundamentals as detailed in [2]. Apart from usual complex rules governing the exchange rate, during the recession, most of the countries tried to resist it by direct interventions. Sometimes it could be change in policy or some times pumping huge amount of money into financial market or imposing restrictions on pay or interest rates, huge economic stimulus package etc. One can for example refer to Euro News for country-wise details (for both EU and non-EU countries) [11]. For the present purpose, we like to see if all these initiatives have effect on the exchange rate in the said time period.

Based on the surrogate analysis, the work of Das & Das [2] has shown that the direct distance of divergence curves between original and surrogate data series is a good qualitative parameter for clustering exchange rates series. Here and in the following, we use the term *distance to a surrogate* as a nonlinear *similarity measure* which is the distance between exponential divergence curves and their surrogate ones. The analysis in [2] have shown that ForEX series can be classified in three categories via their distances to surrogates:

- Group A: For some countries (India, China, Sri Lanka) the distance is too high.
- Group B: For some countries (Australia, Malaysia, Thailand) the distance is moderate.
- Group C: For some countries (Canada, Japan, Singapore, Sweden, Switzerland, UK) the distance is small.

It is also conjectured that the behavior of macroeconomic indicators (for example, the balance of trade) are highly related to the mentioned nonlinear similarity in between the clusters.

In line with the work [2], nonlinear data analysis of the data during which the economic recession had started. In that work, we considered daily data for twelve countries, over the span of nearly 36 years. Now we investigate data from the same 12 countries for the periods of January 2008 to October 2009, as the present recession had started around July 2008. We have again calculated

the largest Lyapunov exponent (LLE) and compared the LLE values calculated in previous work to the present values- that is LLE values previous and during recession.

During recession time, we find again that for countries whose LLE change is positive are China, India and Sri Lanka. They exactly correspond to earlier result of Group A. So we can say that countries with more the nonlinear structure in its ForExRate data, LLE change is positive. For other countries, we divide the change in two groups:

- When change is high- nearly -50% or more: Australia, Malaysia, Thailand and UK
- When change is moderate: Canada, Japan, Singapore, Sweden, Switzerland

Again, we see that the countries falling in group B (Except UK) has suffered high change. And finally, countries showing moderate change correspond to Group C. So, on the basis of change in LLE value during recession, we can conclude that the more nonlinear structure its foreign exchange rate shows the more its LLE changes.

3.1 Temporal Analysis of Surrogate Measures for ForEX Series

Do nonlinear similarity statistics exhibit a high frequency random scattering over long time intervals or they represent global fluctuations with wide wavelengths? In our simulations we show that the structure of the fluctuations of nonlinear statistics over long time intervals can be used to classify the ForEX series through their historical behavior. That means, for the last 3-4 decades financial time series have shown different evolutionary patterns. In this section our main aim is to give a consistent computational procedure depending on the concepts in [8] to obtain the conjunctural fluctuation of the distance to surrogate measures for various ForEX series. Here we use the term *conjunctural* since the basic consideration is on the observation of similarity variation for long time intervals (decades). For the simulations, we adopt the idea of Celluci et.al. [8] for our similarity measures. Here we will not explain the implementation of the algorithm in detail, instead we refer the reader to [5].

We start with the second formula of [8] defining the D statistics given in Equation.(2)

$$D = \frac{1}{N_k\, N_{surr}} \sum_{j=1}^{N_{surr}} \sum_{i=1}^{N_k} |\Lambda_{orig_j}(k_i) - \Lambda_{surr_j}(k_i)|. \tag{2}$$

where

$$\Lambda(k) = \frac{1}{N_{ref}} \sum_{n_0=1}^{N_{ref}} \log_2 \left(\frac{1}{|\mathcal{U}_\epsilon(\mathbf{s}_{n_0})|} \sum_{\mathbf{s}_n \in \mathcal{U}_\epsilon(\mathbf{s}_{n_0})} \frac{\|\mathbf{s}_{n_0+\delta k} - \mathbf{s}_{n+\delta k}\|}{\|\mathbf{s}_{n_0} - \mathbf{s}_n\|} \right) \tag{3}$$

In Equation.(3), $\|\cdot\| = \|\cdot\|_{L_2}$ and $\mathbf{s}_{n_0}$ are embedding vectors satisfying $\mathbf{s}_i = (y_i, y_{i+\tau}, \ldots, y_{i+(m-1)\tau})$ that are generated by the time-delay reconstruction of the time series sequence $\{y_i\}_{i=0}^{N}$ with delay time (τ) and embedding

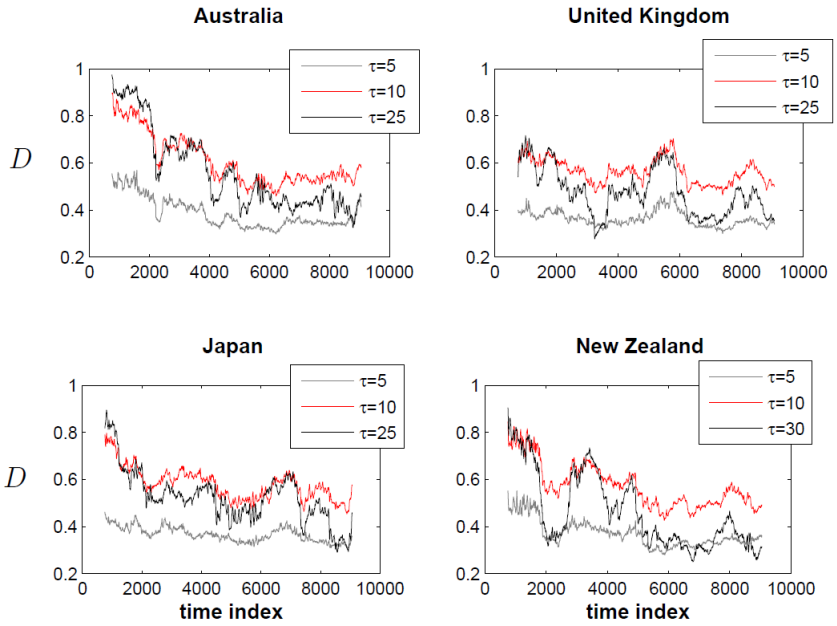

Fig. 2. D curves for the investigated ForEX series (subsegments set ${}_pD_{1500,5}$) where $m = 6$, $N_{ref} = 500$, $N_\epsilon = 20$, $w = 80$, $N_{surr} = 100$.

dimension (m). k is the time evolution parameter where δk is the time span of the reference trajectory to calculate Λ statistics. $\mathcal{U}_\epsilon(\mathbf{s}_{n_0})$ is the temporally uncorrelated neighborhood of $\mathbf{s}_{n_0}$ where at least N_ϵ vectors are found.

D is a measure of direct distance between Λ_{orig} and Λ_{surr} scores which can be evaluated as a similarity measure that defines the rate of 'geometrical equivalence' of Λ curves for original and random shuffled surrogates. Obviously D depends on many parameters which lead to the form for any p given in Equation(4).

$$ {}_{(p)}D_{n,l}(\cdot) =_{(p)} D_{n,l}(m, \tau, N, N_k, N_{surr}, N_\epsilon, N_{ref}, w) \tag{4} $$

m embedding dimension
τ delay time
N length of time series sequence
N_k time span of the reference trajectory vectors
N_{surr} number of surrogates
N_ϵ neighbor trajectory vectors
N_{ref} number of reference trajectory vectors
w minimum window length for temporal correlation

The notation ${}_{(p)}\mathcal{D}_{n,l}$ is used to describe the p^{th} subinterval of the original series $\{y\}_{i=1}^{N}$ of length n with a shifting parameter l. Then the absolute distance

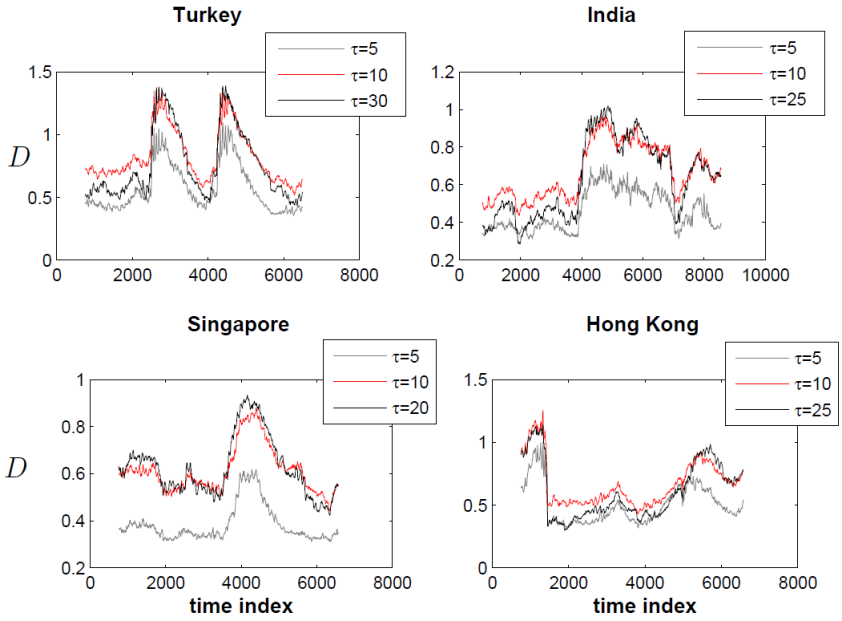

Fig. 3. D curves for the investigated ForEX series (subsegments set ${}_pD_{1500,5}$) where $m = 6$, $N_{ref} = 500$, $N_\epsilon = 20$, $w = 80$, $N_{surr} = 100$.

between two subsegments is l. The D statistics are calculated via reconstructing the phase space of these distinct subsegments.

Our findings on the ForEX rates let us to group the series in to two main categories. The first group (I) includes Australia, UK, Japan and New Zealand where their D statistics exhibit long term decreasing trend for the last 40 years (see Figure.(2)). The mentioned trend is obvious for Australia and Japan. The second group (II) includes Turkey, India, Singapore and Hong-Kong where each series has their own characteristic fluctuations, probably depending on the financial events in their history (see Figure.(3)). The fluctuations in the second group is conjunctural including the jumps across different global phases. The main difference of the sets is the decay pattern of fluctuations. Obviously the series in group I are all developed economies whereas the second group includes developing countries which brings the possibility of financial stability issues effecting nonlinear statistics. Such stability issues are discussed in [2] where the balance of trade data indicating the stability are consistent with their classification.

4 Results and Discussion

In this short work, we tried to analyze the classification of ForEX series based on Lyapunov exponents as the nonlinear statistics. We support that such a classification of financial time series has ability to put forward bright understanding towards the nature of the system. In [15] Thomas Schreiber argue the

validity of nonlinear statistics whether they are supposed to diverge from the original value. He states that, "*we do not have to worry too much about the theoretical basis of the quantities. The results are validated by the statistical significance for the discriminative power. The classification of states can give valuable insights into the structure of a problem*". From this point of view, we give results of related works which make a clear distinction for both spatial (between countries) and temporal (between different time segments of ForEX series) patterns. Our next investigation will be based on the statistical clustering applications of nonlinear measures through a possible link between daily return risk and nonlinear statistics from a temporal perspective.

References

1.J. L. Mccauley. *Dynamics of Markets: Econophysics and Finance*, 2004. Cambridge University Press

2.A. Das and P. Das. Chaotic analysis of the foreign exchange rates . *Applied Mathematics and Computation*. 185(1):388-396,2007.

3.G. Çoban and A. H. Büyüklü. Deterministic flow in phase space of exchange rates: Evidence of chaos in filtered series of Turkish LiraDollar daily growth rates. *Chaos, Solitons & Fractals*, 42(2):1062-1067, 2009.

4.Çoban, G. and Büyüklü, A. H. and Das, A. A linearization based non-iterative approach to measure the gaussian noise level for chaotic time series. *Chaos Solitons and Fractals*,45(3):266-278,2012

5., G. Çoban, A. H. Büyüklü, A. Das and Pritha Das. Behavior Of The Distance Between Exchange Rates Series And Their Surrogates: An Investigation Of Signal to Noise Ratio. In A. Das, editor, *Nonlinear Studies: The Financial Markets And Foreign Exchange Rate*, Technical Monograph, 2010. VDM-Verlag.

6.D. A. Hsieh. Chaos and Nonlinear Dynamics: Application to Financial Markets. *The Journal of Finance*. 46(5):1839-1877, 1991.

7.J. A. Scheinkman. Nonlinearities in Economic Dynamics. *The Economic Journal.*(Conference Papers). 100(400):33-48, 1990.

8.C.J. Cellucci, A.M. Albano, P.E. Rapp, R.A. Pittenger, and R.C. Josiassen. Detecting Noise in a Time Series, *Chaos* 7(3):414-422, 1997.

9.J. Gao. Recognizing randomness in a time series. *Physica D: Nonlinear Phenomena*, 106(1):49-56, 1997.

10.I. A. Moosa, Exchange Rate Forecasting: Techniques and Applications, London, 2000. Macmillian Press.

11.Euro News. Country wise crisis (both EU and non-EU countries) at http://euronews.eu/tag/financial-crisis/. Visited Jan. 2010.

12.T. Schreiber and A. Schmitz. Discrimination power of measures for nonlinearity in a time series. *Phys. Rev. E*, 55:5443, 1997.

13.J. Gao and Z. Zheng. Direct dynamical test for deterministic chaos and optimal embedding of a chaotic time series. *Phys. Rev. E.* 49:38073814, 1994.

14.J. Theiler, and S. Eubank, A. Longtin, B. Galdrikian, J. D. Farmer,Testing for nonlinearity in time series: the method of surrogate data. *Physica D Nonlinear Phenomena*, 58:77-94, 1992.

15.T. Schreiber. Interdisciplinary applications of nonlinear time series analysis. *Physics Reports*, 308:1-64, 1999.

Chaotic Modeling and Simulation (CMSIM) 3: 519–527, 2012

Linear Least Squares Estimate of Noise Level in Chaotic Time Series via L_∞ Norm Correlation Sum

Gürsan Çoban[1], Ali H. Büyüklü[2], and Atin Das[3]

[1] Istanbul Technical University, Institute of Informatics, Division of Computational Science & Engineering, Istanbul, TURKEY
(E-mail: gursan.coban@be.itu.edu.tr)
[2] Yıldız Technical University, Department of Applied Statistics, Davutpaşa, Istanbul, TURKEY
(E-mail: hbuyuklu@yildiz.edu.tr)
[3] NH School, Naktala, Calcutta, INDIA
(E-mail: dasatin@yahoo.co.in)

Abstract. In this work we extend the details of a linear least squares method to estimate the noise level in chaotic time series which has been previously proposed in [1]. For this purpose we analyze a non iterative algorithm based on the functional form obtained by Schreiber in 1993 where the effects of noise on L_∞ norm correlation sums can be quantified via the nonlinear functional. The modified version of the functional leads to a linear approach that gives satisfactory results for simulated continuous flow data even for high level of noise contamination (up to 80%). The approach is especially useful to determine the effective fitting range of data. The range is limited by the curvature effects of the attractor and fluctuations in small scales. We also seek for a phenomenological model for the curvature effect depending on the empirical distribution of estimation errors.
Keywords: linearization, noise level, chaos, curvature effect, data analysis.

1 Introduction

For the last three decades, analysis of chaotic time series has seen a great many numbers of improvements and has became one of the most demanded approach while investigating the systems with unpredictable complex behavior. Chaotic analysis of complex systems usually takes its form through determination of global structural properties (invariants) and the concept of nonlinear prediction. The system under investigation may be perceived as a random fluctuation whereas its behavior is controlled by a system of nonlinear deterministic equations, sometimes disturbed by observational or dynamic noise source. Although it is possible to separate the noise and signal via conventional spectral techniques, it is not the case for chaotic systems which show broadband spectra.

Received: 30 July 2011 / Accepted: 31 March 2012

ISSN 2241-0503

For such a situation, it is crucial to comprehend the main source of fluctuation whether it is generated by pure random noise or any nonlinear dynamical system. If we are interested in the analysis of real world observations such as financial time series, atmospherical measurements or trajectory of planetary motions, then the observations are mostly a combination of the two. However the weights in this combination may be related to the nature of the phenomena.

For noisy observations of a deterministic system, random noise contaminant is evaluated as a negative effect that give rise to serious bias in the estimations of statistical quantities related to the dynamics. This effects the reliability of the information obtained from the system which is supposed to define its overall behavior. Especially for the algorithms to calculate the invariants of the chaotic dynamics, noise narrows the effective scaling ranges for computations, since most of them has been derived under noise-free assumptions. Taking into account of the effects of random noise on the analytical form of the invariants is also advantageous to describe the exact amplitude of noise corruption which can be extracted from the usual invariant statistics. Many of the algorithms have been proposed using the mentioned framework.

In this work, we give a linear least square algorithm for the noise level determination approach used in [2]. We also seek for a phenomenological model for the curvature effects depending on the empirical distribution of estimation errors. The sections are arranged as follows: in Section 2 we give the brief results of the literature dealing with the noise estimation algorithms depending on correlation sum. We also describe a new linear algorithm for noise estimation. In Section 3 we discuss about the *curvature effects* which has strong bias for the map data while using Schreiber's approach. In this section we also propose an empirical model for the characterization of this effect depending on our high-resolution simulations using synthetic chaotic data. Our conclusions and future perspectives about some open problems are given in Section 4.

2 A Linear Algorithm for Noise Estimation

In chaotic systems, the spatial distribution of phase space vectors follows the power law for relatively small length scales compared to the attractor size. Noise shows its disturbing effects on the distribution of nearby vectors that are closer than ϵ distance in phase space. General approach to determine the noise amplitude is to append the analytical form of the disturbance effects on to the mathematical form of invariant descriptions. For example Liu et.al [11] proposed an analytic technique where noise level could be estimated from the geometrical form of the exponential divergence curves [12]. On the other hand studies adopting correlation sum approaches exploit the effects of noise disturbance on the point density over the attractor. Due to the self-similarity, the point distribution follows the very basic power law. If we consider the definition of correlation sum approach [13], the point distribution depends on the fractal dimension of (D_2) the system. For the length scales $\epsilon \to 0$ the distribution is given by,

$$C(\epsilon) \propto \epsilon^{D_2} \tag{1}$$

where $C(\epsilon)$ is defined as,

$$C(\epsilon) = \lim_{N\to\infty} \frac{1}{N^2} \sum_{i,j=1}^{N} \Theta(\epsilon - \| \mathbf{s}_i - \mathbf{s}_j \|) \tag{2}$$

In Eq.(2), $\| \cdot \| = \| \cdot \|_{L_\infty}$ and $\mathbf{s}_{i,j}$ are embedding vectors satisfying $\mathbf{s}_i = (y_i, y_{i+\tau}, \ldots, y_{i+(m-1)\tau})$ that are generated by the time-delay reconstruction of the time series sequence $\{y_i\}_{i=0}^{N}$ with delay time (τ) and embedding dimension (m). Then the Heaviside step function $\Theta(\cdot)$ is used to estimate the probability of a nearby trajectory vector to fall inside the selected hypercube of side length 2ϵ.

If the measurements are noisy, then the functional form in Eq.(2) for L_2 can be represented by the complicated form given by Smith [3] and a modified version discussed in [6]. By using the correlation sum definition in [6], Jayawardena et.al [4] gave a linear least squares approach to detect the noise level in chaotic time series. They have shown that the correlation function in [6] satisfies an ordinary linear differential equation where it is possible to extract both dimension and noise level information by a least squares fitting of calculated correlation sum data.

Our approach here is different from [4] in terms of the norm definition. Schreiber [2] has shown that the L_∞ norm definition of correlation sum can be used to estimate the noise amplitude σ via the nonlinear functional $g(\cdot)$. In this case the effects of noise on the spatial distribution is characterized by (the usual form),

$$d_m(\epsilon) = d_r(\epsilon) + (m-r) g(\frac{\epsilon}{2\sigma}), \quad g(z) = \frac{2}{\sqrt{\pi}} \frac{z\, e^{-z^2}}{\mathrm{erf}(z)} \tag{3}$$

The correlation dimension estimates obtained from n dimensional embedding space d_n is defined by,

$$d_n = \lim_{\epsilon\to 0} \lim_{N\to\infty} d_n(\epsilon), \quad d_n(\epsilon) = \frac{d \ln(C_n(\epsilon))}{d \ln(\epsilon)} \tag{4}$$

In Eq.(3) embedding space of m dimensions should theoretically satisfy $m > r > 2d$, whereas $m > r > d$ give better estimates. It is possible to show that the noise functional $g(z)$ can be represented in terms of the confluent type hypergeometric function of the first kind ${}_1F_1$, such that,

$$g(z) = \left({}_1F_1(1, \frac{3}{2}, z^2) \right)^{-1} \tag{5}$$

where ${}_1F_1(a, c, x)$ can be defined by the integral representation in Eq.(6).

$${}_1F_1(a, c, x) = \frac{\Gamma(c)}{\Gamma(a)\Gamma(c-a)} \int_0^1 e^{xt}\, t^{a-1}\, (1-t)^{c-a-1}\, dt \quad c > a > 0 \tag{6}$$

We approximate the gaussian noise functional by a *stretched exponential decay* function (Eq.(7)), where longer derivations including the asymptotic expansion of the form in Eq.(5) was explained in [1]. The final form is,

$$g(z) = \frac{2}{\sqrt{\pi}} \frac{z\, e^{-z^2}}{\mathrm{erf}(z)} \approx e^{-\alpha\, z^{\lambda}} \tag{7}$$

in which (α, λ) are optimized parameters for $g(z)$ (see [1]). Although there has been successful attempts to directly fitting (global optimum) the exponentials, it is noted that there is still not a direct technique that linearize the exponentially scattered data in to a linear one except ordinary *log* transformation (see [7]). In the present work we follow a relatively practical way to linearize the functional form that was obtained in Eq.(7) by converting the original exponential fitting problem in to an initial value problem (IVP) which is linear in its parameters [14]. Since $g(z) = \exp(-\alpha z^{\lambda})$, then $g(z)' = -\alpha\, \lambda z^{\lambda-1} g(z)$ with initial condition $g(0) = 1$. Despite being a basic property of dimension estimates for small length scales, statistical fluctuations of the data accumulated in $g(z)$ can be efficiently smoothed via the integration based solution. Finally, the linear least squares algorithm for the solution of the mentioned differential equation for $z_i = \epsilon_i / 2\sigma$ yields with,

$$\min \left(\sum_{i=1}^{N} w(z_i) \left\{ g(z_i) + \alpha\, \lambda \int_0^{z_i} z^{\lambda-1} g(z)\, dz - g(0) \right\}^2 \right) \tag{8}$$

including the multiplier term $w(z_i)$ as the statistical weighting factors.

System $N = 20000$	NR	NR $(real)$	$\hat{NR}$ $(estimated)$	σ $(real)$	$\hat{\sigma}$ $(estimated)$	Linear Region
Henon	0.05	0.0502	0.0518	0.0363	0.0374	0.12-0.77
$\sigma_s = 0.72210$	0.20	0.1995	0.2285	0.1444	0.1653	0.19-0.71
	0.50	0.5015	0.6094	0.3629	0.4410	0.17-0.47
Rössler	0.10	0.1004	0.1122	0.8020	0.8957	0.07-0.71
$\sigma_s = 7.9328$	0.40	0.3999	0.4451	3.1933	3.5534	0.16-0.77
	0.80	0.8001	0.8698	6.3876	6.9442	0.23-0.88
Lorenz	0.10	0.1001	0.1090	0.7923	0.8628	0.11-0.734
$\sigma_s = 7.9193$	0.40	0.3989	0.4452	3.1575	3.5251	0.15-0.77
	0.80	0.7963	0.8548	6.3047	6.7675	0.23-0.70

Table 1. Estimated noise amplitudes ($\hat{\sigma}$) by the proposed linear algorithm in Eq.(8). Number of observations for all series is $N = 20000$ where transients are discarded.

We test the algorithm on Lorenz, Rössler flow systems and Henon map to see the efficiency (Table.1). Here and in the following, NR ratio is defined as

the standart deviation of the noise contaminant σ_n divided by the standard deviation of the original noise free signal σ_s, $NR = \sigma_n/\sigma_s$. In Table.1 it can be observed that the linear algorithm works relatively well for the flow data whereas it has strong positive bias for maps. It is clear that the noise estimations for flow systems give reasonably acceptable estimates for extreme noise levels up to 80% ($NR = 0.8$) . In Section 3 we discuss the dominant effect of curvature of the attractor geometry which cause bias for map data.

3 Empirical Modeling of Curvature Effects: The Peak Function Approach

For some statistics obtained from a chaotic time series, the *curvature effect* is dominant. From a technical point of view, the curvature effect is highly related to the limit assumption of $\epsilon \to 0$ made on the point distribution over the attractor. In the literature the bias of density estimates sourced from geometric effects is related to various concepts such as *edge* or *boundary* effect. The sparsity pattern in relatively small scales also cause measurement bias and related to the *lacunarity* of the attractor. However the relationship between noise level and the bias of estimations caused by macroscopic geometric effects has not been clearly described. In this section our aim is to represent the results of our simulations and describe the effects of attractor geometry when the noise level is extremely high.

The point density measurements obey the power law for very small scales. However for large distances ($\epsilon >> 0$) the macro-scale geometrical characteristics of the attractor is dominant for the density measurements which may violate the power law assumption. This problem comes into prominence especially for the correlation dimension estimates where they suffer from positive bias.

Noise level determination algorithms that use information coming from for both micro-macro geometrical features are highly effected from the curvature effects. For instance the ones that use the point density measurements. For low level of noise ratios (NR) the estimated amplitudes are very accurate, whereas estimated noise levels that are comparable to the size of the original attractor show strong positive bias up to a 50% relative error rate. Here and in the following, we define the relative error rate (RE) as the deviation of estimated noise amplitude $\hat{\sigma}$ from the real measurement σ_n, $RE = (\hat{\sigma} - \sigma_n)/\sigma_n$. It is known that Schreiber's algorithm gives overestimated results for $0.2 < NR < 0.8$ which was investigated by Leontitsis et.al in [8]. They have shown that the maximum norm estimation of noise function can be used as a practical way to eliminate negative effects curvature. The prediction algorithm has been also implemented to an adaptive locally projective noise reduction technique in [9]. The algorithm is also useful to describe the overall noise measurements through non-adaptive techniques while analyzing financial time series [10].

In this section we investigate the empirical properties of curvature effects and give a phenomenological model for the distribution of error rates. For a computational description in noise-free systems we refer the reader to the work

in [15]. Analytic description of the effect is possible, however we do not consider such a mathematical model here. Here we will investigate another situation: Destruction of the attractor geometry will eliminate any kind of geometrical effect, since the chaotic attractor is converted in to a '*geometrically formless*' situation resembling the multivariate normal distribution.

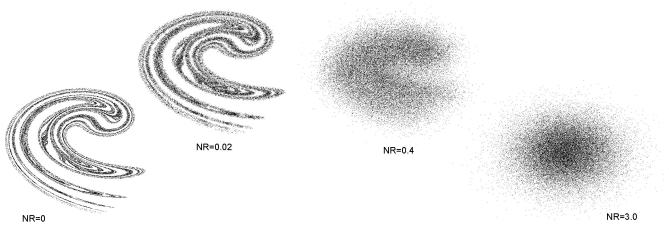

Fig. 1. Destruction of curvature effects on the chaotic Ikeda Map by adding gaussian noise to data ($NR = 0\%,\ 2\%, 40\%, 300\%$).

One way to eliminate all the curvature effects from the attractor is to add appropriate amount of white noise to the original system. In this case, the macro scale geometric form of the system is destroyed and becomes formless (Figure(1)). To support the idea, we test the situation on well known chaotic systems including Henon, Ikeda, Predator-Prey and Lorenz systems. All series have $N = 1500$ observations where transients are excluded. We continuously add normally distributed noise to the systems and estimate the noise level via the nonlinear version of Schreiber's algorithm on $\sigma < \epsilon < 4\sigma$ interval. When the noise ratio exceeds $3\sigma_s$ ($NR > 3$), then any curvature effect is eliminated. The relative error rates for all chaotic systems has a peak position in the interval $0.5 < NR < 1.5$ where the peak level and position seems to depend on the characteristics of the macroscopic geometry. The common features of error distributions is concordant with the behavior of a peak function: 0 level error rates for low noises, a peak point for some noise level and an asymptotic descent of the error rates until convergence to a minimum, while $\sigma_n/\sigma_s \to \infty$. Since we do not make any prior assumptions, we have selected a log-normal type peak function to describe the situation. The relative error rates of a chaotic system arisen from the curvature effect is then modeled by h function in Eq.(9).

$$h(\sigma) = re_0 \left(\frac{\sigma}{\sigma + 1} \right) + \frac{\kappa}{\sqrt{2\pi}\, w\, \sigma}\, e^{-\frac{(\ln(\sigma/x_c))^2}{2\, w^2}} \tag{9}$$

If the original series is corrupted by gaussian noise with standard deviation of ε, it is possible to model the curvature effects via adding increasing amounts of noise with standard deviation of σ_{add}. The final noise amplitude is estimated by $\sigma \approx (\sigma_{add}^2 + \varepsilon^2)^{1/2}$. Since we do not have any information about the relative error rates, observed standard deviations should be used. By using the form used in Eq.(9), the peak model yields the final form in Eq.(10),

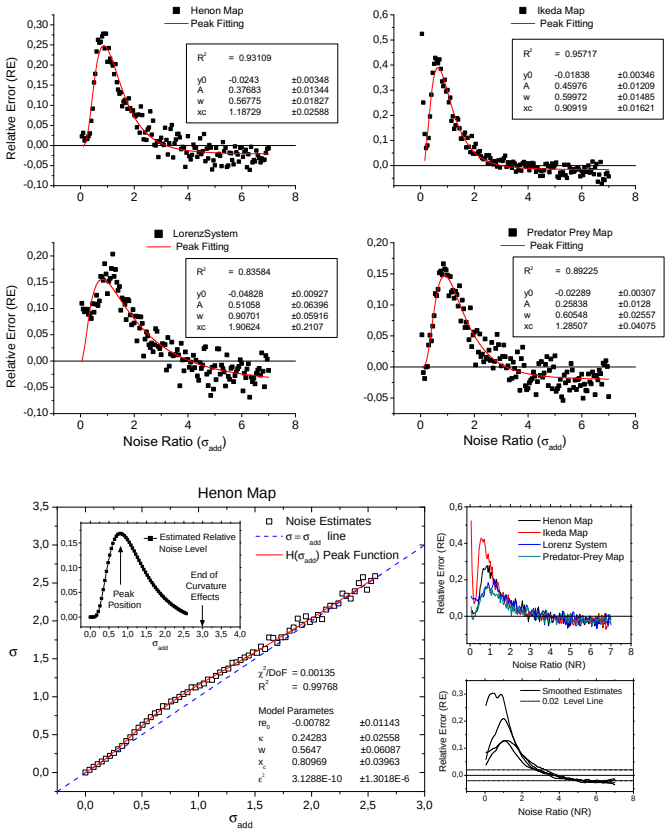

Fig. 2. Upper Panel: The right skewed distribution of relative error rate scores with respect to the noise level for various chaotic systems. The distribution is characterized by a log-normal peak function of type $y = y_0 + \frac{A}{\sqrt{(2\pi)}\, w\, xc} \exp(-(\ln(x) - xc)^2/2w^2)$. Lower Panel: Modeling curvature effects via peak function approach described in the text. Left panel: The noise estimates represent significant deviation from the 45^0 degree line (blue) which can be efficiently modeled by the phenomenological approach. Right panel: The simulation results for four different chaotic systems and moving average smoothed curves.

$$H(\sigma_{add}) = (\sigma_{add}^2 + \varepsilon^2)^{1/2} \, (re_0 (\frac{(\sigma_{add}^2 + \varepsilon^2)^{1/2}}{(\sigma_{add}^2 + \varepsilon^2)^{1/2} + 1} + \frac{\kappa}{\sqrt{2\pi}\, w\, (\sigma_{add}^2 + \varepsilon^2)^{1/2}} \, e^{-\frac{(\ln((\sigma_{add}^2 + \varepsilon^2)^{1/2}/x_c))^2}{2\, w^2}} + 1) \qquad (10)$$

which is obviously extremely nonlinear, but still useful to describe the effects. From Figure.(2), it can be seen that the fitting of error function H accommodates well with the simulated data (significance of model and param-

eters). If the noise level let one to describe the position of peak error rate, it is possible to make better estimates for the exact level of noise via the peak function approach. On the other hand, for noise levels $NR >> 1$ where it goes far beyond the peak position, it would be difficult to make reasonable estimations for exact noise amplitude due to the nonlinearity of $H(\cdot)$ suffering from local minima.

4 Results and Discussion

In this work we have discussed a linear least squares method to estimate the noise level in chaotic time series. The efficiency of the method on map and flow data are discussed. Although the proposed linear approach is used for to estimate the noise level of a chaotic time series, it could also be used to determine the initial feasible estimates for nonlinear algorithms. Positive bias still exists for linear approach where we have proposed a novel approach to model the curvature effects depending on the distribution of estimation errors. Our future investigations will be based on the analytical description of curvature effect.

References

1.G. Çoban, A. H. Büyüklü, and A. Das. A linearization based non-iterative approach to measure the gaussian noise level for chaotic time series. *Chaos Solitons and Fractals*. 45:266-278, 2012.
2.T. Schreiber. Determination of the noise level of chaotic time series. *Physical Review E*. 48:13-16, 1993.
3.R. L. Smith. Estimating Dimension in Noisy Chaotic Time Series. *Journal of the Royal Statistical Society. Series B (Methodological)*. 54(2):329-351, 1992.
4.A. W. Jayawardena, P. Xu, W. K. Li. A method of estimating the noise level in a chaotic time series. *Chaos*. 18(2):(023115 11), 2008.
5.H. Oltmans, P. J. T. Verheijen. Influence of noise on power-law scaling functions and an algorithm for dimension estimations. *Physical Review E*, 56(1):1160-1170, 1997.
6.C. Diks. editor, In *Nonlinear Time Series Analysis: Methods and Applications*, 1999, World Scientific.
7.K. Holmström, J. Petersson. A review of the parameter estimation problem of fitting positive exponential sums to emprical data. *Applied Mathematics and Computation*. 126(1):31-61, 2002.
8.A. Leontitsis , J. Pange , T. Bountis. Large Noise Level Estimation. *International Journal of Bifurcation and Chaos*. 13(8):2309-2313, 2003.
9.A.Leontitsis , T. Bountis , J. Pange. An adaptive way for improving noise reduction using local geometric projection. *Chaos*. 14(1):106-110, 2004.
10.G. Çoban and A. H. Büyüklü. Deterministic flow in phase space of exchange rates: Evidence of chaos in filtered series of Turkish LiraDollar daily growth rates. *Chaos, Solitons & Fractals*, 42(2):1062-1067, 2009.
11.H. F. Liu, Z. H. Dai, W. F. Li, X. Gong, Z. H. Yu. Noise robust estimates of the largest Lyapunov exponent. *Physics Letters A*. 341(1-4):119-127, 2005.
12.J. Gao and Z. Zheng. Direct dynamical test for deterministic chaos and optimal embedding of a chaotic time series. *Phys. Rev. E*. 49:38073814, 1994.

13.P. Grassberger, I. Procaccia. Characterization of Strange Attractors . *Physical Review Letters*. 50:346-349, 1983.
14.E. G. Novikov , A. van Hoek , A. J. W. G. Visser , J. W. Hofstraat. Linear algorithms for stretched exponential decay analysis. *Optics Communication*. 166(1-6):189-198, 1999.
15.H. Heng and M. Bauer and W. Martienssen, Correlation integrals for inhomogeneously distributed random data, *Chaos, Solitons & Fractals*. 7(2): 197-203, 1996.

Chaotic Modeling and Simulation (CMSIM) 3: 529-542, 2012

Adaptive Control of Mixed-Interlaced forms

Kyriakos G. Vamvoudakis[1], Manolis A. Christodoulou[2]

[1] Automation and Robotics Research Institute, The University of Texas at Arlington, 7300 Jack Newell Blvd. S., Ft. Worth, TX 76118
[2] Technical University of Crete, Chania, Crete, Greece
(E-mail: kyriakos@arri.uta.edu , manolis@isc.tuc.gr)

Abstract: In this paper we combine forwarding and backstepping techniques to stabilize mixed interlaced systems. All the signals in the close loop remain semiglobally ultimately bounded the output signal y follows a desired trajectory signal y_d, with bounded derivatives up to m^{th} order. We also present simulation examples that prove the adaptation of mixed interlaced forms, using a backstepping controller.

1 Introduction

Recent technological developments have forced control engineers to deal with extremely complex systems that include uncertain and possibly unknown nonlinearities, operating in highly uncertain environments. Man has two principal objectives in the scientific study of his environment: he wants to understand and to control. The two goals reinforce each other, since deeper understanding permits firmer control, and, on the other hand, systematic application of scientific theories inevitably generates new problems which require further investigation, and so on. Nonlinear control includes two basic forms of systems, the feedforward systems and the feedback systems.

The strict feedback systems can be controlled using the well known backstepping technique. The purpose of backstepping is the recursive design of a controller for the system by selecting appropriate virtual controllers. Separate virtual controllers are used in order to stabilize every equation of the system. In every step we select appropriate update laws. The strict feedforward systems can be controlled using the forwarding technique that is something like backstepping but in reverse order. Other cases of systems that can be converted to the previous forms are part of a larger class of systems that are called interlaced systems as described by [9], and [3]. In these systems we combine backstepping and forwarding techniques together in order to recursively design feedback control laws. Interlaced systems are not in feedback form, nor in feedforward form. These systems have a specific methodology that differs from backstepping and forwarding. We don't start from the top equation, neither from the bottom.

Other special cases of systems are part of other forms that we call mixed interlaced and we introduce their study in the present paper. The methodology is based on classical interlaced systems and is developed by the authors. We want

Received: 29 June 2011 / Accepted 30 March 2012

ISSN 2241-0503

to make the systems solvable by one of the well known backstepping and forwarding methods. This can be reached after some specific steps that convert the system into a known form. We start from the middle equation and we continue with the top. The previous method is based on classical interlaced forms that are introduced by [9] and [3] and can be extended to more complicated systems.

A lot of researchers developed a series of results that generalized and explained the basic idea of nonlinear control. Teel [10] in his dissertation introduced the idea of nested saturations with careful selection of their parameters to achieve robustness for nonlinear controllers. After Teel , Sepulchre, Jankovic and Kokotovic [9] proposed a new solution to the problem of forwarding that is based on a different Lyapunov solution.

The paper consists of four sections including the current one. The next section introduces the meanings of Adaptive Control, Backstepping and Forwarding techniques. In Section 3, the main body of this paper, the mixed interlaced forms are analyzed. Finally section 4 draws some concluding remarks.

2 Background in Adaptive Control

The history of adaptive control began from the early 1950's. With the passing of the years a lot of papers and books have been published. These research activities have proposed solutions for basic problems and for broader classes of systems. Especially the interest for nonlinear adaptive control began from the mid-1980's. A lot of great scientists, such as Kokotovic et al [2], Lewis et al [4], Ioannou and Sun [7], Christodoulou and Rovithakis [5] have studied adaptive control and its applications extensively.

Adaptive control is a powerful tool that deals with modeling uncertainties in nonlinear (and linear) systems by on line tuning of parameters. Very important research activities include on-line identification and pattern recognition inside the feedback control loop.

Through time, adaptive control has existed big development (Sepulchre et al [9]) in order to control plants with unknown dynamics that appear linearly. Adaptive control is based on Lyapunov design.

In order to make it clear, a short example will be reported. Let us consider the nonlinear plant:

$$\dot{x} = u + \theta x^2 \tag{1}$$

And select the control law as:

$$u = -qx - \hat{\theta} x^2 \tag{2}$$

which, if the estimated θ ($\hat{\theta}$) is equal to real θ such that $\hat{\theta} \equiv \theta$, then the result is a close loop system of the form:

$$\dot{x} = -qx \tag{3}$$

The filtered version of the signals x is:

$$x_f = \frac{1}{s+1}x^2 \tag{4}$$

The prediction error e is:

$$e = x - \hat{x} = (\theta - \hat{\theta})x_f = \hat{\theta}x_f \tag{5}$$

We use the commonly normalized update law:

$$\dot{\hat{\theta}} = -\frac{\gamma}{1+{x_f}^2}{x_f}^2\tilde{\theta} \tag{6}$$

The previous update law is linear. It can be proved that $\tilde{\theta}$ does not converge to zero faster than exponentially and the easiest case is:

$$\tilde{\theta} = e^{-\gamma t}\tilde{\theta}(0) \tag{7}$$

Finally the close loop system has the following form:

$$\dot{x} = -x + \tilde{\theta}x^2 \tag{8}$$

where for simplicity q substituted with 1 and by substituting $\tilde{\theta}$ from the previous equation is obtained:

$$\dot{x} = -x + e^{-t}\tilde{\theta}(0)x^2 \tag{9}$$

where for simplicity γ substituted with 1.
It is easy to see that the explicit solution of the previous is determined by the following equation:

$$x = \frac{2x(0)}{x(0)\tilde{\theta}(0)e^{-t} + [2 - x(0)\tilde{\theta}(0)]e^{-t}} \tag{10}$$

From the previous it is clear that if $x(0)\tilde{\theta}(0) < 2$ then it is obvious that x converge to zero as $t \to \infty$. At the case that $x(0)\tilde{\theta}(0) > 2$, at the time:

$$t_{esc} = \frac{1}{2}\ln\frac{x(0)\tilde{\theta}(0)}{x(0)\tilde{\theta}(0) - 2}$$

the difference of the two terms of the exponential in the denominator becomes zero, that is:

$$|x(t)| \to \infty \text{ as } t \to t_{esc}$$

The previous model is unstable (x goes to infinity at t_{esc}) and Lyapunov design models must be specified in order to achieve stabilization.
Let choose the following Lyapunov function:

$$V = \frac{1}{2}x^2 + \frac{1}{2}(\hat{\theta} - \theta)^2 \tag{11}$$

The derivative of the Lyapunov function for our nonlinear plant is:

$$\dot{V} = x(u + \theta x^2) + (\hat{\theta} - \theta)^2 \dot{\hat{\theta}}$$

In order to find a control and an update law we must specify:

$$\dot{V} \le -x^2 \Rightarrow x(u + \theta x^2) + (\hat{\theta} - \theta)^2 \dot{\hat{\theta}} \le -x^2 \tag{12}$$

From the previous equation in order to remove the unknown θ we use the update law:

$$\dot{\hat{\theta}} = x^3$$

And the control law is:

$$u = -x - \hat{\theta}x^2$$

Both control law and update law yield $\dot{V} \le -x^2$ such that stability maintains in opposition to the previous approach without Lyapunov.

Adaptive control in most cases has tracking error that converges to zero.

i) Adaptive Backstepping Design

Backstepping ([1], [2], [4], [7]) is a recursive design for systems of the form:

$$\begin{aligned}
\dot{x}_1 &= x_2 + \varphi_1^{\mathrm{T}}(x_1, x_2)\theta \\
\dot{x}_2 &= x_3 + \varphi_2^{\mathrm{T}}(x_1, x_2, x_3)\theta \\
\dot{x}_3 &= u \ + \varphi_3^{\mathrm{T}}(x_1, x_2, x_3)\theta
\end{aligned}$$

with state $x=[x_1^T, x_2^T, x_3^T]$ and control input u. The value θ is a p x 1 vector which is constant and unknown. The function φ_1 depends only to x_1, x_2 function φ_2, φ_3 depends only to x_1, x_2, x_3.

The purpose of backstepping is the recursive design of a controller for the previous system by selecting appropriate virtual controllers. The virtual controller for the first equation of the system is x_2 and is used to stabilize the first equations, the virtual controller for the middle equation is x_3 and is used to stabilize the first two equations, and finally the controller for the last is u. We use separate virtual controllers in order to stabilize every equation of the system. In every step we select appropriate update laws.

In classical backstepping, the output is selected as the state x_1 and the purpose of adaptive control is to make this state to follow a desired trajectory x_{1d}.

Adaptive backstepping design is a Lyapunov based design [4]. The previous procedure can be applied only to systems that have (or transformed to) the previous form (strict feedback).

ii) Adaptive Forwarding Design

Forwarding ([9]) is something like backstepping but for strict feedforward systems. Let us introduce forwarding technique with an example such as:

$$\dot{x}_1 = x_2 + x_3^2 + x_2 u$$
$$\dot{x}_2 = x_3 - x_3^2 u$$
$$\dot{x}_3 = u$$

In the previous example we do not have feedback paths.
Firstly we stabilize the last equation ($\dot{x}_3 = u$). We take the following Lyapunov function:
$V_3 = \frac{1}{2} x_3^2$ and a feedback to stabilize the system is $u = -x_3$. With the previous we augment $\dot{x}_3 = -x_3$ by the middle equation, and write our system in the cascade form:

$$\dot{x}_2 = \varphi_2(x_3)$$
$$\dot{x}_3 = -x_3$$

where $\varphi_2(x_3) = x_3 - x_3^3$ is the interconnection term. $\dot{x}_2 = 0$ is stable and $\dot{x}_3 = -x_3$ is GAS and LES. The next step is to construct Lyapunov function V_2 for the augmented system when V_3 is given.
After some specific steps we reach the following control law:

$$u = -x_3 - (x_2 + x_3 + \frac{{x_3}^3}{3})(1 + {x_3}^2) \tag{13}$$

3 Mixed Interlaced Forms

a. Introduction and Linearization Method

To begin with we consider the following third order mixed interlaced system and via an example we will introduce mixed interlaced forms [12]:

$$\begin{aligned} \dot{x}_1 &= -\beta_3 x_1 + a_{32}(c_3 - x_1)x_2 + a_{31}(c_3 - x_1)x_3 \\ \dot{x}_2 &= -\beta_2 x_2 + a_{23}(c_2 - x_2)x_1 + a_{21}(c_2 - x_2)x_3 \\ \dot{x}_3 &= -\beta_1 x_3 + (c_1 - x_3)u(t) \end{aligned} \tag{14}$$

The previous system is not in feedback nor is it in feedforward form because of specific terms such as x_1x_2, x_1x_3, x_2x_3. The Jacobi linearization of the previous system is a chain of integrators.

Instead from starting on top, we start from the middle equation and treat x_3 as virtual control and we want $\dot{x}_2 = -x_2$ for stability. There exists a Lyapunov function of the form $V_1 = \frac{1}{2}{x_2}^2$ and a stabilizing feedback is $x_3 = \frac{-\beta_2 x_2 + a_{23}c_2x_1 - a_{23}x_2x_1 + x_2}{a_{21}x_2 - a_{21}c_2}$ which is $x_3=a(x_1,x_2)$. We employ one step of backstepping to stabilize the middle equation augmented by the top equation of our system:

$$\begin{aligned} \dot{x}_1 &= -\beta_3 x_1 + a_{32}(c_3 - x_1)x_2 + \\ &+ a_{31}(c_3 - x_1)\left(\frac{-\beta_2 x_2 + a_{23}c_2x_1 - a_{23}x_2x_1 + x_2}{a_{21}x_2 - a_{21}c_2}\right) + \\ &+ a_{31}(c_3 - x_1)v \\ \dot{x}_2 &= -x_2 + v \end{aligned} \tag{15}$$

where the control x_3 has been augmented to $x_3=a(x_1,x_2)+v$. With v=0, the equilibrium $(x_1,x_2)=(0, 0)$ is globally stable and forwarding yields the following Lyapunov function:

$$V_2 = V_1 + \lim \tilde{x}_1(s)$$
$$= \frac{1}{2}x_2{}^2 + \frac{1}{2}\xi_1{}^2, \qquad (16)$$
$$\xi_1 = x_1 + x_2 - \frac{1}{2}x_2{}^2 - \frac{1}{3}x_2{}^3$$

The feedback law: $v = -(1-x_2{}^2)\xi_1$ maintains the system globally stable and the augmented control is

$$x_3 = a_1(x_1, x_2) \ + v = \frac{-\beta_2 x_2 + a_{23}c_2 x_1 - a_{23}x_2 x_1 + x_2}{a_{21}x_2 - a_{21}c_2} \qquad (17)$$
$$-(1-x_2{}^2)\xi_1 \ = a_2(x_1, x_2, \xi_1)$$

In order to stabilize our system we apply the backstepping technique.

b. Mixed Interlaced Forms, Adaptive Control and Simulations

Adaptive Control of dynamical systems has been an active area of research since the 1960's. The system is described by the following figure:

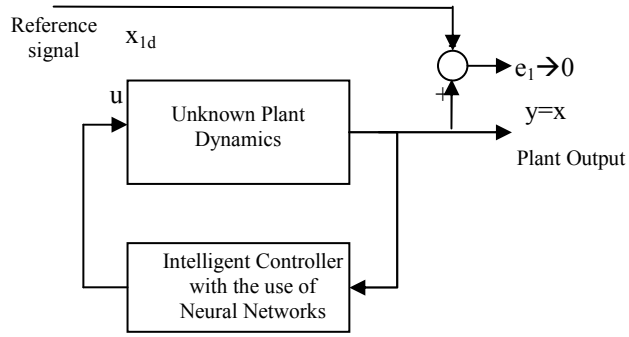

Because we have 3 states our controller design is described with Kaynak et al [1] controller in 3 steps.

Step1: In this step we want to make the error between x_1 and x_{1d} $(=y_d)$ as small as possible.

The previous is described by the following equation:

$$e_1 = x_1 - x_{1d} \qquad (18)$$

We take the derivative of e_1. After that we have:

$$\dot{e}_1 = \dot{x}_1 - \dot{x}_{1d} \Rightarrow \dot{e}_1 = f_1(x_1) + g_1(x_1)x_2 - \dot{x}_{1d} \quad (19)$$

by using x_2 as the virtual control input. The previous equation can be changed by multiplication and division with $g_1(x_1)$ to the following form:

$$\dot{e}_1 = g_1(x_1)[g_1^{-1}(x_1)f_1(x_1) + x_2 - g_1^{-1}(x_1)\dot{x}_{1d}] \quad (20)$$

We choose the virtual controller as:

$$x_{2d} = x_2 = -g_1^{-1}(x_1)f_1(x_1) + g_1^{-1}(x_1)\dot{x}_{1d} - k_1 e_1 \quad (21)$$

where k_1 is a positive constant. In order to approximate the unknown nonlinearities (functions $f_1(x_1)$ and $g_1(x_1)$) we use RBF Neural Networks ([11]). A Neural Network based virtual controller is used as follows:

$$x_{2d} = -\theta_1^{\mathrm{T}}\xi_1(x_1) + \delta_1^{\mathrm{T}}n_1(x_1)\dot{x}_{1d} - k_1 e_1 \quad (22)$$

where we have substituted the unknown nonlinearities $g_1(x_1)^{-1}f_1(x_1)$ and $g_1(x_1)^{-1}$ with the RBF Neural Networks $\theta_1^{\mathrm{T}}\xi_1(x_1)$ and $\delta_1^{\mathrm{T}}n_1(x_1)$ respectively based on Lyapunov stability ([6], [8]).

We take the following adaptation laws (σ-modification) in order to avoid large values of the weights:

$$\dot{\theta}_1 = \Gamma_{11}[e_1\xi_1(x_1) - \sigma_1\theta_1] \quad (23)$$

$$\dot{\delta}_1 = \Gamma_{12}[-e_1 n_1(x_1)\dot{x}_{1d} - \gamma_1\delta_1] \quad (24)$$

with σ_1, γ_1 small and positive constants and $\Gamma_{11}=\Gamma_{11}^T>0$, $\Gamma_{12}=\Gamma_{12}^T>0$ are the adaptive gain matrices.

Step 2: In this step we make the error between x_2 and x_{2d} as small as possible. The previous is described by the following equation:

$$e_2 = x_2 - x_{2d} \quad (25)$$

We take the derivative of e_2. After that we have:

$$\begin{aligned}\dot{e}_2 &= \dot{x}_2 - \dot{x}_{2d} = f_2(\bar{x}_2) + g_2(\bar{x}_2)x_3 - \dot{x}_{2d} \\ &= g_2(\bar{x}_2)[g_2(\bar{x}_2)^{-1} f_2(\bar{x}_2) + x_3 - g_2(\bar{x}_2)^{-1}\dot{x}_{2d}]\end{aligned} \tag{26}$$

By taking the x_{3d} as a virtual control input and by substituting the unknown nonlinearities $g_2(\bar{x}_2)^{-1} f_2(\bar{x}_2)$ and $g_2(\bar{x}_2)^{-1}$ with the RBF Neural Networks $\theta_2^{\mathrm{T}}\xi_2(\bar{x}_2)$ and $\delta_2^{\mathrm{T}} n_2(\bar{x}_2)$ respectively based on Lyapunov stability ([6], [8]), we have:

$$x_{3d} = -e_1 - \theta_2^{\mathrm{T}}\xi_2(\bar{x}_2) + \delta_2^{\mathrm{T}} n_2(\bar{x}_2)\dot{x}_{2d} - k_2 e_2 \tag{27}$$

We take the following adaptation laws (σ-modification) in order to avoid large values of the weights:

$$\begin{aligned}\dot{\theta}_2 &= \Gamma_{21}[e_2\xi_2(\bar{x}_2) - \sigma_2\theta_2] \\ \dot{\delta}_2 &= \Gamma_{22}[-e_2 n_2(\bar{x}_2)\dot{x}_{2d} - \gamma_2\delta_2]\end{aligned} \tag{28}$$

with σ_2, γ_2 small and positive constants and $\Gamma_{21}=\Gamma_{21}^{T}>0$, $\Gamma_{22}=\Gamma_{22}^{T}>0$ are the adaptive gain matrices.

Step 3(Final): In this step we make the error between x_3 and x_{3d} as small as possible.
The previous is described by the following equation:

$$e_3 = x_3 - x_{3d} \tag{29}$$

We take the derivative of e_3. After that we have:

$$\begin{aligned}\dot{e}_3 &= \dot{x}_3 - \dot{x}_{3d} = f_3(\bar{x}_3) + g_3(\bar{x}_3)u \ - \dot{x}_{3d} \\ &= g_3(\bar{x}_3)[g_3(\bar{x}_3)^{-1} f_3(\bar{x}_3) + u - g_3(\bar{x}_3)^{-1}\dot{x}_{3d}]\end{aligned} \tag{30}$$

Where u is the control input and by substituting the unknown nonlinearities $g_3(\bar{x}_3)^{-1} f_3(\bar{x}_3)$ and $g_3(\bar{x}_3)^{-1}$ with the RBF Neural Networks $\theta_3^{\mathrm{T}}\xi_3(\bar{x}_3)$ and $\delta_3^{\mathrm{T}} n_3(\bar{x}_3)$ respectively, we have:

$$u = -e_2 - \theta_3^{\mathrm{T}}\xi_3(\bar{x}_3) + \delta_3^{\mathrm{T}} n_3(\bar{x}_3)\dot{x}_{3d} - k_3 e_3 \tag{31}$$

We take the following adaptation laws (σ-modification) in order to avoid large values of the weights:

$$\dot{\theta}_3 = \Gamma_{31}[e_3\xi_3(\bar{x}_3) - \sigma_3\theta_3]$$
$$\dot{\delta}_3 = \Gamma_{32}[-e_3 n_3(\bar{x}_3)\dot{x}_{3d} - \gamma_3\delta_3] \qquad (32)$$

with σ_3, γ_3 small and positive constants and $\Gamma_{31}=\Gamma_{31}^T>0$, $\Gamma_{32}=\Gamma_{32}^T>0$ are the adaptive gain matrices.

In order to prove the stabilization of mixed interlaced systems we apply the previous described by [1] and we perform the following simulations:

We make the assumption that $c_1>>x_1$, $c_2>>x_2$, $c_3>>x_3$ and $a_{21}=a_{32}=\beta_1=\beta_2=\beta_3=1$, $c_1=9.99$, $c_2=6.66$, $c_3=3.33$. Also we want our desired output to be $y_d=sin(t)$.

Figs. 1-6 show the simulation results of applying the controller for tracking the desired signal y_d. From figure 1 we can see that good tracking performance is obtained. Figure 2 shows the trajectory of the controller. Figure 3 shows the phase plane of the system. Figure 4 shows the error e_1, Figure 5 shows the error e_2 and finally Figure 6 shows the error e_3.

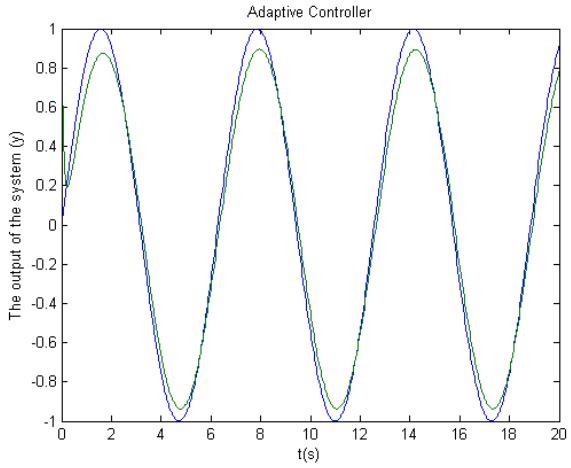

Fig. 1: The output of the system under adaptive controller.

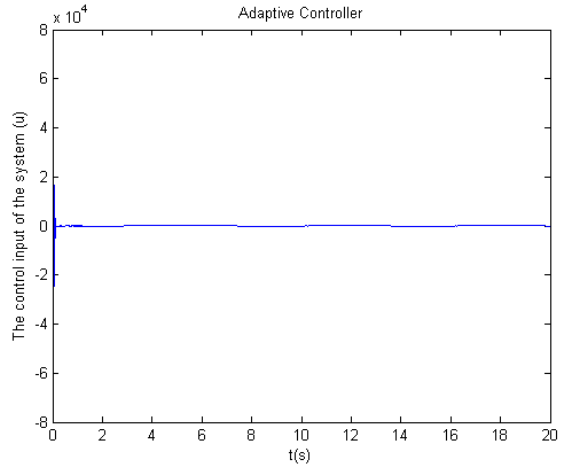

Fig. 2: The trajectory of the adaptive controller.

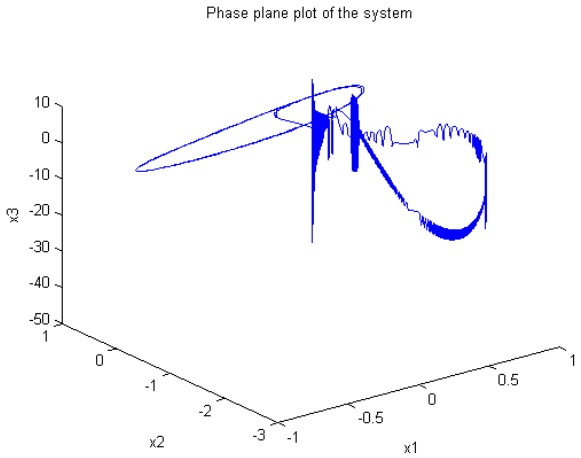

Fig. 3: The phase plane plot of the system.

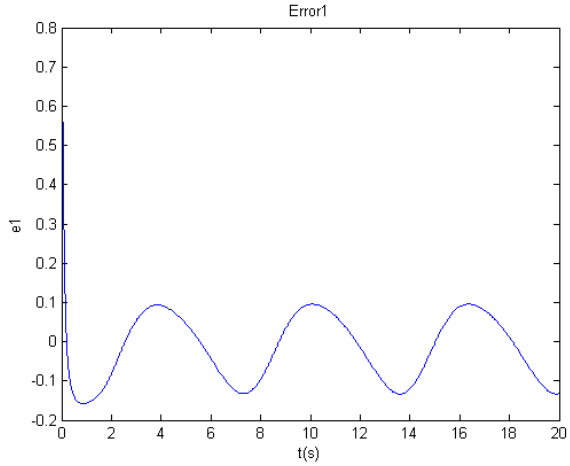

Fig. 4: Error e_1

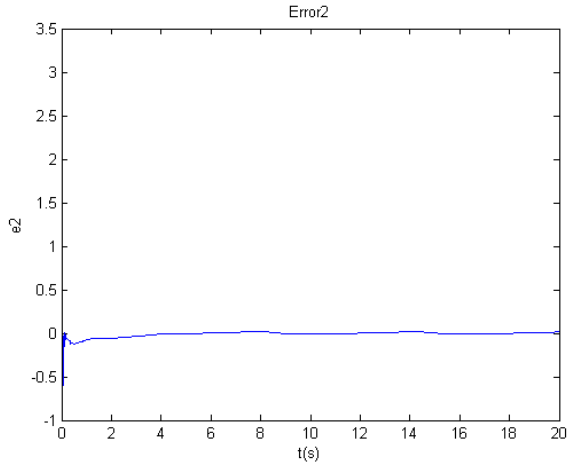

Fig. 5: Error e_2

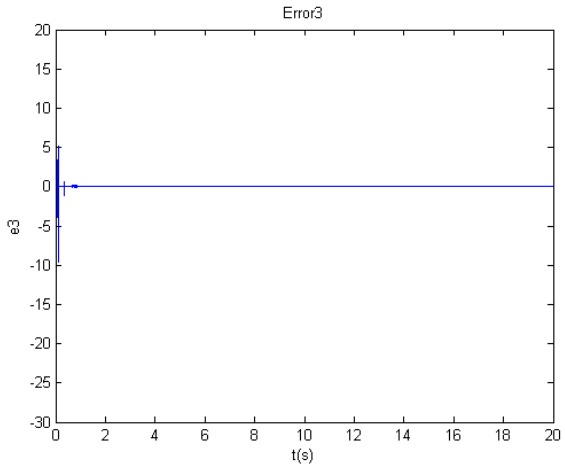

Fig. 6: Error e_3

4 Conclusion

In this paper, we recognize a new form of systems that we call mixed interlaced form. We apply the well known backstepping and forwarding techniques via specific steps. Also Lyapunov functions can be selected to approve convergence and stability. A lot of systems have the mixed interlaced form. For example we can think systems in biological models that have many terms from different states. After the appropriate selection of the controller we can apply adaptive control to make the systems follow a desired trajectory.

The tracking error is bounded and is established on the basis of the Lyapunov approach. Finally, only the states of the unknown plant which are related to the reduced order model are assumed to be available for measurement.

The authors hope that the proposed approach would serve as a promising tool to analyze more complex systems.

References

[1] O. Kaynak, S. Qiang, X. Zhuang, and L. Yahui, "Robust and Adaptive Backstepping Control for Nonlinear Systems Using RBF Neural Networks," *IEEE Trans. Neural Networks*, vol 15, pp 693-701, 2004.

[2] M Krstic, I. Kanellakopoulos, and P. V. Kokotovic, Nonlinear and Adaptive Control Design, New York: Wiley, 1995

[3] M. Krstic, "Feedback Linearizability and Explicit Integrator Forwarding Controllers for Classes of Feedforward Systems," IEEE Trans. on Automatic Control, vol. 49, pp. 1668-1682, 2004.

[4] F. L. Lewis, S. Jagannathan and A. Yesildirek, Neural Network Control of Robot Manipulators and Nonlinear Systems, Taylor & Francis, 1999.

[5] G. A. Rovithakis and M. A. Christodoulou, Adaptive Control with Recurrent high-order Neural Networks, Springer Verlag, New York, USA, 2000.

[6] G. A. Rovithakis, "Tracking Control of multi-inputs affine nonlinear dynamical systems with unknown nonlinearities using dynamical neural networks, "IEEE Trans. Syst., Man, Cybern., vol. 29, pp. 447-451, 1999.

[7] P. A. Ioannou and J. Sun, Robust Adaptive Control, Englewood Cliggs, NJ: Prentice-Hall 1993.
[8] M. Polycarpou and P. A. Ioannou, "Identification and Control Using Neural Network Models: Design and Stability Analysis," Dept. Elect. Eng. Syst., Univ. Southern California, Los Angeles, Tech. Rep. 91-09-01, 1991.
[9] P. V. Kokotovic, R. Sepulchre and M. Jankovic, Constructive Nonlinear Control. New York: Springer Verlag, 1997.
[10] A. R. Teel, "Feedback stabilization: Nonlinear solutions to inherently nonlinear problems," Ph.D., Univ. California, Berkeley, CA, 1992.
[11] R. M. Sanner and J. E. Slotine, "Gaussian networks for direct adaptive control," IEEE Trans. Neural Networks, vol. 3, pp. 837-863, Nov. 1992.
[12] Kyriakos G. Vamvoudakis, Manolis A. Christodoulou, "Adaptive Backstepping Control for MAPK Cascade Models Using RBF Neural Networks," Proc. Mediterranean Conf. Control & Automation, Athens, Greece, June 2007.

Chaotic Modeling and Simulation (CMSIM) 3: 543-550, 2012

The Energy of Generalized Logistic Maps at Full Chaos

Maria Stavroulaki and Dimitrios Sotiropoulos

Department of Sciences, Technical University of Crete
Chania, 73100 Greece
mstavr@mred.tuc.gr, dimsotirop@yahoo.com

Abstract: The energy of generalized logistic maps at full chaos is computed and examined in serving as a guide to multi-disciplinary applications. The maps considered are of the form $x_{n+1} = f(x_n) = r\, x_n^{\lambda}(1-x_n)^{\mu}$, limited above by 1 resulting in the maximum r that yields full chaos; the exponents λ and μ are taken to be any positive real numbers between 0.5 and 2. For given values of r, λ and μ, the average energy is calculated as the average squared x over 512 points starting at the 2049th iteration point. Near full chaos, its dependence on r for fixed values of λ and μ is highly non-linear consisting of a number of maxima and minima. For λ greater than 1.1, the energy diminishes independent of the initial iteration point. At full chaos, the energy dependence on values of λ in the range [0.5, 1.1] and values of μ in the range [0.5, 2] is depicted graphically. For a fixed λ or μ, this dependence is approximated linearly.
Keywords: energy, full chaos, logistic map**,** generalized logistic maps.

1 Introduction

In the present paper, the energy of chaotic generalized logistic maps is computed and examined. The results of the present study may find applications in diverse scientific disciplines such as fracture mechanics, see for example, D. Sotiropoulos [1], social sciences (e.g. Skiadas & Skiadas [2]), population growth modeling (e.g. Marotto [3]), and music composition (e.g. D. Sotiropoulos et al [4]). For applications in astronomy and other areas the reader is referred to the monograph of Skiadas & Skiadas [5].

The generalized logistic maps considered here are of the form,

$$x_{n+1} = r x_n^{\lambda} (1 - x_n)^{\mu} \tag{1}$$

in which the parameters r, λ and μ are positive real numbers, while the variable x and its map range from 0 to 1. The classical logistic map is given by λ=1 and μ=1, whose chaotic nature of the produced x's were discussed by May [6]. A discussion on the x's produced by iteration for λ=1 and μ<1 as well as other specific values may be found in Skiadas & Skiadas [5]. Marotto [3] found that for the case λ=2 and μ=1, there is a range of values of r near its maximum (which is obtained from the condition that the upper limit of x is 1) for which the

Received: 2 April 2012 / Accepted 30 April 2012

ISSN 2241-0503

x's produced are soon after attracted to zero, independent of the initial x chosen in the iteration process. Gottlieb [7] further discussed this by computing a region in the (initial x, r) space in which the produced x's escape the zero value fixed point. The chaotic behavior of the case $\lambda=\mu=1/2$ as applied to music composition was visited by V. Sotiropoulos [8], while that of the double logistic map was examined for music composition by by A. Sotiropoulos [9]. On maps of related functional dependence, Stutzer [10] investigated the iterative map $x_{n+1} = r\ x_n\ (1-x_n^{1/2})$ as a macro-economic dynamic model, while Gottlieb [11] analyzed the map $x_{n+1} = r\ x_n^{3/2}\ (1-x_n^{1/2})$. Skiadas & Skiadas [5] looked at the chaotic behavior of the generalized rational iteration model $x_{n+1} = x_n + r\ x_n\ (1-x_n)/[1-(1-\sigma)x_n]$ with positive σ. Last, D. Sotiropoulos [12] examined in detail the nature and regions of existence of fixed points for the map given by Eq,. (1) above.

The upper limiting value of the map parameter r in Eq. (1) is given in D. Sotiropoulos [12] in terms of the map exponents λ and μ as

$$r_{\max} = (1+\lambda/\mu)^{\mu}(1+\mu/\lambda)^{\lambda} \qquad (2)$$

It is at this value of r which yields full chaos that the energy produced by the map of Eq. (1) will be calculated and studied in the present paper for values of λ in the range [0.5, 1.1] and values of μ in the range [0.5, 2], since it is found in the present study that for λ greater than 1.1 the energy diminishes independent of the initial iteration point. Furthermore, for a fixed λ (or μ) the dependence of the map's energy at full chaos on μ (or λ) will be established analytically by approximating the energy computed from x's resulting from the iterations of Eq. (1).

2 The energy of generalized logistic maps

The energy, E, of the generalized logistic maps given by Eq. (1) is defined as the sum of the squared iterated x's

$$\mathrm{E} = \sum_{n=1}^{N} x_n^2 \qquad (3)$$

The energy clearly depends not only on the map's parameters r, λ and μ but also on the number, N, of x's taken into account in the summation and on the initial x ($=x_1$) selected. To eliminate the energy's dependence on the latter two factors, we divide the energy by a large number N and pick as initial x, the x produced by the map after a large number of iterations so that the resulting energy will be independent of both N and the initial x. Thus, we define the average energy which may be interpreted as the map's generated power as

$$\overline{\mathrm{E}} = \mathrm{E}/\mathrm{N} \qquad (4)$$

The average energy being, therefore, the map's average squared iterated x.

From the numerical calculations performed in the present study, we have concluded that the appropriate initial x to choose in order to satisfy the

aforementioned requirement is the x produced by the map after 2049 iterations. Moreover, in computing an invariant value for the average energy a large number of x's needs to be taken into account and we have concluded that 512 iterations are enough to satisfy this requirement.

As an example of the chaos generated by the map of Eq. (1), the 512 chaotic x's generated at full chaos ($r=r_{max}$) after 2049 iterations with $\lambda=1$ and $\mu=0.5$, 1, 2 are shown in Fig. 1a, b, c.

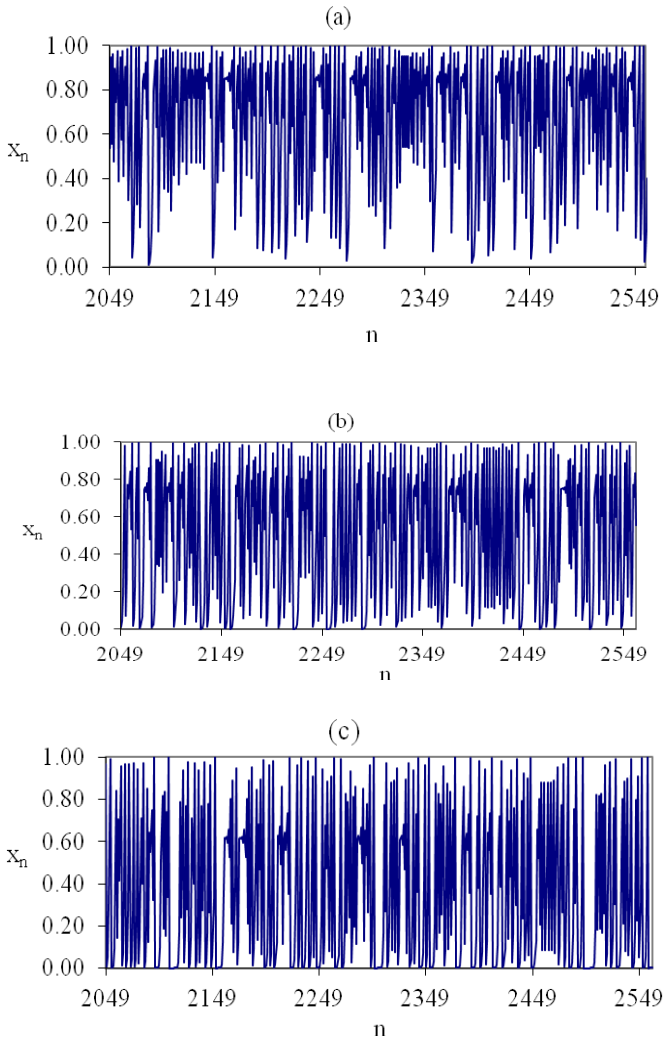

Fig. 1. The fully chaotic productions, x_n, of the generalized logistic maps with $\lambda=1$and $\mu=0.5$ (α), 1 (b), 2 (c)

In Fig.1, the case λ=μ=1 (r=4) corresponds to the classical logistic map [6]. We see that the generated fully chaotic x's are different for the three cases (a) (b) and (c) and, as we shall see in the following section, also the average energy produced is different.

Next, the average energy, $\bar{E}$, of the generalized logistic maps of Eq. (1) is computed using Eqs. (3), (4) for a large range of the map's multiplying parameter r and for different values of λ and μ. The upper limiting value of λ is taken as 1.1 since we have found computationally that larger values yield diminishing energy near full chaos (maximum r) as the generated x's go to the fixed point zero after only very few iterations. The phenomenon of diminishing generated x's near full chaos for the map of Eq. (1) with λ=2 and μ=1 was observed and explained by Marotto [3] and further discussed by Gottlieb [7] in terms of the nature of fixed points for this value of λ. In view of the findings by the second author of the present paper in [12] in respect of the nature and existence of fixed points for all values of λ and μ in the map of Eq. (1), we see that Marotto's explanation holds true for diminishing x's near full chaos for λ's greater than 1.1.

The computed average energy, $\bar{E}$, versus the generalized logistic map parameter r is shown in Fig. 2 for different values of equal map exponents, λ=μ. Interest in the present study is in the chaotic regime or near it so that very small r's are not considered in the computations. We observe that the maximum r considered increases with increasing λ=μ in accordance with Eq. (2). Further, we observe that the average energy decreases both at its maximum and at full chaos (maximum r) with increasing λ=μ. Last, the highly non-linear dependence of energy on r *near* full chaos is evident with the existence of a number of extrema.

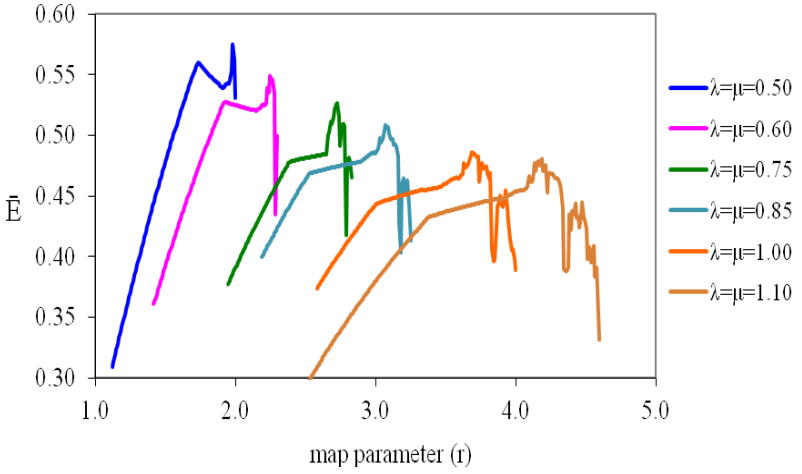

Fig. 2. The average energy, $\bar{E}$, versus the generalized logistic map parameter r for equal exponents, λ=μ.

3 The energy at full chaos

Of particular interest in the present paper is the energy generated by the generalized logistic maps of Eq (1) at full chaos, that is, when $r=r_{max}$ as given by Eq. (2). To this end, the average energy, $\bar{E}$, is computed at full chaos for different values of the map exponents λ and μ. In Fig. 3, the average energy, $\bar{E}$, is shown versus the map exponents $\lambda=\mu$. In solid line is the computed value.

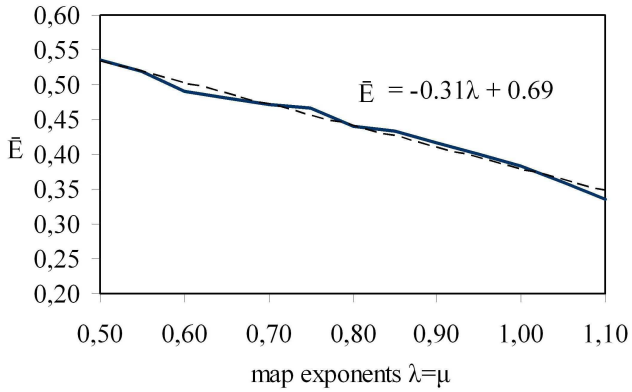

Fig. 3. The average energy, $\bar{E}$, at full chaos versus the map exponents, $\lambda=\mu$.

We observe as already noted above, that the energy at full chaos decreases with increasing $\lambda=\mu$. This decrease is substantial as exemplified by the relative energy decrease of 36% generated by the fully chaotic elliptic map ($\lambda=\mu=0.5$) and the near-logistic map ($\lambda=\mu=1.1$). Furthermore, we see that the decrease is weakly non-linear so that a linear approximation to the computed energy data points as performed by Excel results in the dashed line shown in the figure. The equation of the approximate linear dependence of the average energy on the map exponent λ ($=\mu$) is also shown in the figure. The squared regression coefficient between the two is 0.99.

Next, the average energy, $\bar{E}$, at full chaos was computed versus one of the map exponents for fixed values of the other exponent. The results are shown in Figs. 4, 5. In Fig. 4 the energy dependence on the map exponent λ for fixed values of μ is shown.

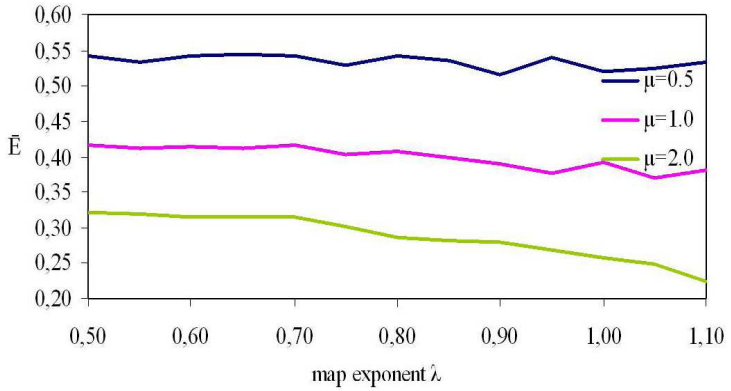

Fig. 4. The average energy $\bar{E}$ at full chaos versus the map exponent λ for fixed μ

It is observed that the average energy exhibits weak fluctuations with increasing λ and has a noticeable decrease with increasing λ only for the larger values of μ. To compare with this, Fig. 5 is shown where now λ is fixed and the energy dependence on the map exponent μ is depicted.

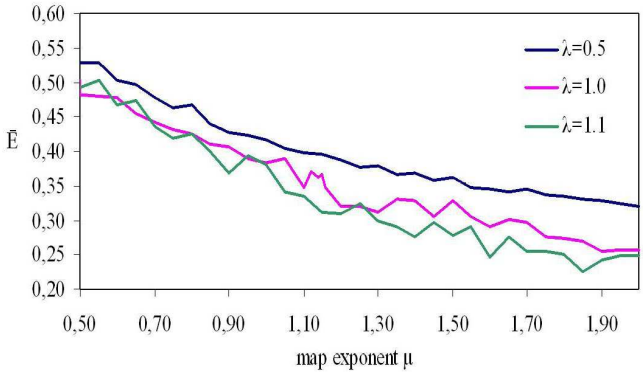

Fig. 5. The average energy $\bar{E}$ at full chaos versus the map exponent μ for fixed λ

It is seen that the energy's dependence on μ is stronger than on λ as far as its decrease is concerned.

Last, as demonstrated above for $\lambda=\mu$, it will be shown in Figs. 6, 7 that the energy's dependence on λ or μ may also be linearly approximated for unequal λ and μ if one of the two exponents is kept constant.

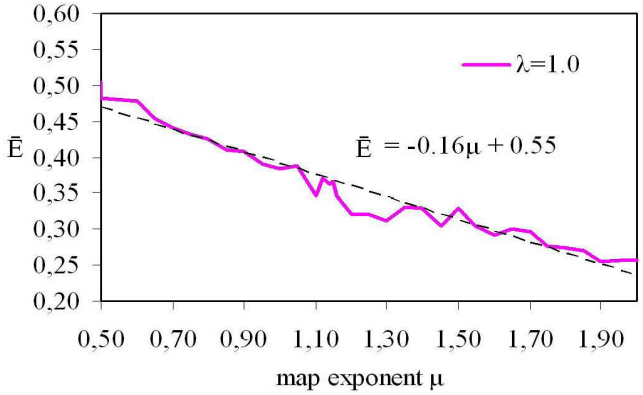

Fig. 6. The linear approximation of the average energy, Ē, at full chaos on μ.

In both Figs. 6, 7 the solid line connects the computed energy points at full chaos while the dashed line is the modeled linear approximation.

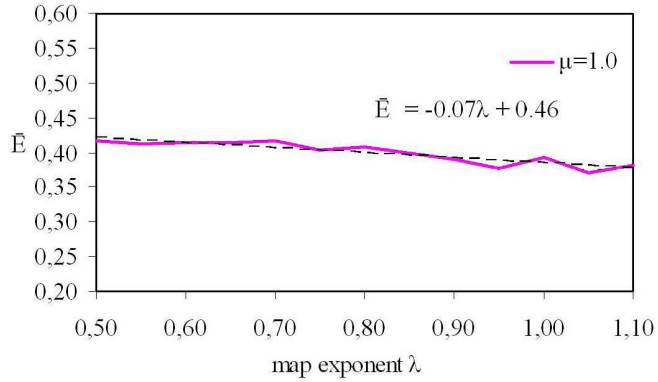

Fig. 7. The linear approximation of the average energy, Ē, at full chaos on λ.

The linear approximation of the energy with increasing map exponent λ or μ is satisfactory since the squared regression coefficients are 0.88 and 0.94 for Figs. 6 and 7, respectively.

4 Conclusions

The energy of generalized logistic maps was studied. In order to be able to compare the energy generated by different maps and also have an invariant energy value for each map, the average energy was defined for a large number (512) of iterations as the total energy per number of iterations with an initial map value that given by the map after a couple of thousand (2049) of iterations. It was found that the average energy exhibits strong fluctuations with a number of extrema near the chaotic regime whose full development is given by the maximum map parameter r.

Further, the energy at fully developed chaos decreases with increasing map exponents λ and μ and this decrease was satisfactorily approximated in a linear fashion.

References

[1] D. A. Sotiropoulos. Chaotic crack size and fracture stiffness. *Proceedings of the Thirteenth InternationalConference on Civil, Structural and Environmental Engineering Computing*, B.H.V. Topping and Y. Tsompanakis, eds. Civil-Comp Press, Stirlingshire, Scotland, paper 225, 2011.

[2] C. H. Skiadas and C. Skiadas. Innovation diffusion modeling: the deterministic, stochastic and chaotic case. *Nonlinear Dynamics,Psychology, & Life Sciences* 15 (2): 285-303, 2011.

[3] F. R. Marotto. The dynamics of a discrete population model with threshold. *Math. Biosci*. 58: 123-128, 1982.

[4] D. A. Sotiropoulos, A. D. Sotiropoulos, and V. D. Sotiropoulos. On the timbre of chaotic algorithmic sounds. In *Chaos Theory: Modeling, Simulation and Applications*, C. H. Skiadas, I. Dimoticalis and C. Skiadas, eds. World Scientific, pp. 379-387, 2011.

[5] C. H. Skiadas and C. Skiadas. *Chaotic Modelling and Simulation*. CRC Press, N. York, 2009.

[6] R. May. Simple mathematical models with very complicated dynamics. *Nature* 261: 459-467 (1976).

[7] H. P. W. Gottlieb. Thresholds in a class of iterative maps. *International Journal of MathematicalEducation in Science and Technology* 30 (1): 93-101, 1999.

[8] V. D. Sotiropoulos. The rainbow effect on composing chaotic algorithmic music. In *Chaos Theory: Modeling, Simulation and Applications*, C. H. Skiadas, I. Dimoticalis and C. Skiadas, eds. World Scientific, pp. 388-398, 2011.

[9] A. D. Sotiropoulos. Composing chaotic music from the letter m. In *Chaos Theory: Modeling, Simulation and Applications*, C. H. Skiadas, I. Dimoticalis and C. Skiadas, eds. World Scientific, pp. 369-378, 2011.

[10] M. J. Stutzer. Chaotic dynamics and bifurcation in a macro-model. *Journal of Economic Dynamics and Control* 2: 353-376, 1980.

[11] H. P. W. Gottlieb. Properties of some generalized logistic maps. In *Complex Systems: Mechanism of Adaptation*, R. J. Stonier and X. H. Yu, eds. Amsterdam: IOS Press, pp. 307-312, 1994.

[12] D. A. Sotiropoulos. On logistic-like first order iterative maps. In *Chaos Theory: Modeling, Simulation and Applications*, C. H. Skiadas, I. Dimoticalis and C. Skiadas, eds. World Scientific, pp. 77-85, 2011.